CRC Press FreeBook

# Innovations in Oil and Gas Engineering

CRC Press
Taylor & Francis Group

# Table of Contents

# Save on Essential Books in Oil and Gas Engineering

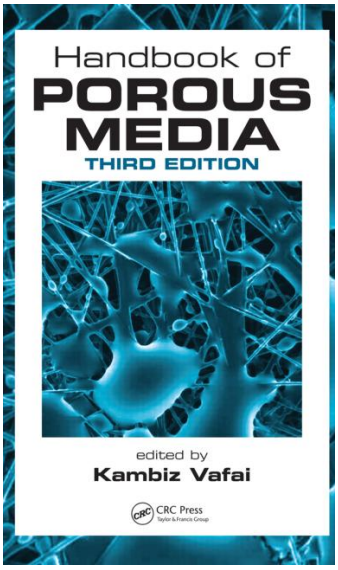


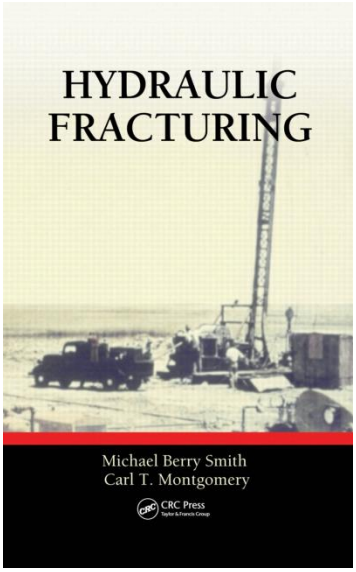


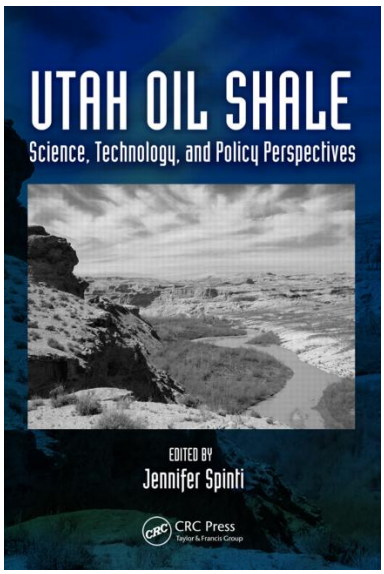


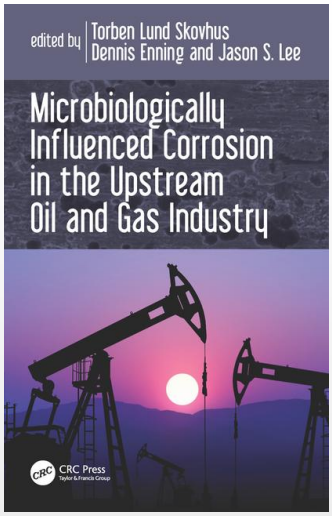


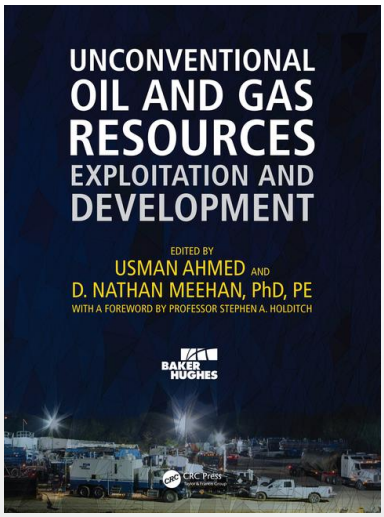


***SAVE 20%* + Receive *FREE Shipping!***

**Visit crcpress.com to browse our collection of books in Oil and Gas Engineering**

**Enter code *FBK17* at time of checkout.**

# Introduction

FREE BOOK, **Innovations in Oil and Gas Engineering**, is relevant to oil and gas professionals, researchers, and students. This book features content from a range of CRC Press titles and includes:  The Art of Data Mining and Its Impact on Unconventional Reservoir Development from *Unconventional Oil and Gas Resources: Exploitation and Development*, edited by Usman Ahmed and D. Nathan Meehan.

This book provides a comprehensive understanding of the latest advances in the exploitation and development of unconventional resources. It provides a valuable reference for geologists, geophysicists, petrophysicists, geomechanic specialists, and drilling, completion, stimulation, production, and reservoir engineers.

Definitions and Simple Geometry Models from *Hydraulic Fracturing*, written by Michael Berry Smith and Carl T. Montgomery
**This practical text** effectively busts the myths associated with hydraulic fracturing. It explains how to properly engineer and optimize a hydraulically fractured well by selecting the right materials, evaluating the economic benefits of the project, and ensuring the safety and success of the people, environment, and equipment.

Microorganisms in the Oil and Gas Industry from *Microbiologically Influenced Corrosion in the Upstream Oil and Gas Industry*, edited by Torben Lund Skovhus, Dennis Enning, and Jason S. Lee

Oilfield microorganisms can affect materials integrity profoundly through a multitude of elusive (bio)chemical mechanisms, collectively referred to as microbiologically influenced corrosion (MIC). MIC is estimated to account for 20 to 30% of all corrosion-related costs in the oil and gas industry. Exhaustively researched by leaders from both industry and academia, this book discusses the latest technological and scientific advances as well as relevant case studies to convey to readers an understanding of MIC and its effective management.

Digital Petrophysics: Imaging, Modeling, and Experimental Challenges Related to Porous Media in Oil Fields from *Handbook of Porous Media, Third Edition*, edited by Kambiz Vafai

Featuring chapters written by a compendium of international experts, this handbook offers a comprehensive overview of the latest theories on flow, transport, and heat-exchange processes in porous media. It also details sophisticated porous media models which can be used to improve the accuracy of modeling in a variety of practical applications. Core-Scale Oil Shale Pyrolysis from *Utah Oil Shale: Science, Technology, and Policy Perspectives*, edited by Jennifer Spinti

This book examines many of the issues surrounding oil shale development in the Uinta Basin, one of the largest oil shale resources in the US. Focusing on research conducted by investigators associated with The University of Utah's Institute for Clean and Secure Energy, the chapters in this book build on each other across a range of scales and of disciplines to present a comprehensive picture of the opportunities and challenges facing this nascent industry.

Please note this Free Book does not include references, endnotes and footnotes. Fully referenced versions of each book can be accessed through crcpress.com.

# Chapter 1

## The Art of Data Mining and Its Impact on Unconventional Reservoir Development

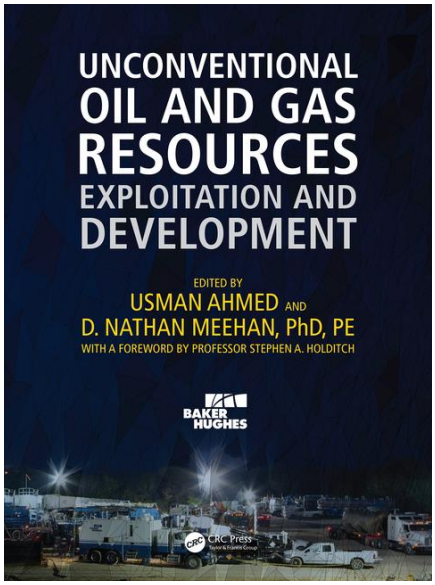


**Unconventional Oil and Gas Resources: Exploitation and Development**

*By* Usman Ahmed, and D. Nathan



To purchase a copy, click here.

## Introduction

Unconventional reservoir development is a process in which multi-million-dollar decisions must be made in a commodity environment that is both technically and fi sensitive. An operator's decision to acquire a certain unconventional leasehold or concession is a huge fi risk, perhaps one hundred million US dollars or more, that may or may not ever pay out. Reservoir quality is the fi requirement, but even if the resource is adequate, changes in operational practices may either substantially improve—or ruin—an operator's success.

North America has been, and remains, the testing laboratory for unconventional reservoirs around the planet. Many thousands of vertical wells were completed in tight gas sandstones and mixed conventional and tight reservoirs since the 1970s (Hufft, 1977; Meehan and Pennington, 1982). The modern era of "shale" reservoir drilling and completion began in the 1980s in the Barnett shale (Steward 2007), although much of the groundwork was laid by the United States Department of Energy's Eastern Gas Shales Project studies of the 1970s.
(Shellenberger et al. 2011, Ahmed, et al. 1991, Yost et al. 1980).

The previous paragraphs should be sufficient for the reader to understand the importance of careful analysis of the available data, so that expensive and risky decisions can indeed be data- driven. However, there is more. The unconventional resource owner has access to quantities of data unheard of even 10 years ago. The effect is simple–too much data, too little knowledge. This chapter is intended to discuss the important topic of practical data mining and what it can mean to the reader. The authors have presented a discussion of variables, available data, database quality control, and analytical methods. Case studies of different reservoirs are also documented.

## Fundamental Reservoir Quality Issues in Unconventional Reservoirs

Early in the modern era of mudstone reservoirs, also known as "shales," these reservoirs were often thought to have relatively uniform natural properties, perhaps with the exception of large faults that bounded different producing areas. This view led to an industry belief system that production results depended mainly on completion and stimulation parameters. There was some truth in that belief, but it was incomplete. Inadequate stimulation, that is, pumping treatments that are too small for the zone in question, produced less than desired production. At the other end of the treatment size range, too-large treatments in the Barnett could also result in poor well results. The reasons varied, but in general, the results were due to larger treatments contacting unknown geohazards, either karsts or faults, that were in communication with the underlying Ellenberger saline aquifer. Subsequent data mining work over the years has shown that the natural variability in unconventional well production is heavily dependent on variations of naturally occurring rock properties. Data mining results have also shown that well architecture, completion, and stimulation parameters can be key productivity drivers. These results hold true whether tight gas sandstones, mudstones, or light-tight oil reservoirs are under consideration.

The fundamental natural rock properties in unconventional reservoirs are found at the intersection of geochemical, geological, and geomechanical properties in the reservoir and bounding beds. For data mining purposes, geochemical parameters are less important in tight gas sandstones where migration out of the source rock has occurred. In the mudstone reservoirs, geochemical maps indicating thermal maturity yield one of the keys to understanding production variability in the source rock reservoirs.

Key geological engineering properties are represented in some of the factors of the fundamental rate equation (that is, permeability, thickness, reservoir pressure, and reservoir fluid viscosity). For the importance of the fundamental rate equation in understanding oil and gas well production, see Economides and Nolte 2000. These values do vary geologically across producing areas. Certain values, particularly matrix permeability and its variability, are difficult or impossible to obtain across tens to ten thousand or more wells, and this complicates the data mining process. The importance of natural fractures to system permeability in these reservoirs further complicates the reservoir quality picture.

Reservoir fluid viscosity impacts productivity in unconventional reservoirs. And, particular mudstone reservoirs typically show substantial variability in gas gravity as the thermal maturity varies across different areas of a play.

Reservoir thickness is a much more tractable value than permeability and is also a key to production results.

However, it should not be assumed that greater thickness would *automatically* result in greater production. Non-sympathetically varying parameters such as thermal maturity or presence or absence of fracture height growth barriers have shown in some instances to compete with pay height to reduce production.

Reservoir pressure is also a key productivity factor. Unconventional reservoirs that work tend to be over-pressured to strongly over-pressured.

From the previous discussion, it would be easy to conclude that any data mining exercise would be doomed to failure. System permeability is a substantial uncertainty. Reservoir fluid viscosity measurements are rarely available for data mining work. Pay thickness can be a bit more reliable. The good news for data mining efforts using less granular data sets, such as public data, is that natural reservoir quality typically varies systematically across geographic areas and may be proxied by the well location variables.

## Variability of Key Geomechanical Properties

In addition to the above fundamental factors, there are many other parameters that may strongly influence well production in unconventional reservoirs. Geomechanical properties comprise one set of influence parameters because they
are critical to hydraulic fracture initiation, propagation, complexity, containment, conductivity, and durability.

### Time-Dependence of Well Architecture, Completion, and Stimulation Trends

Workers with some history in unconventional reservoirs understand intuitively that well architecture, completion, and stimulation approaches have varied substantially over time.

One way to understand the macro trends is through the use of a graphic timeline, such as that shown for Barnett shale from its tentative beginning in 1981 through 2009
(LaFollette and Holcombe et al. 2012). In **Fig. 12.1—** Barnett update 2009, vertical wells are shown in yellow, deviated wells are in red, and horizontal wells are shown in blue. The dates for introduction of key technologies are shown by the annotations.

Another example is shown in tabular format (LaFollette et al. 2011) in **Table 12.1**. The abbreviation MHF is *massive hydraulic fracturing*. SWF is *slick water fracturing*.

Examination of the table reveals that, over the relatively short time frame of 6 years, completed lateral well lengths increased from an average of 1,800 feet to over 2,600 feet, while fracture treatment volume per foot decreased from 2,200 ft
to 1,400 ft. Additionally, proppant quantity increased from approximately 670 lbm/ft to 960 lbm/ft. Thus, the completion date can be a key variable describing well productivity.

Brnt Update May 2009
11494 Samples for 11782 Wells

Elastic mechanical properties of shale gas reservoir rocks were shown by Sone and Zoback (2013) to vary widely within and among reservoirs. From their experimental laboratory work, the main drivers of variability were mineralogy and rock fabric anisotropy. Practitioners also need to concern themselves with the mechanical properties of all bounding beds that may be fractured, or those that may act as fracturing barriers across any given area of study.

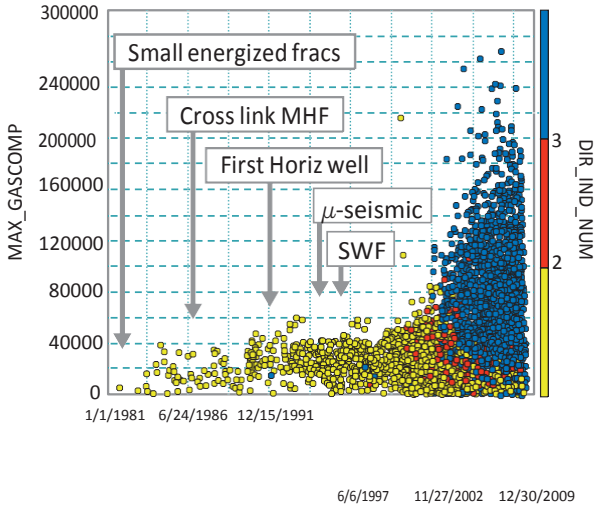


An early GIS-based analysis of the Barnett shale indicated that the presence or absence of the Viola–Simpson formation will determine if, and where, there is a hydraulic fracturing barrier. Where the Viola–Simpson formation underlies the Barnett shale across part of the Fort Worth basin, it acts as a hydraulic fracturing barrier. Where the barrier is missing, the GIS analysis shows clear evidence of a negative impact on vertical well performance

**Barnett update 2009.**

**Statistical data for whole field Barnett horizontal completions, 2004 to 2009.**

| Average Statistics for Barnett Horizontal Completetions | | | | | | |
|---|---|---|---|---|---|---|
| | Completion Year | | | | | |
| Parameter | 2004 | 2005 | 2006 | 2007 | 2008 | 2009 |
| Number of Completions | 255 | 697 | 1239 | 2303 | 2662 | 1380 |
| Perforated Length, ft | 1793 | 1874 | 2054 | 2187 | 2363 | 2675 |
| Peak Monthly Gas Mscf/mo | 52098 | 53150 | 49851 | 52640 | 54098 | 58689 |
| 1 year Cumulative Gas, MMscf/yr | 378.3 | 355.2 | 325.2 | 340.2 | 358.4 | 365.2* |
| 1 year Cumulative Liquids, BBl | 2267 | 2048 | 1552 | 1469 | 1911 | 2438* |
| 1 year Cumulative Water, BBl | 44050 | 63915 | 64825 | 73026 | 89721 | 77329* |
| Treatment Volume, Mgal | 3849 | 3793 | 3686 | 3353 | 3587 | 3796 |
| Treatment Volume/pcrf ft, gal/ft | 2206 | 1951 | 1779 | 1497 | 1418 | 1410 |
| Proppant Quantity, Mlbs | 1141 | 1400 | 1867 | 2287 | 2562 | 2624 |
| Proppant Quantity/pcrf ft, lbs/ft | 672 | 711 | 886 | 995 | 993 | 953 |
| Number of Stages | 2.1 | 2.8 | 4.0 | 3.2 | 3.2 | 3.6 |
| Peak Monthly Gas P10, MMscf/mo | 17.0 | 17.3 | 17.3 | 17.4 | 19.0 | 21.2 |
| Peak Monthly Gas P25, MMscf/mo | 29.1 | 27.4 | 26.5 | 27.9 | 30.3 | 34.2 |
| Peak Monthly Gas P50, MMscf/mo | 45.6 | 46.6 | 42.0 | 45.4 | 47.4 | 53.7 |
| Peak Monthly Gas P75, MMscf/mo | 69.6 | 68.2 | 64.1 | 68.8 | 69.2 | 74.9 |
| Peak Monthly Gas P90, MMscf/mo | 93.1 | 98.6 | 93.1 | 96.8 | 95.9 | 103.3 |

*Limited Sample Size

## Evolution of Data Mining

### Non-Oilfield Data Mining

Data mining is an analytic process of knowledge discovery. In a data-mining project, we collect raw data, examine the quality of the data, and explore the data to find intrinsic relationships and consistent patterns. Ultimately, we want to apply these findings to help us make predictions on new datasets. Data mining may sound like an abstract concept, but it's actually underlying many things, influences many aspects of our daily life, and shapes our future.

Market survey questionnaires are distributed to random customers to gain feedback on specific products or services to enable the provider to make improvements. Think of those short online surveys printed on your restaurant receipts that contain several feedback questions! Responses are data-mined to provide guidance to the management.

In clinical trials, all subjects' vital statistics are collected periodically together with the drug usage, including placebo usage and drug dose, to make an inference on the drug toxicity and efficacy. All drugs have to go through multiple-phase clinical trials before being approved by the US Food and Drug Administration (FDA).

In financial services, every bank has its own set of criteria for loan applications. In this type of data-mining exercise, a statistical model is built upon large historical datasets that automatically pulls all the applicants' credit information, including but not limited to, credit scores, loans and mortgages, and delinquency history. The data-mining algorithm then uses that data to evaluate the risk of charge-off. If the predicted risk is lower than a preselected threshold, the application will be approved.

Social media companies apply algorithms to look into users' emails, forum posts, videos viewed—and even who their friends are—to allocate hobbies and interests before they send out targeted advertisements.

Data mining has a close similarity to statistical methods, and the terms have been used in the literature interchangeably. Exploratory data analysis methods, such as scatter plots and histograms, can be used to describe different perspectives of the data and summarize them. Linear models provide straightforward preliminary descriptions of variable relationships. Principal component analysis, factor analysis, and cluster analysis bear important merits in high-dimension datasets. Due to the rapid development in computer technology, machine learning has emerged as a new trend in data mining recently, including random forest, boosting, and support vector machines. Unlike traditional statistical models, these methods don't require an explicit expression of the model in the beginning.

### Early Oilfield Formation Studies: Number 2 Lead Pencils and Graph Paper

Practicing engineers have attempted to put pencil to paper and correlate field practice with production and economics for a very long time. When the earliest formation, completion, and stimulation studies known to the authors were done in the 1960s, modern data mining methods were in their infancy. Early work from engineers in the oilfield consisted of compilations of existing practices, perhaps with calculations designed to offer an understanding of the theory and practice. These studies involved very limited data and effectively represented "current events."

### Computers and Univariate Statistics: Spreadsheets and Cross Plots

Early formation studies in which relatively large datasets (for the time) were used include a study of the Second Frontier formation of the Moxa Arch, southwest Wyoming, US (LaFollette and Davis, 1993.)

In that project, public datasets were gathered from a subscription to Petroleum Information (now IHS Energy). Monthly production streams from approximately 500 wells were decline-analyzed by hand to generate production metrics. A computer spreadsheet application was then used to graph and correlate data, such as sedimentary depositional environment, porosity and permeability, fracturing fluid type, and so on. The data was used for correlation to target variables such as estimated ultimate recovery (EUR) and initial potential (IP) metrics using linear regression. Studies such

as this are univariate statistical studies, where independent variables are each correlated in isolation to a target variable. In these types of studies, interactions among the so-called "independent variables" are not typically considered.

Univariate statistical studies at the time did not generally take advantage of the more modern understanding of the importance of reservoir quality proxies, and thus suffered from the fact that much of the driving force (that is, the interaction of permeability, pressure, thickness, and hydrocarbon viscosity) behind well productivity was excluded from the analysis.

### Map-Based Analysis: Geographical Information Systems (GIS)

While spreadsheets and cross plots have certain uses, map- based GIS analysis brings a geoscience-based perspective to the analysis, interpretation, and display of complex integrated datasets. Certainly, the early work of this nature in the earth sciences field came from geologists and geochemists putting their data on hand-drawn maps. With the advent of GIS mapping applications such as ESRI's ArcView™ (supplanted by ArcGIS™), IHS Energy's Petra™, and Schlumberger's Petrel™, workers have been much more productive in terms of the sheer numbers of maps they could generate. However, this was only the beginning, as the speed with which maps can be modified to show, for example, the best and worst 10% of wells in a given play, can allow direct question and answer using the map. Present-day GIS applications have evolved far beyond their original geological and geochemical uses.

GIS applications are useful for analysis and display of all data categories from well architecture through production. Even simplistic well azimuths drawn as straight lines from surface to bottom-hole locations were used in groundbreaking work that proved the importance of well azimuth to productivity in the Barnett shale. Attribute functions can be easily used to show stage counts. Specialized functions such as the drainage radius function in the IHS Energy Petra™ application can be used to directly show treatment size as high aspect ratio ellipses that can be aligned in the maximum horizontal stress direction where it is known. Work with GIS methods begins by enabling workers to store all available data in a well-centric manner, using a unique well identifier (UWI) number assigned to each well's data. Critical to good interpretation, GIS applications can store geological, geochemical, and geomechanical data along with well logs, plus engineering and production data. Much of the data from tables within a GIS application may be analyzed internally and then displayed directly on the map. This offers the advantage of immediately taking data—such as treatment size, fracturing fluid type, well azimuth, completion stage count—and immediately putting it into a geographic and geologic perspective.

GIS is so useful to us because it makes use of the human brain's inherent pattern recognition ability. An example to think about is our innate ability to instantly recognize the faces of the people we know. Use of GIS methods not only allows engineering inputs to be analyzed in geological, geomechanical, and geochemical perspective, but it also enables the practitioner to study and recognize patterns on the map. This makes GIS a very powerful analytical tool, not only to aid the data miner in interpretation, but to also show data and knowledge on the map in patterns that can be easily comprehended and explained.

### Present Day: Multivariate Statistics Combined with GIS

There are many different methods used in multivariate statistical work. For a more complete study of the different methods available, refer to Zangl and Hannerer 2003; Nisbet et al. 2009; and Hastie et al. 2009.

Early GIS work for well optimization was presented in Economides and Martin, 2007. Evolving workflows have taken GIS work with multivariate statistical work and combined them to create a powerful workflow method that can be used by other workers. This allows the practitioner to take advantage of the power of each set of methods. In these workflows, "sanity checked" datasets are developed and analyzed using boosted tree methods to develop the influence plots highlighting key well productivity drivers. A commercial GIS application is then used to further develop the interpretation and to display key insights on maps.

## Data Availability

There are many different sources of data, public and proprietary, that are available for study. The data is classified into different types, and then categorized into subgroups. This section discusses the issues associated with the variety of data streams available (or not) for data mining.

## Data Categorization

There are numerous random variables in our daily work. We can classify them into a few categories based on their intrinsic characteristics. Generally, there are two types of variables: numeric variables and categorical variables. A numeric variable can be either an integer or a decimal. A variable with integer values is termed a *discrete numeric variable*. Two examples would be the number of fracture stages and well completion year. On the other hand, a variable with possible decimal values is termed a *continuous numeric variable*. Two examples of continuous variables are total proppant quantity and cumulative lateral length. In other words, continuous variables can have any value within a *theoretically possible* range of values. A categorical variable can only take values from a few categories. If these values can be ranked and sorted, the variable is ordinal, otherwise it is nominal. Proppant mesh size is an example of an ordinal categorical variable, while well completion type is an example of a nominal categorical variable.

Variable classification is very important, since we need to apply different methods to visualize the different categories in exploratory data analysis. This will be discussed in more detail in Section 12.5.2. Correct variable classification can also be helpful in data quality control. If a fracture stage count value was 8.5, or a proppant mesh size was shown as 204.0 in the raw data, it would be clear to a domain expert that something was wrong, as those values would not be possible. Those data points would then need to be fluid for further investigation and correction, removal, or marked as suspicious.

It is worthwhile to mention that the API (UWI) number is a crucial variable in all oil and gas data manipulation, since it is the "unique, permanent, numeric identifier." A 14-digit API number is composed of 2-digit state code, a 3-digit county code, a 5-digit well identifier for the permit, a 2-digit directional sidetrack code, and a 2-digit event sequence code.

Well data can be subdivided into reservoir quality, well architecture, well completion, stimulation, and production classes.

Knowledge of the reservoir is crucial to optimize shale play production. Reservoir quality can be characterized based on total organic carbon (TOC) kerogen, thermal maturity, porosity, permeability, mineralogy, lithology, brittleness, thickness, stress regime, depositional environment, reservoir pressure, viscosity, fluid regimes, and distribution of natural fractures, to name but a few. Different hydrocarbon types may be characterized by their cumulative gas-to oil ratio (GOR). Fluid types evolve basinward from black oil to volatile oil, condensate, and finally to dry gas, and vary with increasing formation depth, pore pressure, API gravity, and thermal maturity. When resources for petrophysical analysis are not available on the scale required for work with thousands of wells, and when public data are used, X-Y surface location can be used as a proxy for the data sources.

Well architecture data includes completed lateral length, well azimuth, and well dip angle. Completed lateral length is calculated as the measured depth of the bottom perforation or sleeve, minus measured depth of the top perforation or sleeve. Average azimuth calculations were taken from the actual directional survey in the completed lateral section of the well. Special care was taken when calculating well azimuth when survey points crossed the due north dividing line between the northwest and northeast quadrants. These wells were fluid azimuths were projected onto
he southeast/southwest quadrants, average azimuth was calculated, and then projected back to their original directions. Well dip angle was averaged from the actual
directional survey over the completed section of the lateral. Wells with dip angles less than 90° are toe down, wells having dip angles greater than 90°are toe up, and wells at 90° are fluid.

The well completion can be either open-hole or cased-hole (plugged and perforated). Well completion data contains

casing size, casing length, cementing depth and method, bore hole diameter, number of stage counts, clusters counts or clusters per stage, and the length of stage.

Well stimulation treatment data will be focused on generic fracturing fluid type and volume, proppant type, proppant quantity, mesh size, average pressure concentration, injection rate, and additives.

Well production and production proxies, such as maximum oil rate in the final 12 producing months and normalized 12-month cumulative production, were often selected and merged with the other data for analysis. The best-producing month in the final 12 producing months (BO) gives an indicator of the factors studied that can drive overall well early time production rate. The BO/ft. is a measure of efficiency of completed well length. Cumulative 3-month and 12-month oil/gas production was based on 3 and 12 months of active production beginning with the peak month.
For unconventional reservoir development, how to optimize drilling and completion and how to effectively predict production remains a major challenge in the oil and gas industry. Thus, data integration and analytic innovation are becoming more and more important.

Public Data Sources

In the North American oil and gas industry, state governments generally give the public the right to access government oil and gas records. Certain exceptions may apply to the disclosure of the information. The Railroad Commission of Texas maintains historical information that is used by employees, other state agencies, local government, the oil and gas industry, and the general public in its Central Records and Imaging units. An estimated 132 million pages of analog and digital documents encompassing the history of each Texas oil and natural gas well—from the drilling permit application to the final plugging report—are preserved. The oil and gas potential profit includes applications to drill, oil and gas completion reports, plugging reports, producer's transportation authority, and miscellaneous records from 1964 to the present. The well log (WL) profile includes images of all well logs received since July 2004.

The following is the data link from Railroad Commission of Texas:

http://www.rrc.state.tx.us/data/index.php#

Similar to Texas, the following states' websites contain information related to oil and gas well permits, leases, rigs, and production or drilling reports. Some states have online mapping applications and the well locations are updated daily. The following states' websites are active as of the date of this writing:

Arkansas:
http://www.aogc.state.ar.us/JDesi gnerPro/ JDPArkansas/default.htm

Colorado:

http://cogcc.state.co.us/Home/gismain.cfm

Kentucky:

http://oilandgas.ky.gov/Pages/ProductionReports.aspx

Montana:

http://www.bogc.dnrc.mt.gov/webapps/ dataminer/

New York:

http://www.dec.ny.gov/energy/1603.html

North Dakota:

https://www.dmr.nd.gov/oilgas/

Utah:

http://gis.utah.gov/data/energy/oil-gas/

Virginia:

http://www.dmme.virginia.gov/dgoinqui ry/frmMain.aspx?ctl=1

West Virginia:

http://www.dep.wv.gov/oil-and-gas/databaseinfo/Pages/default.aspx

Fracfocus:

http://www.fracfocus.org/

In 2011, the FracFocus.org national chemical registry website was created. The website was formed to give the public access to detailed information on every fracturing treatment pumped in the United States. It is currently managed by the Ground Water Protection Council and the Interstate Oil and Gas Compact Commission. The well data sheet contains the technical information about the fluid type, proppant type, all fluid additives with purpose and concentration, trade name, supplier, ingredients, chemical abstract service number, ingredient percentage in additive by percent of mass, and the ingredient concentration in hydraulic fracturing fluid percentage by mass. The well data sheet also includes key well data such as fracture date, location, API number, depth, operator, well name, total water volume, and production type. All data is based on the total material injected into the well, but the data is not broken down by stage or the number of stages.

**Vendors' Data**

Commercial datasets about well history, completion practices, and monthly production are available to be purchased from vendors, such as IHS, or Drilling Info, but are not available from the states' websites.

**IHS**

http://www.ihs.com/products/oil-gas-information/production- data/index.aspx

The **IHS Energy** well database contains well header data, location, key well dates, producing formations, actual directional survey, well test, treatment information, and production stream data.

http://www.ihs.com/products/oil-gas-information/production- data/index.aspx)

The IHS web site states: "IHS has a team of experts who work daily to transform original raw data received in multiple formats and in several languages, following different company or country standards and from various sources into the critical information fi for customer's requirement. IHS Production Data covers the world from Canada, the United States and 85 countries."

Canadian production data is available on over 800 approved and pending down-spacing applications to Alberta's Energy Resources Conservation Board. Canadian fluid analyses and pressure information is updated regularly, as well as providing written and visual depictions of well production and performance.

US well and oil, gas, and water cumulative and monthly production volumes are available on over 1.7 million producing entities. IHS has the following to say: IHS Drilling and Rig Activity products cover every facet of US drilling activity, from permits through completion, along with instant access to detailed analysis of daily updated well activity across the country.

IHS Oil and Gas Log Data products provide critical data for well properties, hydrocarbon zones, and optimal production methods. Digital and raster log databases contain the historical well log coverage in the industry for both continental and off-shore exploration.

Drilling info http://info.drillinginfo.com/products/

"Drilling Info provides an online permit, completion mapping, historical well and scout information, nationwide production data, and international regional information. DI Desktop is one of their powerful production analysis tools. It will not only deliver well production, decline curve analysis, and estimated ultimate recoveries, but contains transporter, gas plant/refineries and pricing data."

RigData http://www.rigdata.com/Index3.aspx

RigData says they provide the information pertaining to drilling activity in the United States, the Gulf of Mexico, and Canada. It has comprehensive reporting on drilling permits, drilling activity, and tracking for drilling rig locations.

RigData collects and publishes extensive information on permits-to- drill, completions data, drilling rig locations, and overall oil and gas drilling activity.

**Proprietary Data Sources**

Besides public and vendor databases, operators and service companies will have their own proprietary data sources. In-house databases have been used extensively for data mining purposes. Most of the time, these are more reliable than public data sources, although none yet has been found to be without some level of error.

At Baker Hughes, we have the PowerVision™ stimulation and cementing database, hydraulic fracturing JobMaster™ database, drilling and evaluation MaPS system database, product line financial SAP database, and rig data.

**The Baker Hughes PowerVision™** applications allow engineers to enter job information simultaneously into one centralized database. The system allows all authorized users to view and create job proposals from any location. It provides quality services and products to our customers. The database contains general information, regarding the customer, business and technique contact name etc., and well information, such as name, rig name, API, location, etc., service line information, such as cementing, acidizing, fracturing, casing, etc. Based on the wellbore hole OD, measured depth, and true vertical depth, the system will provide calculated annular volumes of slurry, shoe track volume, along with pump via data, displacement volume, etc. PowerVision has detailed pressure- pumping jobs, such as stages, injection rate, fluid type, volumes, proppant type, quantities, mess size, and mass, etc.

**JOB master** contains detail fluid, proppant, tubing, and casing databases. Job events are logged automatically, entered manually, selected from a pre-defined list, or recorded from a compatible device. Job data may be played back for purposes of demonstration or parameter recalculation. The customer version is available for post-job analysis and remote monitoring.

**Rig data.** Baker Hughes has issued the rotary rig counts as a service to the petroleum industry since 1944, when Hughes Tool Company began weekly counts of US and Canadian drilling activity. Hughes initiated the monthly international rig count in 1975. The North American rig count is released weekly at noon central standard time on the last day of the workweek. The international rig count is released on the fifth working day of each month. The Baker Hughes Rig Counts are an important business barometer for the drilling industry and its suppliers. When drilling rigs are active, they consume products and services produced by the oil service industry. The active rig count acts as a leading indicator of demand for products used in drilling, completing, producing, and processing hydrocarbons.

> Baker Hughes Rig Counts are published by major newspapers and trade publications, are referred to frequently by journalists, economists, security analysts and government officials, and are included in many industry statistical reports. Because they have been compiled consistently for 60 years, Baker Hughes Rig Counts also are useful in historical analysis of the industry. The working rig location information is provided in part by RigData. http://www.rigdata.com/index.aspx

**MaPS.** The Maintenance and Performance System (MaPS) provides Baker Hughes with operational data, equipment repair and maintenance data, and tool failure and quality incident data. MaPS makes the entire equipment life-cycle transparent, because it covers all aspects of the tracked equipment, and helps to achieve important business goals like improving the overall reliability and quality, reducing maintenance costs, and providing up-to-date equipment and service information at any time. The maintenance, operational, and tool failure data that is entered by MaPS users worldwide, or is pulled from other systems like SAP®, Advantage, and Power, enables Baker Hughes to predict tool maintenance intervals, track tool repair and maintenance efforts, and to query information for generating standardized and custom reports on product configuration, product reliability, and performance.

## Data Quality Control

Ideally, we would like to see a fully automatic system, within which raw data collection, data processing, and data storage functions are seamlessly integrated. However, many data are still hand-written recorded by field engineers, then extracted from paper and typed into the database. Human error like fat fingers is inevitable in this procedure. Before starting any data interpretation work, we need to scrutinize our raw datasets with various criteria for quality control. Sanity check can never be exaggerated. Remember that "garbage in, garbage out."

### Verifying and Validating Units

The commonly used units for proppant quantity in the US are pounds, sacks, or tons and the units for fracturing fluid volume are gallons or barrels. However, we cannot take units as guaranteed in real datasets. Actually, it is common to see erroneous units in large datasets, especially from public data sources. The following table (**Table 12.2**) is a frequency table showing the distribution of fracture fluid units from a public dataset. We can see that the majority records have correct units with either gallons (GAL) or barrels (BBL). But, a fair number of units are missing and some erroneous units exist in the dataset.

After verifying and validating units of records, an essential step in data processing is to reconcile and unify the units in subsequent work. In other words, all proppant amounts need to be converted into values in pounds and fracturing fluid volumes need to be converted to values in gallons. The transformation includes:

- 1 SACK = 100 LBS,
- 1 TON = 2000 LBS, and
- 1 BBL = 42 GALS.

### Known Limits and Ratios

When there is a negative value in a proppant or fl column, we immediately know it is an error. The largest fracture job size we've seen in the studies has approximately

**Table 12.2—Frequency table with distribution of fracture fl units from a public dataset.**

| | BBL | CF | GAL | HOLE | LB | MCF | QT | SACK | TON |
|---|---|---|---|---|---|---|---|---|---|
| 65217 | 190548 | 2695 | 135076 | 1 | 36 | 9441 | 2 | 6 | 128 |

10 M lbs of proppant and 0 M gals of fracturing fl

If a record contains a tenfold bigger job size, it is suspicious and needs to be revisited and validated. Another very useful criterion is to check if proppant concentration is in a reasonable range. Proppant concentration is the value of total proppant over total fracture fl and is expressed in pounds/gallon. The theoretical upper limit is 25 lbs/gal, but the realistic values are most likely less than 10 lbs/gal. A record containing 2 MM lbs of sand and 75,000 gallons of cross-linked gel is clearly problematic.

### 1ther Outlier Checks

It's always helpful to visualize the data and plot the distribution of each variable. If a few data points are far from the others, we need to verify and validate those distant points. Both histogram and scatter plot methods, which will be introduced in 12.5.2, are very effi ways to identify outliers.

## Analysis Methods

### Map-Based Methods

GIS maps can be used for many different analyses of unconventional reservoirs. First, GIS maps can be used to gain the interpretive perspective of geologically driven, geographic location-based changes in fundamental reservoir

properties. For example, reservoir depth and thickness frequently change in a predictable, but nonlinear, fashion. Thermal maturity can be mapped directly and can show geographical change. Simple mappings of hydrocarbon types or well classification can lead to an increased perspective, which contributes to the prediction of production variation related to gross well location within the study area. In another example, geological features, such as faults, may be associated with poor wells.

In an early example of GIS-based analysis (that is regretfully proprietary), of the Barnett, consistently derived petrophysical parameters were mapped, contoured, and then overlain by an estimated ultimate recovery (EUR) bubble map. Examination of the map clearly demonstrated that the EUR was not consistent with the petrophysical variables. In that instance, the best indicator of vertical well EUR was the water-to-gas ratio (WGR), with the poorest wells having the highest WGR values. At issue was fracture stimulation treatments hitting faults, or otherwise communicating with, the wet Ellenberger dolomite and bringing salt water into the completion.

At the point when a proper understanding is reached about the impact of geoscience on production, then the author's GIS workflow enters into the "considerations of well architecture" phase. Cumulative frequency histograms of production metrics are used to identify the distribution's tails, and the (for example) best and worst 10% wells can then be displayed on the map, excluding the middle 80%. The goal of this analysis is to identify natural geographic sweet- and not-so-sweet spots by observing whether the best and worst wells are intermixed or if they are geographically separated into specific parts of the study area. Overlays can be used to outline sweet spots. Less-than-optimum producers within sweet spot areas can be further investigated for problems associated with original well architecture, completion, and stimulation that may or may not be possible to remediate.

Direct display of actual well paths from directional surveys is a key to pattern recognition methods of GIS analysis, although surface and bottom-hole locations may be used if they are all that is available. It should be noted that an assumption of a straight-line well path may be incorrect in the plays in which "turnizontal" wells were drilled in order to gain the geomechanically most favorable well path in an unfavorably oriented lease. Examining the well path data via the map is a means of identifying optimum and non-optimum well paths and too-short laterals in different parts of the play.

The attribute function of GIS programs provides a means of visually identifying stage count groups. Proceed with caution when better producers within a geographic area show higher stage counts, because a more detailed investigation may be needed to separate the stage-count effect from the treatment- size effect.

As indicated previously, treatment volumes and proppant quantities can be shown on the map through the use of drainage radius or perhaps other functions. In one example, the method plots a high aspect-ratio ellipse with size and color showing the proppant quantity pumped in each well. When plotted in conjunction with the stage count and production metric, oversized and undersized treatments can be readily identified and compared to production results.

The level of analytical detail and understanding that can be achieved using GIS analysis is first and foremost based on the level of granularity of the dataset being studied. Equally important is using the full interpretive power of the different disciplines working together on projects. A geologist trained in understanding reservoir geometries, thermal maturity patterns, and so on, brings much more insight to the interpretation of the engineering parameters, while the engineer(s) bring insights and experience from their own discipline to aid the final integrated study result.

## Exploratory Data Analysis

The first two questions that arise when we tackle any analytic problem are, "what is my goal?" and "what data do I have?" A quick tour of the available dataset will plot the profile of our task. Despite the advances in modern sophisticated statistical methodologies, several traditional methods play important roles in exploratory data analysis.

The frequency table displays the distribution of a categorical variable in the dataset by associating the possible values of the variable with the corresponding frequency or relative frequency (i.e., percentage). An example of a frequency table for the well distribution over districts in the Wichita- Albany formation from a proprietary dataset is shown next. A table that displays a single variable is also known as a one-way table.

A two-way table shows the joint distribution of two categorical variables. The two-way table often helps with identifying the association between these variables. There are different criteria for the well completion type. The two-way table, next, indicates that all engineered wells used sleeves in the completion example shown.

The bar plot in **Fig. 2** visualizes the related frequency table for better readability. We converted the previous one-way table example to a bar plot. In this example Gaines County has most of the wells.

Both frequency tables and bar plots are apparatuses for categorical variables. A widely used visualization method for numeric variables is the histogram, which looks very similar to a bar plot. A histogram shows the frequency distribution of a numeric variable upon a set of consecutive bins. The number of bins can be adjusted to serve the presentation purpose. However, either too many bins or too few bins can dilute the information from the data. There are typically 5-to-10 bins in a histogram. The following histogram for the variable maximum monthly oil production in BOE shows a highly right-skewed distribution, with only a small percentage of the wells showing production over 6,000 BOE (Fig. 12.3). Note that the vertical scale is relative frequency in this example, which ensures that the area under the overlaid fitted curve is normalized to one. Also, the wells with ultra-high production (over 12,000 BOE) are outliers, based on the distribution and need to be validated.

**Table 3—Frequency of well distribution over districts in the Wichita-Albany formation from a proprietary dataset.**

| ANDREWS | CRANE | ECTOR | GAINES | WARD | WINKLER |
|---|---|---|---|---|---|
| 79 | 58 | 20 | 194 | 49 | 29 |

**Table 12.4—Two-way table showing that all engineered wells used sleeves in the completion.**

| | Ctype2 | |
|---|---|---|
| Ctype1 | Engineered | Geometric |
| Plug & Perf | 0 | 2 |
| Sleeves | 65 | 2 |

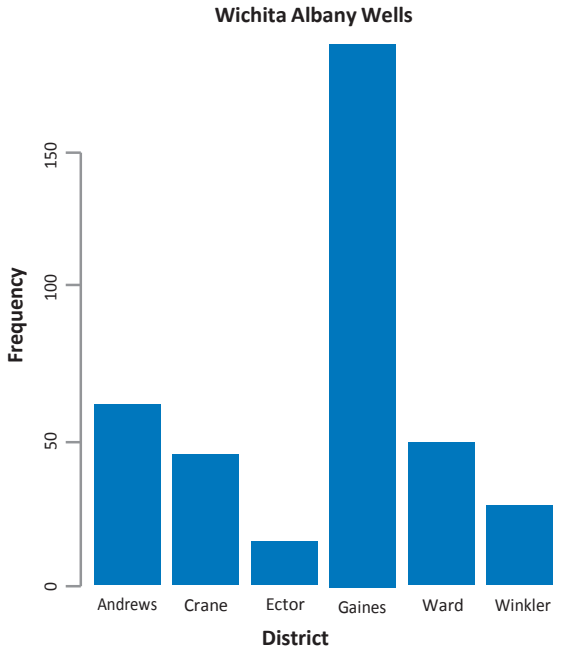


**Fig2—Bar plot showing the data for the related table in Table 12.4.**

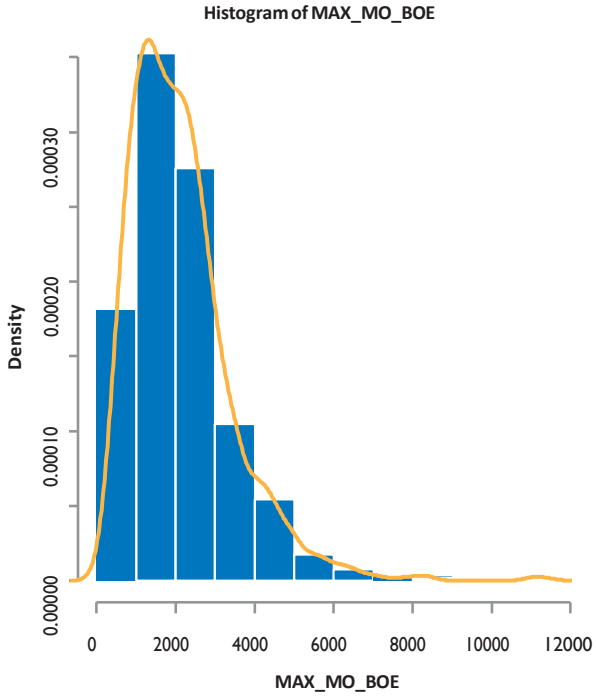


Fig. 12.3—Histogram of MAX_MO_BOE bar plot.

A scatter plot (shown in **Fig. 4**) uses Cartesian coordinates to display values of two or more variables from a dataset. It shows various kinds of correlations between these variables, as well as the existence of outliers. The scatter plot, next, indicates that there is a positive correlation between fracture fluid and proppant. There is an outlier that is far away from the others that needs further verification.

When a dataset contains many variables, it will take a lot of scatter plots to inspect the pairwise relationship between them. It's neither convenient nor efficient to flip through dozens of plots. Instead, we can integrate selected scatter plots into a scatter plot matrix and review all the pairwise relationships simultaneously. The scatter plot matrix, next in **Fig. 5**, contains 91 independent scatter plots taken from 14 variables. The target variable is the cumulative 30-day production, beginning with peak production within the first 12 producing months. The predictor includes fracture stage count, average stage length, gross fracture fluid amount, proppant quantity, and other well parameters. Each off- diagonal cell $c_{ij}$ is a scatter plot between two variables; one is listed in the diagonal cell $c_{ii}$ along the horizontal direction and the other can be found in the diagonal cell $c_{jj}$ along the vertical direction. Note that the scatter plots in cell $c_{ij}$ and $c_{ji}$ are essentially the same. One is the mirror image of the other after 90° counterclockwise rotation. According to the scatter

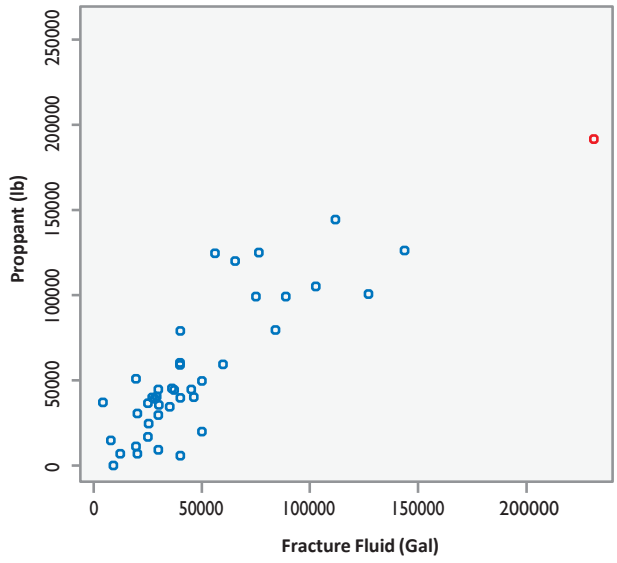


**Fig. 4—Scatter plot with Cartesian coordinates showing dataset variables.**

plot matrix, we can find (aside from the positive correlation between the fracture fluid and proppant, as we mentioned before), the number of fracture stages is also strongly correlated with these two variables.

There are other frequently used methods in exploratory data analysis we didn't discuss here, such as the pie chart and box plot. Interested readers can easily find an introduction to these two chart types in reference books or online.

## Linear Methods

In statistics, regression analysis is the analysis of the relationship between a response or outcome variable and another one or more explanatory variables. For one explanatory variable, it is called simple linear regression. For more than one explanatory variable, it is called multiple linear regressions. It is different from multivariate linear regression, where multiple correlated dependent variables are predicted, rather than a single scalar variable.

The relationship is expressed through a statistical model equation that predicts a response variable (or dependent variable) from a function of regressor variables (or called independent variables or explanatory variables) and parameters. In a linear regression model, the predictor function is linear in the parameters. The parameters are estimated so that a measure of fit is optimized.


**Fig. 5—Example of 91 separate scatter plots created from 14 variables.**

The multiple linear regression equation is as follows:

$$\hat{Y} = b_0 + b_1X_1 + b_2X_2 + \ldots + b_pX_p \quad \textbf{Eq. 12.1}$$

where $\hat{Y}$ is the predicted value of the dependent variables, $X_1$ to $X_p$ are $p$ distinct independent variables, $b_0$ is the value of Y when all of the independent variables ($X_1$ to $X_p$) are equal to zero, and $b_1$ to $b_p$ are the estimated regression co-effient. Each regression coefficient represents the change in Y relative to a unit change in the respective independent variable.

While mining production or production efficiency in major shale plays, the production (initial production, three- cumulative-month production, etc.) is usually the dependent variable and parameters from reservoir properties, well architectures, completions, and stimulations are independent variables to be regression studied through statistical modeling. (See the case study as example.)

## Tree Boosting Methods

Machine learning methods have gained momentum across various fields recently. Benefits from rapid advances in computer science and technology, machine-learning methods can be applied to modeling problems in a different way than traditional statistical modeling. Traditional statistical models start from an explicit expression with a set of unknown parameters, and then those parameters are tweaked to achieve the best match with real data according to certain criteria (typically, minimizing a metric).

Machine learning methods, instead, have no specific predefined models, but instead rely on the "brute force" power from the computer to learn the relationship between the variables and find dominant patterns between the target and predictors. Two widely used machine-learning methods—*random forest* and *boosting*—are both decision- tree based. A decision tree is a tree-like hierarchical model used to map observations of a subject to conclusions about the subject's target value. Fisher's iris dataset consists of 50 samples from each of three species of iris: setosa, versicolor, and virginica. Four characteristics were measured for each sample, including the length and the width of the sepal and petal (in centimeters). A decision tree was built to use these four characteristics to predict the species of iris (**Fig. 12.6)**. From the results:

- Node 2 contains 50 samples from branch, with petal length ≤ 1.9, and the species are all setosa
- Node 5 contains 46 samples from branches with 1.9 < petal length ≤ 4.8 and petal width ≤ 1.7, and the species are mostly versicolor
- Node 6 contains 8 samples from branches, petal length > 4.8 and petal width ≤ 1.7, and they are half versicolor and half virginica
- Node 7 contains 46 samples from branches with petal length > 1.9, and petal width > 1.7, and the species are mostly virginica

To verify the accuracy of this decision tree, we can check the cross table between the predicted species and the true species. In the table below (Table 5), the columns label the prediction and the rows the true species. We can see that only 6 cases out of 150 are misclassification under a single decision tree. Boosting the method builds a series of trees subsequently during modeling. Each tree is built upon a random subsample of the train dataset and the residual from the previous tree, which is treated as target variable. Note that tree boosting

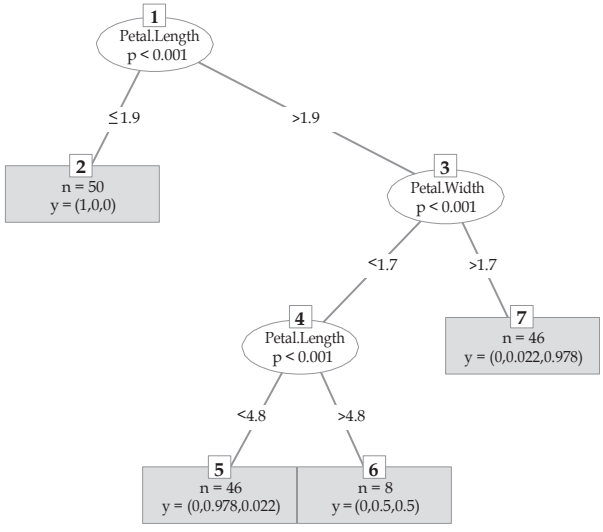


**Fig. 12.6—Iris species prediction decision tree.**

**Table 5—Iris data table showing data for predicted and true species.**

| | setosa | versicolor | virginica |
|---|---|---|---|
| setosa | 50 | 0 | 0 |
| versicolor | 0 | 49 | 5 |
| virginica | 0 | 1 | 45 |

requires a minimum of assumptions about data structure, and is more resistant to common data quality issues like outliers and missing data than traditional statistical modeling is. We can evaluate the impact of individual predictors upon the target, based on the output of the relative importance chart. From that output, we can observe the marginal effect of individual predictors upon the target, while the influence of other predictors is "integrated" out. We will illustrate the application of this method using a few case studies in the next section.

## Case Studies

The remainder of the chapter is devoted to case studies about three well-known unconventional reservoir plays in North America. Each case study is presented as a means of reinforcing the data sources, quality control, data exploration, data mining concepts, and key lessons learned using the methods described above.

## Barnett Shale

The Barnett shale of the Fort Worth basin is a complex mudstone reservoir. X-ray diffraction (XRD) analysis of 66 samples of Barnett shale from 13 counties indicates that quartz, feldspars, carbonate minerals (mainly calcite, dolomite, and siderite), and clays (mainly illite/smectite) are the main minerals present. **Fig. 12.7** highlights the variable nature of Barnett mineralogy.

The Barnett offers much data to study and has been data mined extensively by the authors (LaFollette, 2011 and LaFollette, 2012.) The major goals of these Barnett studies were to analyze well and production data from Barnett vertical and horizontal wells in order to better understand critical and not-so-critical productivity drivers. (See **Fig. 9** and **Fig. 10** later in this section for a graphical representation of the data.)

Study well data were taken from the IHS Energy US Well Database subscription, and from the Baker Hughes internal PowerVision database. Over 211,000 wells were selected for analysis (LaFollette, 2012) including the over 15,000 Barnett wells producing in 2011. Standard procedure is to load all well header and production data into a commercial GIS application.

The process of quality control began immediately by checking well locations against map overlay boundaries. Wells shown were color-coded by well type, with gas wells in red, oil wells in green, and injectors in blue (**Fig. 12.8**). Background geological studies indicated that all conventional reservoirs in the study area were sourced by the Barnett shale. Thus, the map became a proxy for gross thermal maturity variation across the basin.

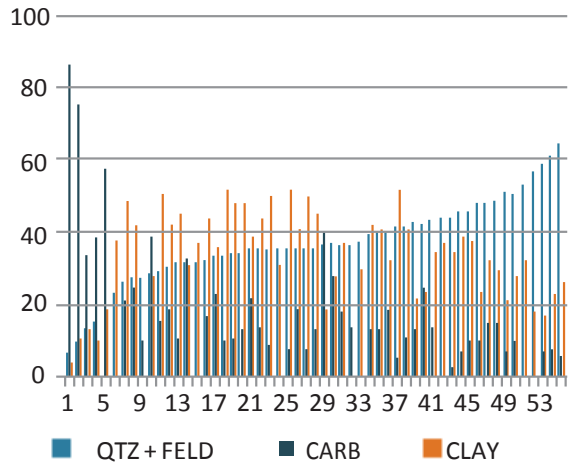


**Fig. 12.7—Main minerals present in the Barnett shale highlight the variability mineralogy.**

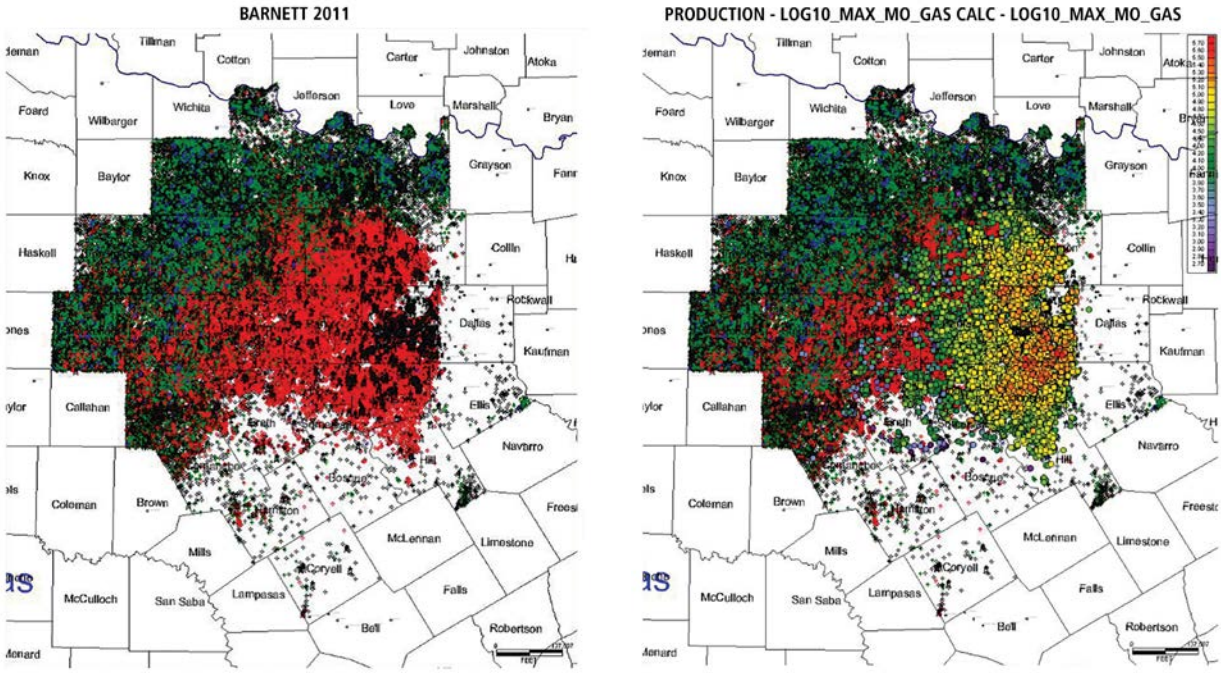


**Fig. 8—Data plot for production wells. (LaFollette and Holcomb 2012.)**

Public and proprietary data from well architecture, completion staging, well tests and treatments and production were also merged into a common database and quality control checked. Examples of quality control checks included checking calculated well azimuth values to be within the known limit of 0-360° and checking to ensure that well length was in the "reasonable" range. Another example is to cross-reference public and proprietary values of the same variable, e.g., fracturing fluid proppant quantity, etc. Many other sanity checks were performed in the course of the study.

Selecting the right production metric(s) is important in data mining. The tradeoff is that the longer time a well must be produced to be selected as a study well, the fewer wells are available for study. Further, results are pushed further into the future. One of the goals of data mining is to use the data to drive significance operational change, leading to selection of production metrics as short term as possible. However, selecting a production metric that is too short may not adequately predict longer-term production.

The authors typically select such short-term metrics as peak monthly rate, and 3-, 6-, and 9-month normalized cumulative production for regression against the 12-month normalized cumulative production. Then the shortest-term metric that

**Fig. 9—Map of well data. (LaFollette and Holcomb 2012.)**

correlates acceptably with 12-month normalized cumulative production is selected.

For the purpose of mapping production data for comparison to geographical, geological, and other trends, bubble-mapping the log10 value of the peak gas rate was used, as shown in Fig. 8 and Fig. 9.

GIS mapping using a log10 production metric and a rainbow color scheme with each shade difference having a 0.1 value indicates a 25% production improvement per increment. This allows rapid pattern-recognition of production trends across the study area. The map can also be used to identify both better and poorer producing areas by displaying, for example, best and worst 10% wells. **Fig. 10**, next, shows such a plot of Barnett vertical wells.

Study of the map shows that locations most favorable for vertical wells were restricted to areas to the northeast of the Viola Pinchout, were generally at some distance from major faults, were geographically separated from the poorest 10% wells, and did not extend to the northwest into the oil leg area of northern Wise and Montague Counties.

Examination of **Fig. 11**, next, shows that favorable locations for best 10% horizontal wells could be on either

side of the Viola Pinchout. An important lesson was that vertical wells could condemn acreage in a shale play that could be productive when drilled and completed as horizontal laterals.

The importance of well azimuth to productivity was fi learned using GIS analysis in an unpublished study circa 2004, and was validated again in 2011 (LaFollette, 2011).

Public and proprietary stimulation treatment data were input stage-wise in their original databases. The data were aggregated and summarized to well level for analysis. It is important to note that stage-by-stage stimulation data would be useful in data mining projects only in the unlikely event that production data were also collected stage-wise.

Examination of the distributions of all variables studied indicated that certain variables were skewed or bimodally distributed. This led to choosing a boosted regression tree method of analysis.

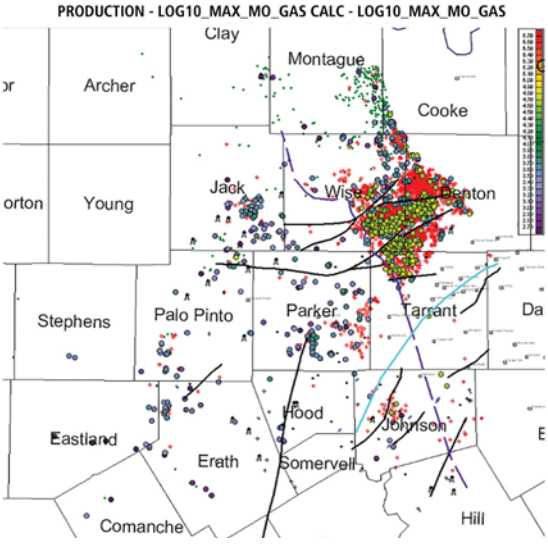


**Fig. 10—Map highlighting the best and worst 10% of Barnett vertical wells with large-scale structure. Fault lines are in black; Viola Pinchout is in purple (dashed). (LaFollette and Holcomb 2012.)**

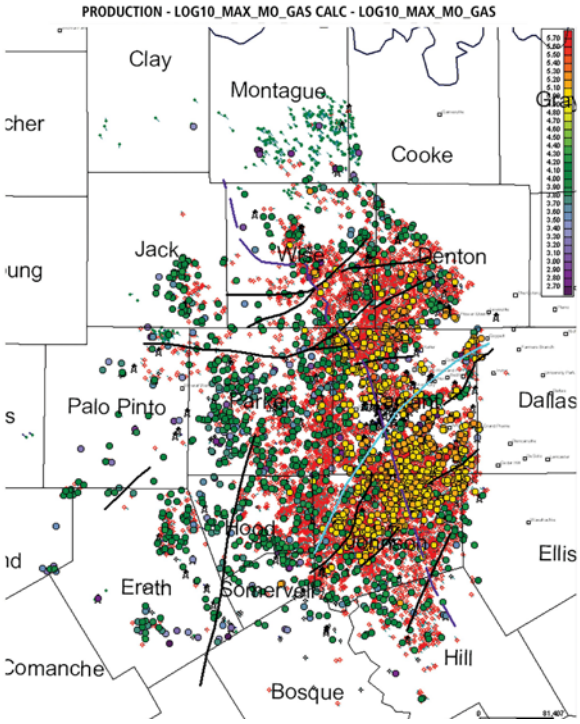


**Fig. 11—Map highlighting favorable locations for the best 10% of Barnett shale horizontal wells on either side of the Viola Pinchout. Fault lines are in black. (LaFollette and Holcomb 2012.)**

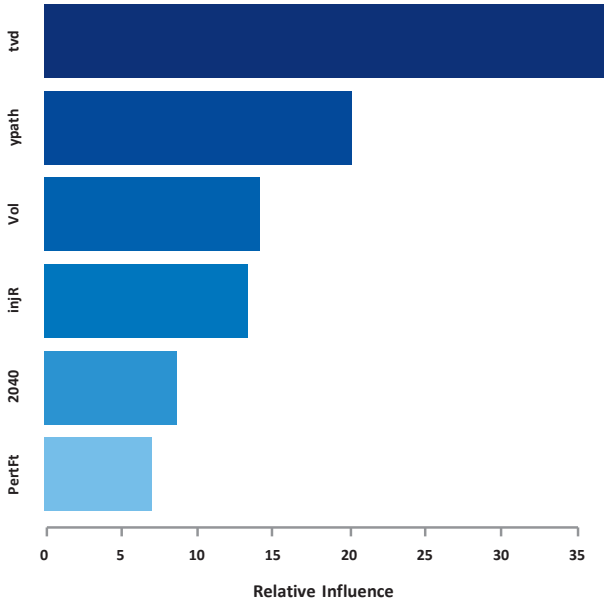


**Fig. 12—Response surface diagram highlighting the importance of both injection rate and treatment fluid volume on maximum gas rate in Barnett study wells. (LaFollette 2013.)**

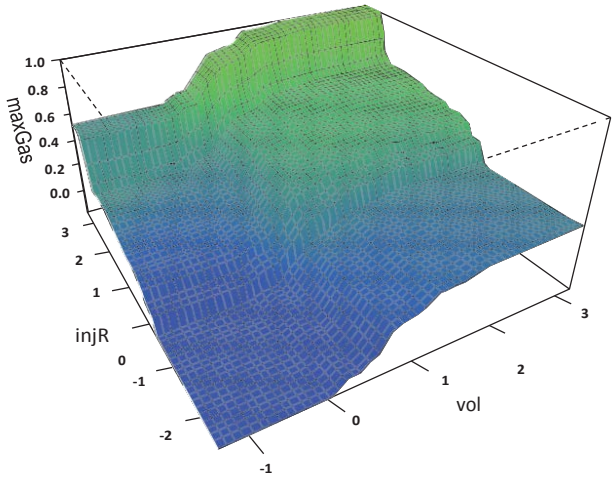


**Fig. 13—Importance plot showing main stimulation influence on maximum gas rate (MMG) target. (LaFollette and Holcomb 2012.)**

The influence plot from the boosted tree analysis using the target production variable maximum monthly gas rate (MMG) is shown in **Fig. 13.**

The bar chart in **Fig. 12** shows the top six variables influence MMG in the study area. True vertical depth (TVD) is most influence followed by N-S location (ypath), fracture treatment fluid volume (Vol), injection rate (InjR), percentage of 20/40 mesh sand, and completed lateral length (PerfFt). Of these, completed lateral length drops below the commonly used double-digit threshold of significance in the dataset used in the study.

The importance of both injection rate and treatment volume to well performance in unconventional reservoirs was discussed early on by King.

Lessons learned may be categorized by variable class.

## Bakken Play

The Bakken formation of the Williston Basin occurs mainly in eastern Montana, western North Dakota, and southern Saskatchewan. This study is focused on wells producing from the Middle Bakken interval of the Bakken-Lodgepole Total Petroleum System south of the 49th parallel (Figure 1, Pollastro, et.al., 2008). It does not include Bakken-Three Forks completions.

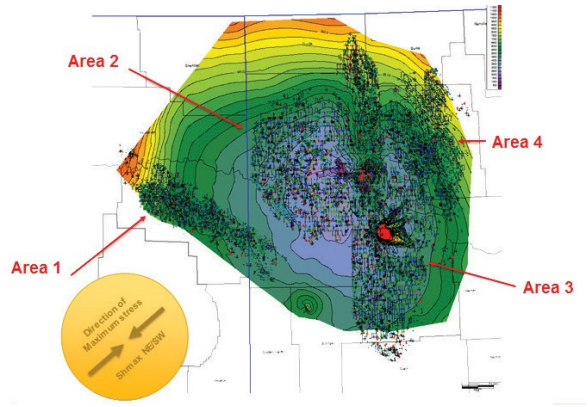


Fig. 12.14—Middle Bakken producing areas across the US side of the basin.

The Bakken shale play discussed here is a shale-sourced, light, tight oil play in which laterals are drilled, completed, and stimulated in the Middle Bakken interval. The Middle Bakken is an interval of mixed carbonate and siliclastic mineral suites, according to producing area (**Fig. 14**).

The goals of this study are to update and expand prior well optimization data mining efforts in the Bakken. There are over 3500-plus horizontal wells included in our Bakken analysis. Our efforts were focused on the impacts of well location, well architecture, completion, and stimulation on production results. One of the production metrics considered is "best month oil production" in the final 12 producing months (BO) in barrels.

The dataset histograms in **Fig. 15** reveal the distribution of individual variables. The target variable BO is highly skewed to the right, while both the surface X location and the cumulative lateral length (CLAT) have bimodal distributions.

A multiple linear model was built upon the Bakken data after variable selection. This model highlights the importance of well location, total fracturing fluid amount pumped in the well, area code, the presence of coarse-mesh proppant in the treatment, and increased proppant concentration in the fracturing fluid as predictors of improved maximum monthly oil production performance.

Linear models (**Table 6**) are straightforward, but need to be built upon many assumptions. The model shows that the fracture fluid volume has a positive impact upon the production. Actually, you can't expect the production to keep climbing with the increased fracture fluid volume in the field. The real-world relationship is much more complex and generally nonlinear.

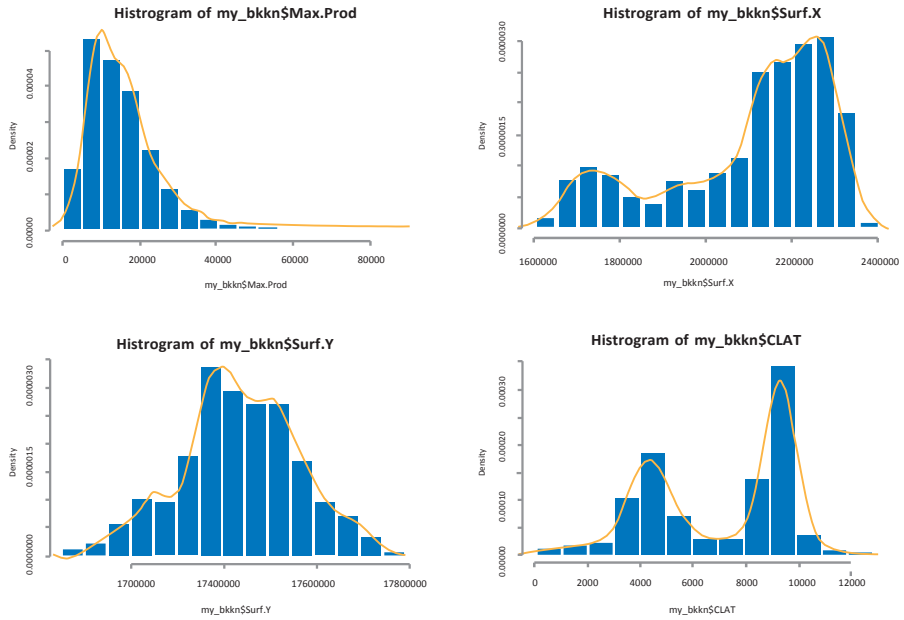


**Fig. 12.15—Histogram of selected variables showing frequency distributions. Note the bimodal distribution of CLAT and Surface X direction.**

Next, we applied the boosted tree method in the analysis (**Fig. 16**). When multiple variables influence the target variable simultaneously, the goal is to learn which ones are the key influence factors. The relative influence is essentially a weighted average of the frequencies a variable is used for splitting trees. The higher value on the influence plot suggests a stronger effect on the target variable. The influence value is proportional to the length of the blue horizontal bar, which is scaled to have a sum of 100.

**Table 6—A multiple linear model for max monthly oil production. Nature logarithm has been applied to some variables to comply with the normality assumption of linear modeling.**

```
Call:
lm(formula = log(Max.Prod) ~ log(Surf.X) + log(Surf.Y) + log(ffa_tot) +
    Area.Code + CPROP + ratio, data = na.omit(my_bkkn[, -c(15:17)]))

Residuals:
    Min      1Q  Median      3Q     Max
-4.5438 -0.3447  0.0430  0.3826  1.8923

Coefficients:
                 Estimate Std. Error t value             Pr(>|t|)
(Intercept)     254.14056   30.86012   8.235 0.000000000000000260 ***
log(Surf.X)      -1.28235    0.45820  -2.799              0.00516 **
log(Surf.Y)     -13.81892    1.69754  -8.141 0.000000000000000561 ***
log(ffa_tot)      0.30765    0.01708  18.011 < 0.0000000000000002 ***
Area.CodeRegion 2  -0.39703    0.08612  -4.610 0.000004182166989809 ***
Area.CodeRegion 3  -0.41930    0.10765  -3.895              0.00010 ***
Area.CodeRegion 4  -0.09823    0.13102  -0.750              0.45349
CPROP1              0.10218    0.02440   4.188 0.000028892970413116 ***
ratio               0.17680    0.01622  10.898 < 0.0000000000000002 ***
---
Signif. codes:  0 '***' 0.001 '**' 0.01 '*' 0.05 '.' 0.1 ' ' 1

Residual standard error: 0.5987 on 3139 degrees of freedom
Multiple R-squared: 0.1743,     Adjusted R-squared: 0.1721
F-statistic:  82.8 on 8 and 3139 DF,  p-value: < 0.00000000000000022
```

**Note:** To avoid the distraction of technical details, we only quoted the results here.

The relative importance plot indicates that well location
is the single most important consideration to predict well productivity from our dataset, followed by the total proppant agent amount. Location and proppant quantity variables show double-digit values on the influence plot, which is a good indicator of their significance. Fracturing fluid amount is only slightly less influential than proppant quantity (high single- digit influence). Proppant quantity is relatively consistent related to the fluid volume. Proppant concentration (in lb/ gal, expressed as a "ratio") has less influence, as does CLAT. Well azimuth through the completed interval (AZM and AZM2) seems to have relatively little influence in the basin- wide model. Note that AZM is well azimuth on a 360° scale and AZM2 is well azimuth on a 180° scale. Neither of these predictors stands out as substantially more significant than the other. The influence of area code indicates that the particular gross field area effects well productivity—which is no surprise to workers in the Middle Bakken play.

More analysis details can be found in the Society of Petroleum Engineers conference paper, SPE 163852 Application of Multivariate Analysis and Geographic Information Systems Pattern-Recognition Analysis to Production Results in the Bakken Light Tight Oil Play, February 2013, available from https://www.onepetro.org/conference-paper/SPE-163852-MS).

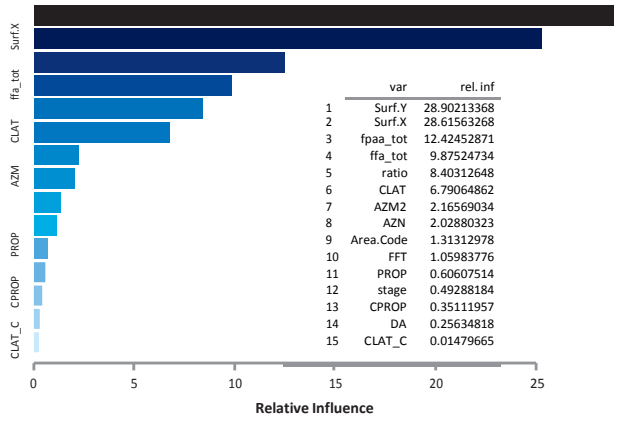


| | var | rel. inf |
|---|---|---|
| 1 | Surf.Y | 28.90213368 |
| 2 | Surf.X | 28.61563268 |
| 3 | fpaa_tot | 12.42452871 |
| 4 | ffa_tot | 9.87524734 |
| 5 | ratio | 8.40312648 |
| 6 | CLAT | 6.79064862 |
| 7 | AZM2 | 2.16569034 |
| 8 | AZN | 2.02880323 |
| 9 | Area.Code | 1.31312978 |
| 10 | FFT | 1.05983776 |
| 11 | PROP | 0.60607514 |
| 12 | stage | 0.49288184 |
| 13 | CPROP | 0.35111957 |
| 14 | DA | 0.25634818 |
| 15 | CLAT_C | 0.01479665 |

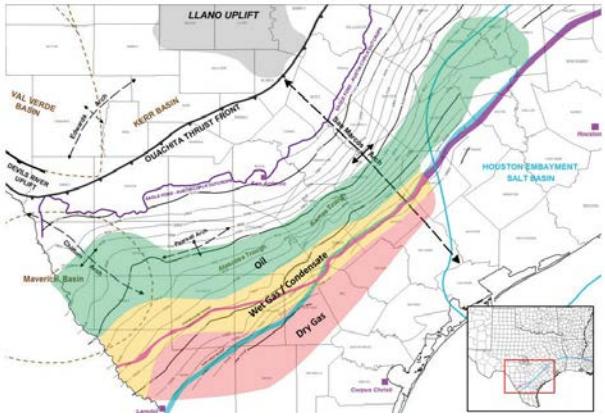


**Fig. 16—Boosted tree model influence plot of Bakken wells with directional surveys across the Williston Basin. The model is based on Approximately 3500 wells**

**Fig. 17—LaFollette 2014. Location map showing the general study area of Eagle For production, South Texas, US. Map courtesy of Momentum Oil and Gas. Used with permission.**

## Eagle Ford Shale

The Eagle Ford formation is a Late Cretaceous Age sedimentary rock formation that underlies much of South Texas. The rocks are mainly organic matter-rich fossiliferous marine shales of the Lower Eagle Ford interval. The play extends over an area of approximately 11 million acres overall, and the main body of the play stretches from the Texas-Mexico border to the eastern borders of Gonzales and Lavaca counties (**Fig. 17**). The northern part of the play (highlighted in green) is in the oil maturation window, and, in addition to producing crude oil, the oil window also contains lesser amounts of natural gas and natural gas liquids (NGLs). Situated to the south and southeast of the oil window, the wet-gas region (highlighted in yellow) produces gas along with high volumes of NGLs. The southernmost region (highlighted in red) contains mostly dry natural gas. Because oil and natural gas liquids command a higher price than natural gas, producers have mostly focused on extracting the formation's oil and NGL resources.

Our Eagle Ford database contains data for around 4,000 horizontal wells from public and proprietary data sources. The wells were divided into three major producing areas. We evaluated the effect of various well parameters upon the production metrics in each area. One of the target variables is maximum monthly oil production within the first 12 producing months (MMO). The available predictors include: X/Y surface locations (which serve as the proxies of the reservoir quality in the absence of large-scale petrophysical analysis data), CLAT, number of fracture stages, well azimuth, drift angle, gas oil ratio (GOR), total fracture fluid volume, total proppant quantity, and proppant concentration.

Exploratory data analysis and a "sanity check" was conducted iteratively for data quality control. Both the histograms and the scatter plot matrix (created from the selected variables shown in the chart, next) suggest the complexity nature of the dataset. A multiple-linear model is not competent to address the non-normality and nonlinearity within the data.

We applied a tree boosting method, gradient boosting, to build our predictive model in each of the three areas from the Eagle Ford play (**Fig. 18**). For producing Eagle Ford wells in Area 1, GOR stands out as the most influential predictor, followed by proppant amount, X-Y-location, and CLAT. The remaining variables are somewhat less influential (**Fig. 19**). **Fig. 12.20** is a matrix scatter plot diagram that suggests the complexity of the dataset.

The relative influence quantifies the overall effect of a variable upon the production, but it can't reveal how this effect could vary when the variable changes its value. As another output from the boosting model, partial dependence plots show the marginal effect of the chosen variable(s) on the target variable. These plots provide useful clues for interpretation.

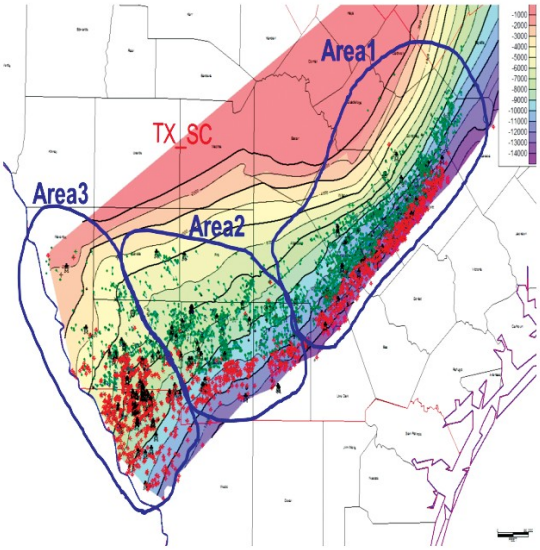


Fig. 18—LaFollette 2014. Map highlighting the study sub- areas within the Eagle Ford play of South Texas, US.

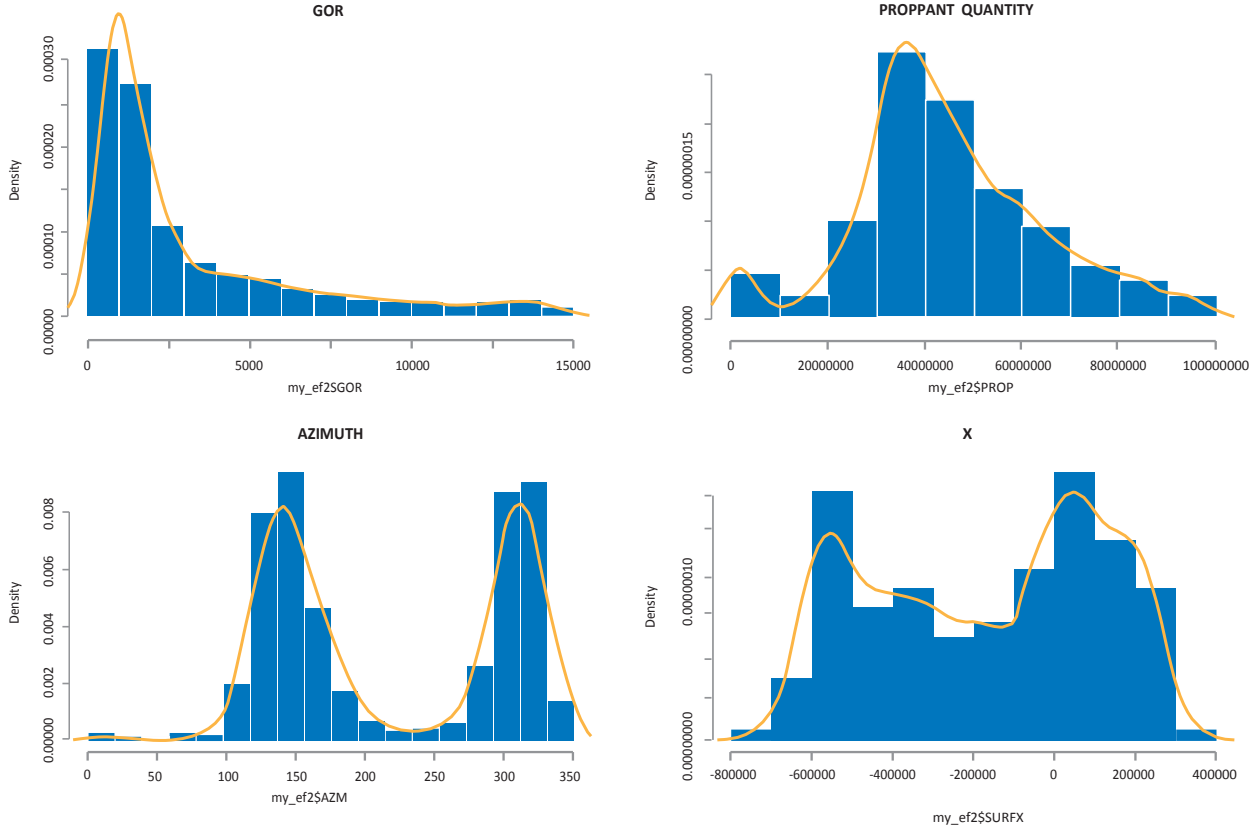


Fig. 19—Histogram suggesting the complexity of the dataset.

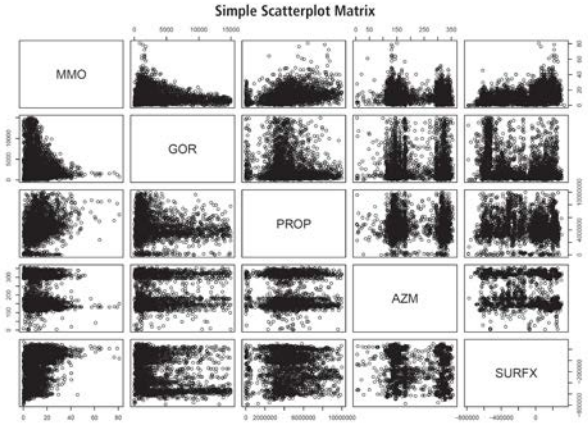


**Fig. 20—Scatter plot matrix suggesting the complexity of the dataset.**

**Fig. 21** shows the partial dependence plots of the top six predictors in the relative influence-ranking list. The upper left, partial dependence plot highlights GOR as a major cause of peak month oil productivity in Area 1. This is reasonable, since the higher GOR means more gas—or less oil—and lower peak production is a natural inference. The partial dependence plot of proppant quantity shows that more proppant is generally associated with increased productivity at least up to the maximum eight-million-plus pound treatments shown in the dataset. Well location is also a key factor that suggests the importance of sweet spots. Last, but not least, according to the partial dependence plot of CLAT (bottom center), the optimal choice of CLAT for peak oil rate is over the range of approximately 3,000 to 6,000 feet. More analysis details can be found from SPE 168628.

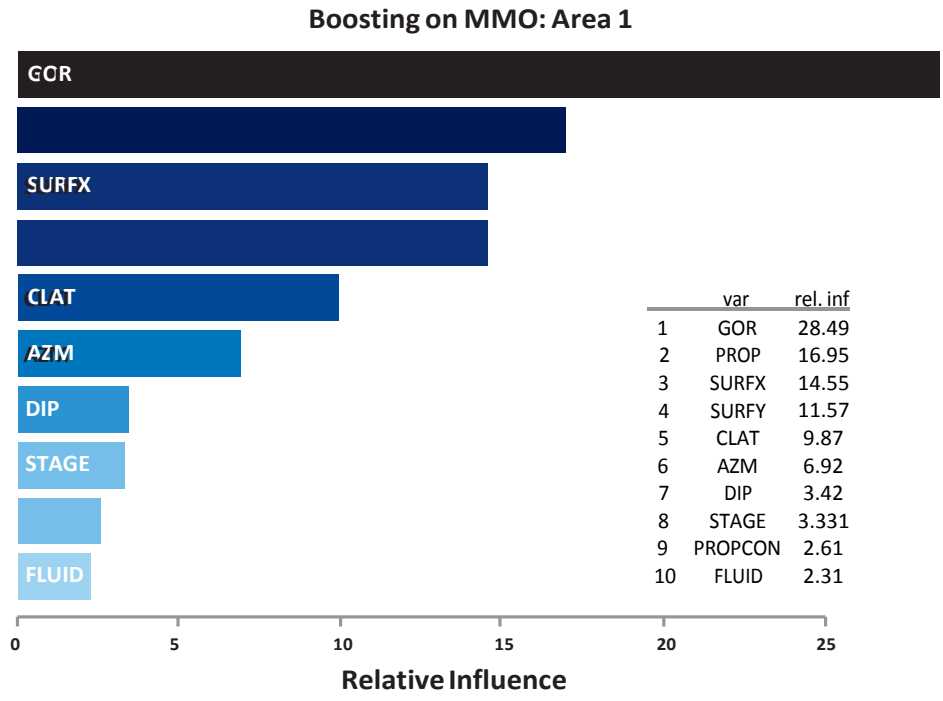


| | var | rel. inf |
|---|---|---|
| 1 | GOR | 28.49 |
| 2 | PROP | 16.95 |
| 3 | SURFX | 14.55 |
| 4 | SURFY | 11.57 |
| 5 | CLAT | 9.87 |
| 6 | AZM | 6.92 |
| 7 | DIP | 3.42 |
| 8 | STAGE | 3.331 |
| 9 | PROPCON | 2.61 |
| 10 | FLUID | 2.31 |

**Fig. 21—Boosting on MMO for Area 1.**

## Concluding Remarks

As stated at the beginning of the chapter, data mining is important in unconventional reservoirs because multi-million dollar decisions are being made daily in the industry, often with limited data to inform the decision-makers. This is largely a result of inadequate reservoir and bounding bed characterization, caused mainly by cost and risk considerations.

While data mining adds important tools to the practitioner's toolbox, we would be remiss if we did not include the following cautions:

- Do follow good statistical and data mining practices. Seek help from a qualified statistician, if statistics is not your field of expertise.
- Understand that "correlation does not imply causation." For any given correlation, there may be an underlying fundamental variable not studied that is the real cause.
- Seek to understand what variables are unknowns, e.g., karst locations relative to Barnett wells, and what impact they would have on interpreting study results.
- Use extreme caution when applying the results of a study outside its original study area. Geological conditions may not have changed, but it is more likely that conditions have indeed changed.
- Do not extrapolate study results. Seeing a trend of increasing treatment volume having a strong influence on increasing well production does not imply that the trend will continue indefinitely.
- Never apply the results of any data mining study blindly.

Data mining allows examination of large numbers of historical well datasets using statistical and machine-learning methods. This approach can be combined with map-based pattern- recognition methods that give the analyst geological and geographical perspective. Together, these tools allow operators, service companies, investors, and others to effectively and efficiently find hidden relationships among variables that may significantly impact their business strategy and decisions.

# Chapter 2

## Definitions and Simple Geometry Models

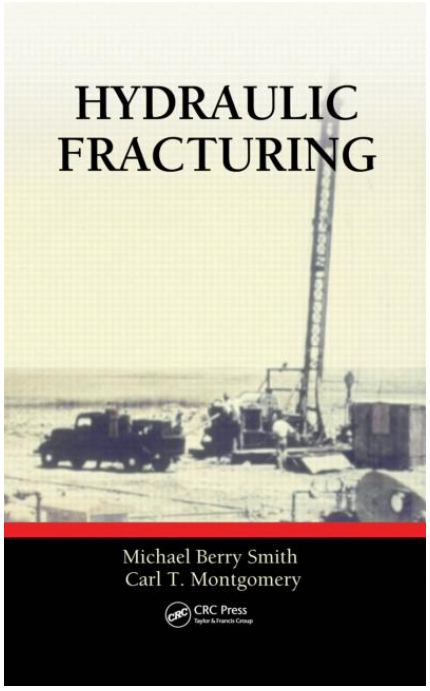


**Hydraulic Fracturing**

*By* Michael Berry Smith, Carl Montgomery Meehan *Park*

This chapter will outline the basic parameters and theory used to build a simple fracture geometry model. It will include simple 2D and P3D fracture geometry models and what the assumptions and limitation of these models are. This includes discussions of material balance, modulus, elasticity, fluid flow, $K_{Ic}$ (rock toughness or the resistance to fracture propagation), fluid loss, and net pressure. Where do these values come from, what do they mean, and what is their impact on the design?

## Introduction

Since its introduction, hydraulic fracturing has been, and will remain, one of (if not *the*) the primary engineering tools for improving well productivity. This is achieved by

- Placing a conductive channel through near-wellbore damage, bypassing this crucial zone
- Extending the channel to a significant depth into the reservoir to further increase productivity
- Placing the channel such that fluid flow in the reservoir is altered

In this last instance, the fracture becomes a tool for true reservoir management including sand deconsolidation management and long-term exploitation strategies. As first visualized, the concept of hydraulic fracturing was quite straightforward. This visualization is described in the following, and in general, for many geologic environments, the basic physics of fracturing are straightforward and well established. Complexity arises from two directions: geologic reality and the inherent multidisciplinary nature of the fracturing process.

Historically, control of fracturing has rested with drilling and operations groups owing to the nature of field procedures using pumps, packers, pressure limits, etc. However, the final results (and thus design) are dominantly a production engineering exercise; also, fracturing cannot be removed from intimate contact with reservoir engineering. At the same time, designing

treatments to achieve the desired results is intimately connected with rock mechanics (which controls fracture geometry, see discussion in the following text), fluid mechanics (which controls fluid flow and proppant placement inside a fracture), and the chemistry that governs the performance of the materials used to conduct the treatmen. However, the design must also be consistent with the physical limits set by actual field and well environments. Also, treatments must be conducted as designed to achieve a desired result (i.e., full circle to the critical role of operations). Proper treatment design is thus tied to several disciplines:

- Production engineering
- Geology
- Rock mechanics
- Fluid mechanics
- Selection of optimum materials
- Operations

Because of this absolutely essential multidisciplinary approach, there is only one rule of thumb in fracturing—there are no rules of thumb in fracturing. The multidisciplinary nature, along with the difficulty in firmly establishing many of the design variables, lends an element of art to hydraulic fracturing. This is not to say that the process is a mystery, nor is it to say that for most cases, the basic physics controlling the process are not defined. It simply says that the multitude of variables involved, along with some uncertainty in the absolute values of these variables, makes sound engineering judgment important.

## What Is Fracturing?

If fluid is pumped into a well faster than the fluid can escape into the formation, inevitably pressure rises, and at some point, something breaks. What breaks is the formation, with the wellbore splitting along its axis due to tensile hoop stresses generated by the high wellbore pressure as illustrated in Figure 1b.

In the earth at any point, the rock is always being acted on by three "principal stresses" (i.e., along axes of the principal stress, the stress is acting purely to compress the rock, with 0 shear stress). (See discussion in Chapter 4, section "In Situ Stress Differences".) In any geologic environment (excepting regions with active tectonics), the vertical stress is one of these three; there are then two horizontal stresses (Figure 2.1a). In most geologic environments (excepting thrust or reverse fault environments), the minimum horizontal stress, $\sigma_{H_{min}}$, is *the*

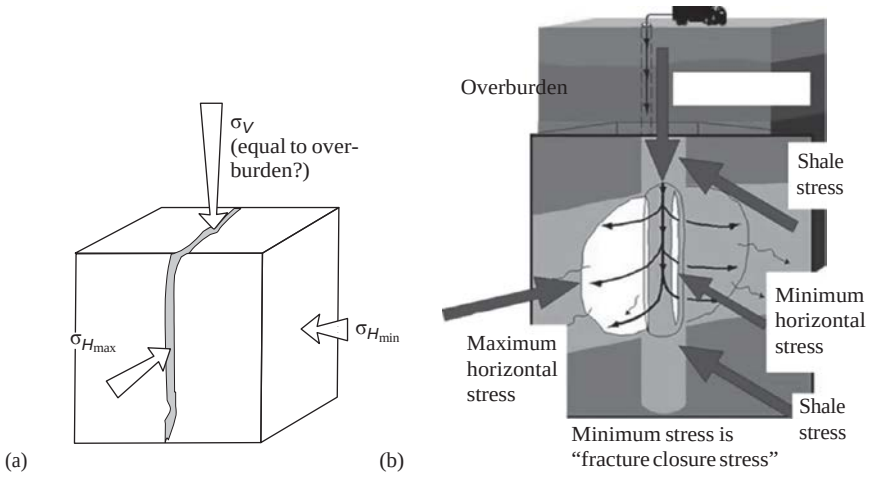


**Figure 1**
Fracture initiation and propagation. (a) Principal stresses. (b) Principal stresses in relation to fracture orientation.

minimum stress, $\sigma_{min}$. This stress is then given a special name—"closure stress, $\sigma_{CL}$, or closure pressure, $P_{CL}$ (the two designations being synonymous)"—since this pressure is where a fracture is mechanically closed.

The simple idea of the wellbore splitting like a pipe (shown as a cartoon in Figure 2b) becomes more complex for cased and/or perforated wells and nonvertical wells. However, in general, the wellbore breaks—that is, the rock fractures—owing to the action of the hydraulic fluid pressure, and a "hydraulic fracture" (a crack help open by hydraulic pressure) is created perpendicular to the minimum stress (i.e., $\sigma_{CL}$). For the ideal case of a vertical well with the smallest stress being the minimum horizontal stress, the initial splitting (or breakdown) results in a vertical planar parting in the earth. The breakdown and early fracture growth expose new formation area to the injected fluid, and thus, the rate of fluid leaking off into the formation starts to increase. However, if the pumping rate is maintained at a rate higher than the fluid loss rate, then the newly created fracture must continue to propagate and grow.

This continued injection at rates higher than the fluid loss rate must create a void in the earth. This might be spherical void, and one could calculate the pressure required to form such a void—it would be a "big" number. The lowest pressure required to open the desired void comes from creating a flat, hot water bottle–shaped void. Thus, we create a void (fracture) that is very large in two dimensions (usually the height and length) and very, very small in the third dimension (the width).

This growth continues to open more formation area. However, although the hydraulic fracture tremendously increases the formation flow area while pumping, once pumping stops and the injected fluids leak off, the fracture

will close and the new formation area will not be available for production. To prevent this, measures must be taken to maintain the conductive channel. This normally involves adding a propping agent to the hydraulic fluid to be transported into the fracture. When pumping stops and fluid flows back from the well, the propping agent remains in place to keep the fracture open and maintain a conductive flow path for the increased formation flow area during production. The propping agent is generally sand or a high-strength, granular substitute for sand.

Alternatively, for carbonate rocks, the hydraulic fluid may consist of acid that dissolves some of the formation, leaving behind acid-etched channels extending into the reservoir .

## Why Fracture?

Hydraulic fracturing may be performed on a well for one (or more) of three reasons:

1. Bypass wellbore damage and return a well to its "natural" productivity.
2. Extend a conductive path deep into a formation and thus increase productivity beyond the natural level.
3. To alter fluid flow in the formation.

In the third case, fracture design may affect and be affected by considerations for other wells (e.g., where to place other wells and how many additional wells to drill). The fracture becomes a tool for reservoir management. Although these three motivations are addressed separately in this section, they frequently overlap.

### Damage Bypass

Wellbore damage reduces well productivity. This damage can occur from several sources, including drilling-induced damage resulting from fines invasion into the formation while drilling and chemical incompatibility between drilling fluids and the formation. The damage can also be due to natural reservoir processes such as saturation changes resulting from low reservoir pressure near a well, formation fines movement, or scale deposition. Whatever the cause, the result is undesirable. Matrix treatments are usually used to remove the damage chemically, restoring a well to its natural productivity. In some instances, chemical procedures may not be effective or appropriate, and hydraulic fracture operations are used

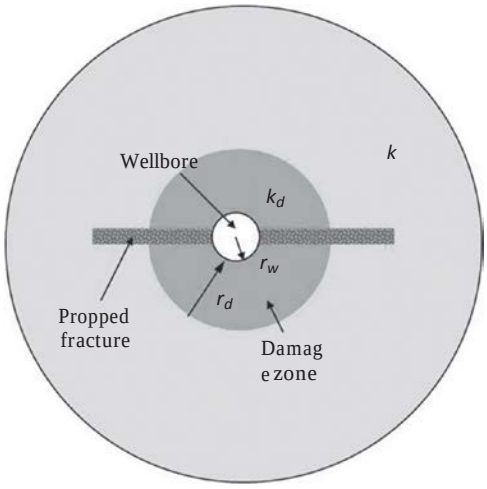


**Figure 2**
High-conductivity fracture bypassing wellbore damage.

to bypass the damage. This is achieved by producing a high-conductivity path through the damage region to restore wellbore contact with undamaged rock (see Figure 2).
For such a fracture, a minimum conductivity ($k_fw - k_f$, the proppant permeability $xw$, the propped width of the fracture) can be established. Just to restore natural productivity, the fracture conductivity must be $k_fw = 2\pi r_w k$. Since damage bypass is mostly for high-permeability formations (with $k$ equal 100s of md or more), the fracture must have a significant conductivity of 2000+ md/ft.

### Increased Productivity

Unlike matrix stimulation procedures, hydraulic fracturing operations can extend a conductive channel deep into the reservoir stimulating productivity beyond the natural level. All reservoir exploitation practices are subject to Darcy's law:

$$Q = \frac{kh}{\mu}\frac{\Delta p}{\Delta x}A \qquad \text{(2.1)}$$

where production rate $Q$ is related to formation permeability $k$, pay thickness $h$, reservoir fluid viscosity $\mu$, pressure drop $\Delta p/\Delta x$, and formation flow area $A$. Reservoir exploitation revolves around manipulating this equation. For example, pressure drop may be increased by using artificial lift to reduce bottom-hole-flowing pressure, water injection to increase or maintain

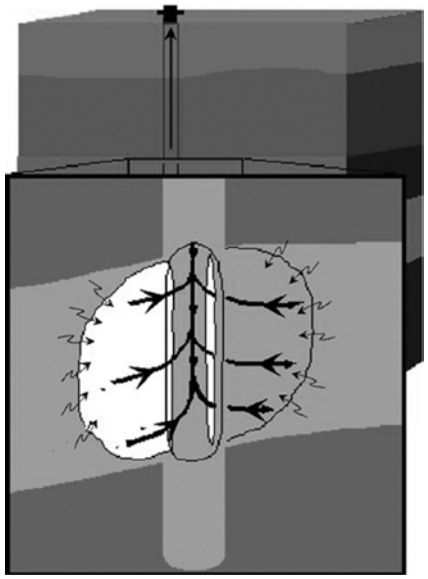

**Figure 3**
Increased formation contact increases production.

reservoir pressure, or both. For other cases, in situ combustion or steam injection is used to reduce reservoir fluid viscosity and thus increase productivity. For fracturing, as pictured in Figure 2.3, operations are on the formation area in the equation, with the increased formation flow area giving the increased production rate. (Strictly speaking, it is the flow shape that is altered, as discussed in detail in Chapter 8.)

This is the classic use of fracturing, to increase the producing rate by bypassing near-wellbore formation damage or by increasing exposure of the formation area and thus stimulating well performance beyond that for no damage. For a single well, treatment design concentrates on creating the required formation flow area to yield increased production at minimal cost. More formally, the design should optimize economic return on the basis of increased productivity and treatment cost.

### Reservoir Management

Along with improving well productivity, fractures also provide a powerful tool for altering reservoir flow. In combination with the other parts of field development, the fracture becomes a reservoir management tool. For example, creating long fractures in tight rock ($k < 0.1$ md) enables field development with fewer wells. However, even fewer wells are required if the fracture azimuth is known and the wells are located appropriately (e.g., not on a regulatory-required square pattern).

The actual philosophy shift for fracturing, from accelerating production from a single well to reservoir management, occurred with the application of massive stimulation treatments in tight gas formations. Although outwardly, a traditional application of fracturing to poorer quality reservoirs, these treatments represented the first engineering attempts to alter reservoir flow in the horizontal plane and the methodology for well placement (Smith, 1979).

Fracturing for vertical inflow conformance (i.e., reservoir management) was successfully used in the Gullfaks field (Bale, 1994), where selective perforating and fracturing were used to optimize reserve recovery and control sand production while maintaining (but not necessarily increasing) the required production rates. This is illustrated in Figure 2.4, where the bottom, lower permeability zone was selectively perforated thus allowing the fracture to initiate in the zone and then grow up into the more permeable zones. Rannoch-1 zone was perforated to create a propped fracture that extends up and into the high-permeability (>1000 md) Rannoch-3 zone. Without fracturing, the entire zone can be perforated, and a low drawdown allows a significant production rate on the order of 20,000 STB/D, sand-free. However, sand production is triggered by water breakthrough in the high-permeability zone (from down-dip water injection). The resulting wellbore enlargement

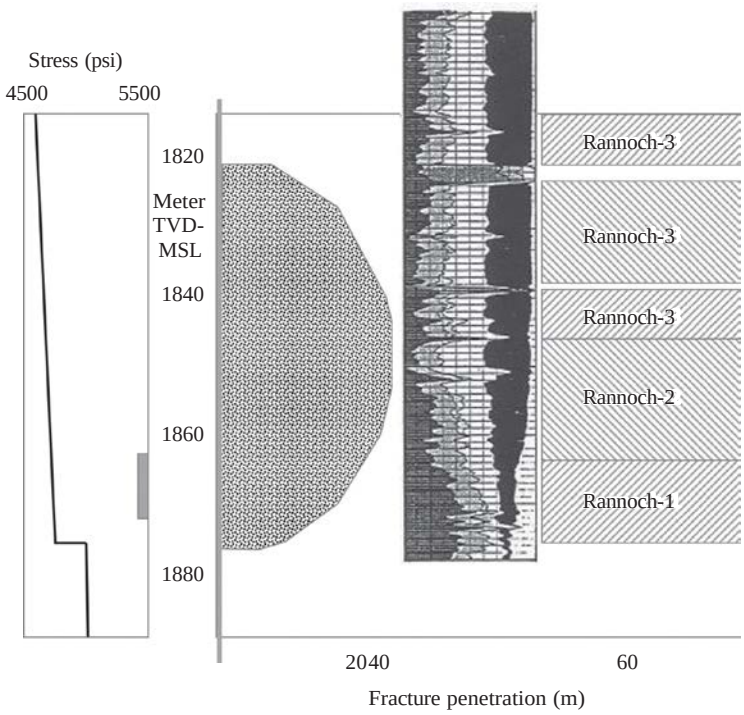


**Figure 4**
Propped fracturing for reservoir management.

caused by sand production acts to stimulate production from the high-permeability zone. To stop sand production, drawdown must be reduced even more. The production is then essentially 100% water coming from the stimulated high-permeability zone, and the well must be abandoned. This further diminishes production from the large reserves found in the deeper zones with lower permeability.

Open or cased hole gravel packing could be used to eliminate the sand production. However, such completions are less than satisfactory for two reasons. First, the deeper, lower-permeability zones can significantly benefit from stimulation. Second, significant scaling occurs with water breakthrough and quickly plugs the gravel pack. The fracturing tool selected to manage the Gullfaks field is termed an indirect vertical fracture completion (IVFC). The IVFC accomplishes several goals:

- Some (although choked) production is achieved from the main zone to enable the well to reach minimum productivity standards.
- Production from the lower, moderate-permeability zone is stimulated, maximizing reserves from this zone.
- Greater drawdown is allowed because the weak high-permeability rock is separated from the perforations, and greater drawdown increases the total rate and significantly increases recovery from the lower zones.
- If the upper high-permeability zone has sand production tendencies (as is typically the case), then producing this zone via the fracture totally avoids the need for sand control.
- Any potential for water breakthrough in the high-permeability zone is retarded, and postwater breakthrough oil production is significantly increased.

To achieve these goals, fracture conductivity must be tailored by synergy between the reservoir and fracture models. Too much conductivity accelerates production and the time to water breakthrough from the high-permeability main zone. Also, too much conductivity, because of surface or tubular limits for the production rate, restricts drawdown on the lower zones, and the desired, more uniform vertical production profile is not achieved. The fracture design goal is not to simply accelerate the rate but to achieve maximum reserves recovery with no sacrifice of rate (as compared with a simple completion in which the entire zone is perforated). Another example of reservoir management is waterflood development utilizing fractures and a “line drive” flood pattern (i.e., one-dimensional [1D] or linear flow from injection fractures to production fractures). Knowledge of the fracture azimuth, combined with conductive fractures (or correctly controlled injection greater than the fracture pressure), results in improved sweep efficiency and enables more efficient field development.

## Treatment Design Variables

As discussed earlier, fracture effectiveness depends on fracture area A, with A equal to fracture height, H, times tip-to-tip fracture length, $L$ ($L = 2x_f$, with $x_f$ being the fracture ½ length or fracture penetration). Fracture conductivity is equally important, with $k_f w$ (the conductivity) being the permeability of the proppant, $k_f$, $x$ the propped fracture width, $w$. Clearly, three of these four parameters are related to fracture geometry (height, length, and width); thus, fracturing is fundamentally about creating desired fracture geometry.

This chapter reviews the basic physics of hydraulic fracture propagation, growth, and final fracture geometry. In addition to leading toward a general understanding of fracture growth, reviewing the basic physical process emphasizes which variables are critical to treatment design. As with all real-world processes, the behavior of hydraulic fractures is a complex function of many variables. However, for most processes, a minor number of these variables dominate the process and control the results. These are the critical parameters or variables, and good information "must" be available for these critical variables in order to understand and design the process (in this case to design a hydraulic fracture treatment). For fracturing, the critical parameters are height, $H$ (or the in situ stresses, which normally control height); Young's modulus, $E$ (the "stiffness" of the rock); fluid loss coefficient, $C$; and (sometimes) fracture toughness (the resistance to fracture propagation), $K_{Ic}$ — that is, HECK. These are the in situ or formation variables. Then, there are the design variables of including pump rate, $Q$, frac fluid viscosity, μ, (as will be discussed in Chapter 9), and treatment volume (Table 2.1). Finally, it should be noted that fundamental fracture geometry models discussed in this section form the theoretical basis for fracturing pressure analysis, which is covered in detail in a separate chapter.

**Table 1**

Major Design Variables

| | |
|---|---|
| **In Situ Design Variables** | |
| $H$ | Gross or total fracture height |
| $H_p$ | Permeable or fluid loss height (sometimes designated as $H_L$) |
| $E$ | Young's modulus |
| $C$ | Fluid loss coefficient |
| $S$ | Spurt loss |
| $P$ | Fracture toughness |
| $K$ | |
| **Treatment Design Variables** | |
| $Q$ | Pump rate |
| μ | Fluid viscosity |
| $t_p$ | Pump time |

### Wellbore Breakdown

The first step in fracturing is to create the initial fracture, to "break down" the wellbore.

### Material Balance

Once the fracture forms, the growth is dominated by material balance—Fracture volume = volume pumped − volume lost to fluid loss. These three volumes can be idealized as

1. Fracture volume = $H \times L \times w$ (where $H$ and $w$ are the average values of height/width).
2. Volume pumped = $Qt_p$ ($Q$ is the constant pump rate and $t_p$ is the total pump time).
3. Volume lost = $4\,CH_pL\sqrt{t_p}$ ($C$ is the "fluid loss coefficient" discussed in the succeeding text, $H_p$ is the permeable or leak-off height, and $L$ is the tip-to-tip length).

and these combine to give

$$L = 2x_f = \frac{Qt_p}{4CH_p\sqrt{t_p} + 2H_pV_{Spurt} + wH} \tag{2.2}$$

providing the very first fracture "model" (see Box 2.1—Fracture Area Equations). In this case, a 1D model where $H$ and $w$ are specified and then length, $L$, can be calculated. That is, when talking about the dimensions for fracture models, it refers to height, $H$; length, $x_f$; and width, $w$. Alternatively, a desired $L$ is specified and this can be solved as a quadratic for $t_p$, that is, a design equation. This "model" then serves to illustrate which are the main variables for frac design.

### Fracture Height, $H$

$H$ and $H_p$ are clearly major variables, and this is seen in Figure 5. The two curves represent two different ways to calculate width. The top curve (Perkins and Kern or PKN) (Perkins, 1961; Nordgren, 1972) assumes $w$ is proportional to the fracture height. The lower curve (Geertsma and de Klerk or GdK) (Khristianovich, 1955; Geertsma and de Klerk, 1969) assumes width is proportional to the tip-to-tip fracture length. Thus, they represent bounds for a true fracture width solution. Either case shows a strong relation between length and height, with, for the PKN model, $L \propto 1/H$. The critical role of height in fracturing is then illustrated in Figure 6. The dominant parameter-controlling fracture height is differences in closure stress between

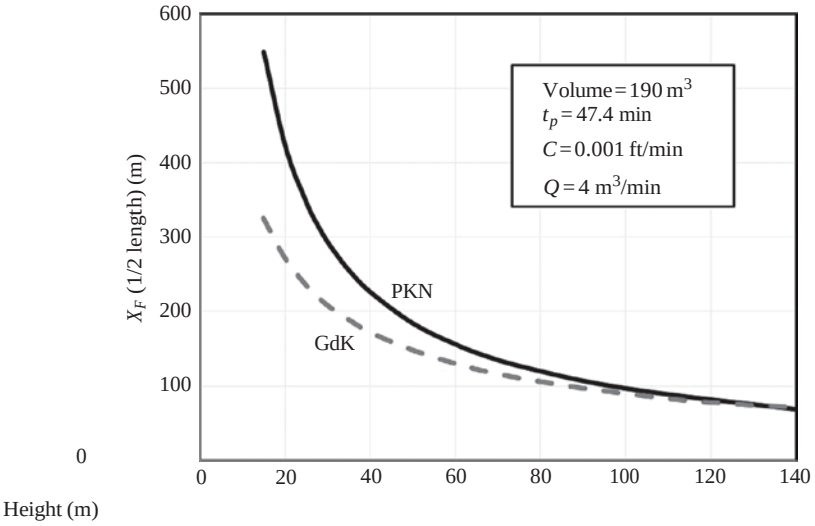


**Figure 5**
Relation between fracture height and fracture length for different width calculations.

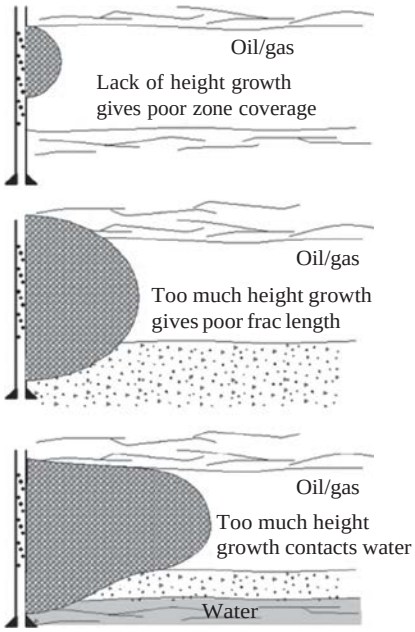


**Figure 6**
Relation between fracture height and fracture length for different width calculations.

## Box 1 FRACTURE AREA EQUATION

Equation 2.4 presented a very simple, 1D model for fracture length growth:

$$L = \frac{Qt_P}{4CH_P\left(t_P + 2H_P V_{Spurt} + wH\right)} \quad (2.3)$$

This is based on a very simple fluid loss model seen in Figure 2.7—the entire tip-to-tip fracture length ($L$) exists for the entire pump time ($t_p$) (giving an absolute maximum for the fluid loss volume). Based on this idea, the total fluid loss volume is given by

$$V_{Loss} = 2CA_P\int_0^{t_P} dt + 2V_{Spurt}A_P = 4CA_P\left(t_P + \frac{2A_P}{p}V_{Spurt}\right) \quad (2.4)$$

where $A_P$ is the permeable or fluid loss fracture area = $LH_P$.

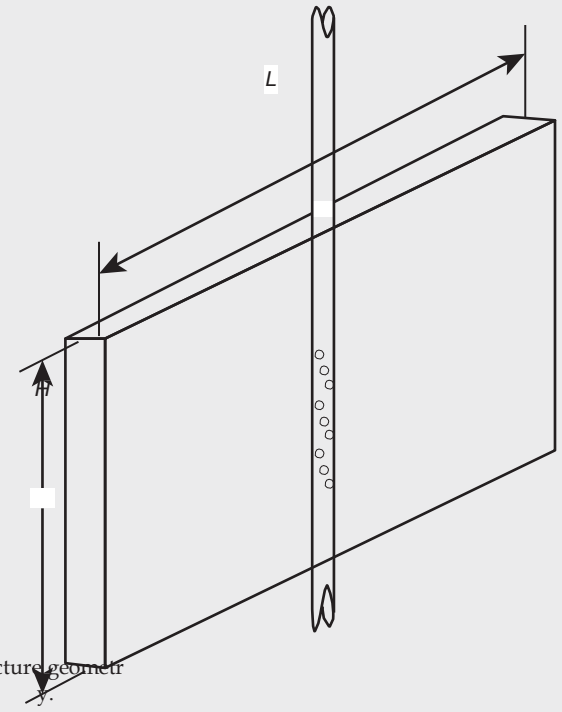


**Figure 2.7**
Idealized fracture geometr

The more rigorous form of this was presented by Carter (1957) including a propagation with time for the solution (this equation implicitly assumes $H = H_P$):

$$A = \frac{Qw}{4\pi C}\left[-\frac{2}{}\left[e^{X^2}\,erfc(X) + \frac{2X}{\sqrt{\pi}} - 1\right]\right], \qquad X = 2C\frac{\sqrt{\pi t_p}}{w} \tag{2.5}$$

Harrington (1979), developed a general relation for fluid volume lost (due to "matrix" or "fluid loss coefficient" loss) as

$$V_{Lost} = 8CA\sqrt{t_p} \tag{2.6}$$

and Nolte (1979) showed that under various bounds the coefficient ($\sqrt{8}$ in this case) of this equation could only vary between 8/3 and $\sqrt{8}$. Thus, for $r_p = 1$ (i.e., $H_P = H$), and no spurt loss,

$$V_{Lost} \cong 3CA\sqrt{t_p} \tag{2.7}$$

reincluding spurt loss revises this equation to

$$V_{Lost} \cong 3CA\sqrt{t_p} + 2V_{Spurt}A \tag{2.8}$$

and using the material balance equation gives

$$A = \frac{Qt_p}{3C\sqrt{t_p} + 2V_{Spurt} + w} \tag{2.9}$$

and this is an excellent approximation to the Carter area equation (still using $H = H_P$) and not that much different from the very simple Equation 2.3.

the pay and over/underlying formations (Warpinski, 1982). This is discussed in more detail in the later chapter—Fracture Design Variables.

### Fluid loss ($C$ and $V_{Spurt}$)

The remaining two variables (other than $w$) control the fluid lost into the formation while the fracture is propagating. These are $C$, the fluid loss coefficient, and $V_{Spurt}$, the "spurt" loss. Normal, matrix, fluid loss is mostly

controlled by a "fluid loss coefficient," $C$, and the rate of fluid loss at any point along the fracture is a function of the square root of time, $C/\sqrt{t}$ (see equation in the succeeding text). This loss coefficient consists of three parts:

1. $C_W$—The polymer in the fluid may form a filter cake on the face of the fracture.
2. $C_I$ or $C_{Viscous}$—The mobility of the fracturing fluid filtrate, leaking off into the formation, may have a mobility ($k_{Effective}/\mu_{filtrate}$) greater than the reservoir fluid and thus form a barrier to fluid loss.
3. $C_{II}$ or $C_{Compressibility}$—Compressing the reservoir fluid for a formation with a viscous oil with low compressibility can act to retard fluid loss.

The mathematical relation between these fluid loss control mechanisms and in situ variables such as $\Delta P$ (frac pressure–reservoir pressure), viscosity of the reservoir fluid, and mobility ($k_{Effective}/\mu_{filtrate}$) of the fluid invading the formation are discussed in Chapter 3.

In most "normal" environments, $V_{Spurt}$, spurt loss, is either 0 or much smaller than the loss due to the loss coefficient. While it does occur, environments where $V_{Spurt}$ might be the dominant parameter in controlling loss are rare.

The matrix fluid loss due to the loss coefficient is governed by the relation

$$q_{Loss} = \frac{2C}{\sqrt{t-\tau(A)}}\, dA \quad (2.10)$$

where $q_{Loss}$ is the fluid loss rate at some piece of fracture area along the fracture face, $dA$, that was first opened at time $t = \tau(A)$. Thus, when the fracture first opens somewhere (say right at the wellbore), fluid loss rate is very large—$C/\sqrt{0}$. Then as time goes on, and the fracture propagates well past the point in question, the rate of fluid loss decreases. This behavior is illustrated in Figure 2.8a. This is discussed in more detail in the later chapter, Fracture Design Variables, and this form of fluid loss is sometimes referred to as "Carter loss."

This behavior is perhaps most readily visualized for the case of fluid loss controlled by a polymer filter cake on the fracture face. At time $t = \tau$, there is no filter cake so the rate of fluid loss is extremely high. Then due to this high loss rate, a short time later, a significant filter cake has formed, and the loss rate is much lower. Then, with time, the filter cake gets thicker, and the loss rate goes down. Typically, this type of fluid loss is characterized by $C_{III}$ or $C_{Wall}$ and is determined from lab testing as pictured in Figure 2.8b. Sometimes, there is a much higher fluid loss rate, which the initial filter cake is formed, and this is idealized as a "Spurt Loss $V_{Spurt}$" (Chapter 3).

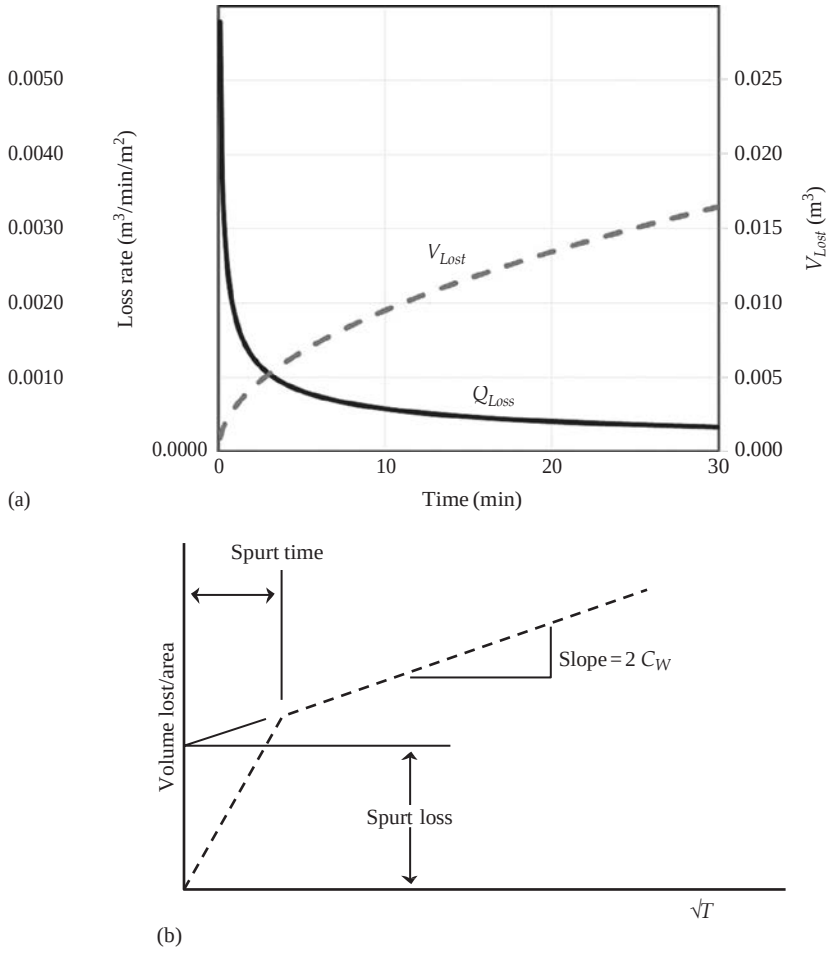


**Figure 8**
Fluid loss rate for matrix loss (one dimension, linear fluid loss, sometimes termed "Carter loss"). (a) Relationship of fluid loss rate vs. time. (b) Relationship of fluid loss per unit area vs. the square root of time.

## Fracture Width

This still leaves width and height as major unknowns. Historically, $w$ was the first parameter to be tackled.

Assume a "slit" in the earth held closed by a far-field stress, closure stress, or closure pressure. Now, begin to increase the pressure in the slit ($P$) until it is greater than this closure pressure. The slit will open into an elliptical crack with the width given by (Sneddon, 1946)

$$w = \frac{2(P - \sigma_{CL})d}{E'} = \frac{2P_{Net}d}{E'} \tag{2.11}$$

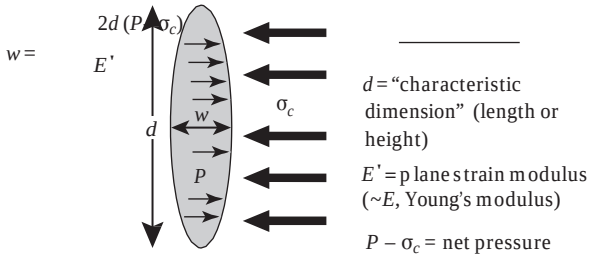


**Figure 9**
Fracture width.

as illustrated in Figure 9. Here, $w$ is the maximum width of the created fracture, $P$ is the fluid pressure inside the fracture and $\sigma_{CL}$ is the minimum in situ stress, $d$ is the dimension of the original slit, and $E'$ is the plane strain modulus ($E' = E/(1 - \nu^2)$) with $E$ being Young's modulus and $\nu$ being the Poisson's ratio for the formation (note that for $\nu = 0.2$, $E'$ only differs by 4% from $E$). For a very high value of 0.35, this effect will be about 15%, which could be important in low modulus formations.

Unfortunately, in terms of our 1D design equation, this does not help much—we simply traded one thing we do not know, $H$, to another thing we do not know, $P_{Net}$. In fact, we made things worse by introducing a brand new variable, $E'$. Despite these drawbacks, this variable change from $w$ to $P_{Net}$ is essential to the problem solution. What we need to know is fracture width; however, we can neither measure nor predict $w$. However, $P_{Net}$ can be both measured and predicted (as discussed in the succeeding text).

The first use of this width equation was by Perkins and Kern (1961). Being with Atlantic Richfield Company, they were primarily involved with relatively low-permeability formations and relatively thin zones. What they wanted were "long" fractures, $L = 2x_f \gg H$. Accordingly, they used height, $H$, for the dimension $d$ in the width equation as seen in Figure 10a. Figure 10b is a bit

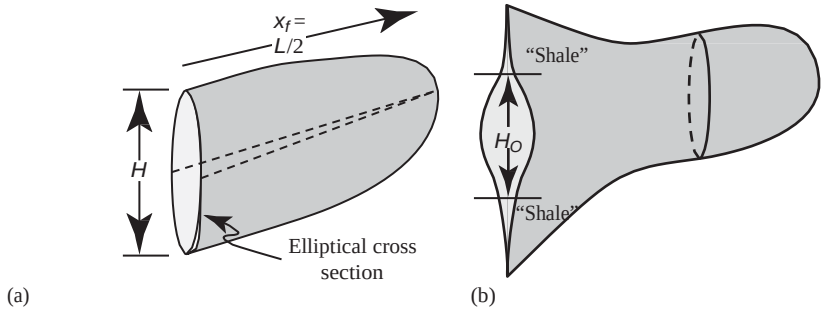


**Figure 10**
Fracture width based on fracture height for a Perkins and Kern (PKN) type fracture ($L \gg H_O$). (a) Geometry of an ideal contained fracture (PKN). (b) Geometry of a more realistic PKN fracture that is growing into a shale.

more realistic view of a long fracture, but still the width defined by the height $H_O$ (height where the fracture first encounters barriers above, and below, and begins to propagate preferentially in length) is approximately correct.

Some years later, Geertsma and de Klerk (1969) applied this width equation somewhat differently; being more concerned with thick Rotliegendes sands with moderate permeability, what was needed was a tall, short frac. Thus, he postulated the tip-to-tip length of the fracture, $L$, was the correct dimension $d$. This gives an ideal fracture as seen in Figure 2.11a, with Figure 2.11b picturing a bit more realistic fracture geometry for a Geertsma–de Klerk (GdK) fracture. Of course, there can also be a radial geometry where $H = L$ as seen in Figure 12 where width is proportional to the radius of the fracture.

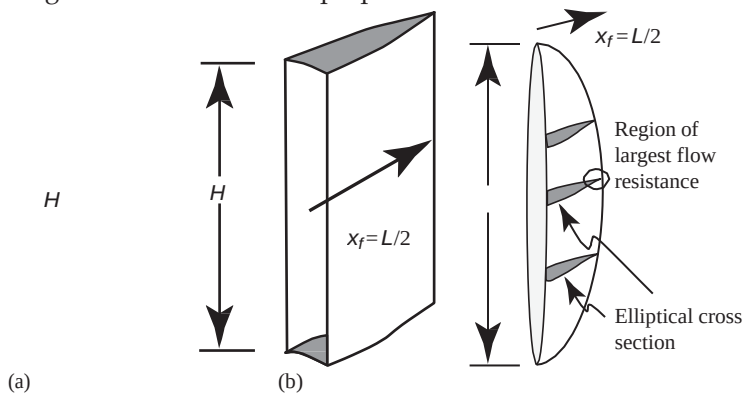


**Figure 11**
Fracture width based on fracture height for a Geertsma–deKlerk (GdK) type fracture ($L \ll H_O$). (a) Geometry of an ideal tall, short fracture (GdK). (b) Geometry of a more realistic GdK fracture.

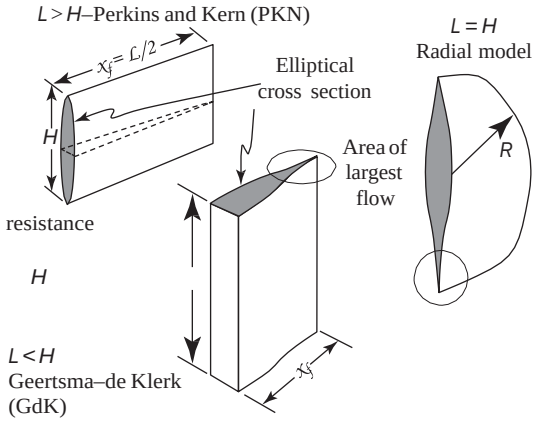


**Figure 12**
Fracture width based on radial geometry ($L = H$)

Coming back to our simple 1D model, we now have two forms of the equation:

$$w = \frac{2P_{Net}d}{E'}, \qquad \bar{w} = \frac{\pi}{4}\frac{2P_{Net}d}{E'}$$

$$(PKN)\quad L = \frac{Qt_P}{4CH_t} + \sqrt{\left(\frac{Qt_P}{4CH_t}\right)^2 + \frac{2CH_V}{\frac{\pi}{2}P_{Net}H_{Spurt}}\frac{P_P}{4}\frac{P_P}{E'}} \tag{2.12}$$

$$(GdK)\quad L = \frac{Qt_P}{4CH_t} + \sqrt{\left(\frac{Qt_P}{4CH_t}\right)^2 + \frac{2CH_V}{\frac{\pi}{4}P_{Net}H_{Spurt}}\frac{P_P}{4}\frac{P_P}{E'}}$$

and assuming one can measure or predict $P_{Net}$ (as discussed in the following text), this has become a 2D model. That is, for a given fracture height, one calculates the width and length; but which model do we use? This started the second big debate in fracturing (the first being vertical vs. horizontal) with some companies choosing the GdK model to build 2D fracture simulators and others using the PKN approach. This argument continued for many years despite Geertsma's (1979) (and others) attempts to sort things out.

Figure 13 compares the widths predicted by these two theories with the width calculated for a 3D, ellipsoidal fracture, and one can think of the $x$-axis (to some extent) as a "time" axis. Initially, the wellbore breaks down and we have a tall, short fracture (and in the figure, the GdK/3D calculations are in perfect agreement). Then with time, the fracture will eventually expand into a radial fracture with $H = L$, and now neither 2D width theory is correct. The fracture may then continue to grow as a radial fracture until eventually, it reaches a barrier formation above and below and begins to propagate preferentially in length. Thus, it finally becomes a PKN fracture.

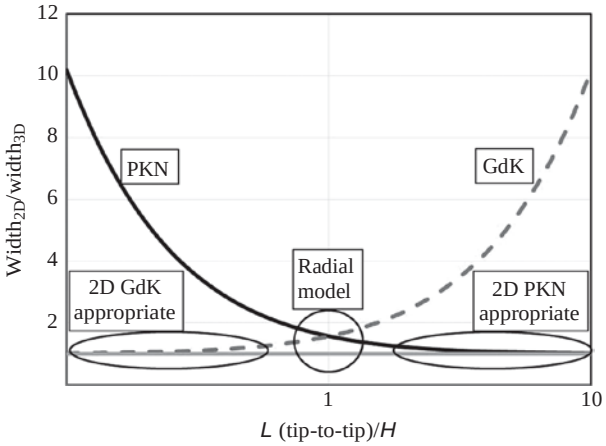

**Figure 13**
2D fracture width calculations versus 3D ellipsoidal fracture width.

## $P_{Net}$ (Net Pressure)

As defined earlier, net pressure is the pressure inside the fracture minus the fracture closure pressure (or closure stress). This $P_{Net}$ is the pressure available to create width and to force propagation—and this is still a big unknown in our 2D fracture aforementioned models. So let's examine the pressure inside a propagating hydraulic fracture—as pictured in Figure 2.14. First (Figure 2.14a), pressure must rise to equal the fracture closure pressure. This provides nothing; it is simply what must be paid (i.e., pumping horsepower fees) in order to play. Next, since the fracture is propagating, there must be some critical net pressure at the tip of the fracture, $P_{Tip}$, to force propagation (Figure 14b).

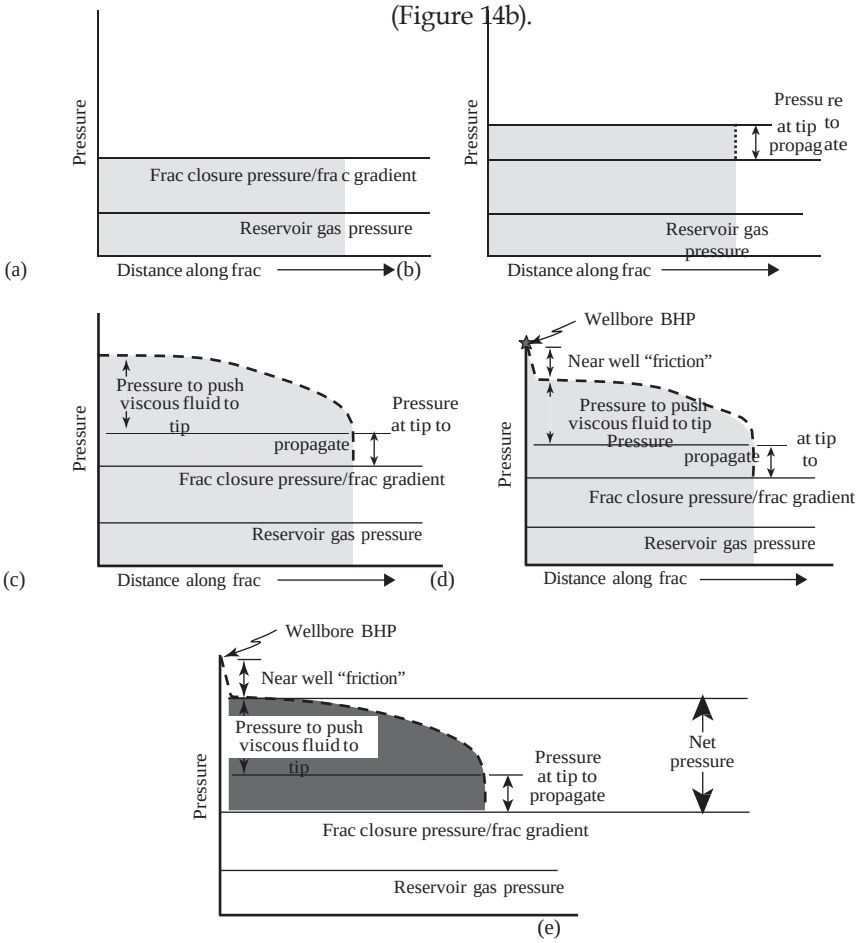


**Figure 14**
Pressure inside a propagating fracture. (a) Reservoir pressure (Pr) + closure pressure (Pc). (b) Pr + Pc + tip pressure (Pt). (c) Pr + Pc + Pt + viscous pressure (Pv). (d) Pr + Pc + Pt + Pv + near wellbore "friction." (e) Pt + Pv is equal to net pressure ($P_{Net}$).

Then, since the fracture tip is propagating, fluid pressure at the wellbore must be higher than pressure at the tip; that is, there is a viscous pressure drop along the fracture (Figure 2.14c). Finally, there may be some near-wellbore pressure drop (perforation friction in the simplest case), giving the final bottom-hole-treating pressure (BHTP) (Figure 2.14d). Out of this entire bottom-hole pressure, all that is of interest is the $P_{Tip}$ and $P_{Viscous}$ as illustrated in Figure 2.14e.

As seen in Box 2.2, these two quantities are given by

$$P_{Viscous} = \frac{E'}{H}\left[\frac{8(Q/2)\mu L}{\pi E'}\right]^{1/4} \qquad P_{Tip} = K_{Ic}\sqrt{\frac{\pi}{412R_{Tip}}} \tag{2.13}$$

However, the final $P_{Net}$ is not simply the sum of these two values. For example, if $P_{Tip}$ is very large, then the fracture is very wide all along its length, and $P_{Viscous}$ becomes negligible. In that case, $P_{Net}$ and thus $w$ (and thus, the frac design) are dominated by $P_{Tip}$ and $P_{Viscous}$ (and thus, pump rate and viscosity) is of negligible concern. The final relation for $P_{Net}$ becomes (Nolte, 1991)

$$P_{Net} = \left[P_{Tip}^{e} + P_{Viscous}^{e}\right]^{1/e}, \quad e = n + 2 = 3 \text{ (for Newtonian fluid)} \tag{2.14}$$

Now, assuming that $R_{Tip} = H_O/2$ (where $H_O$ is the fracture height when the fracture first reaches a barrier to vertical growth at top and bottom), our 2D design model becomes (for a long-confined height, PKN, geometry, Newtonian, $n = 1$, fluid, and using oil field units) (for a non-Newtonian fluid see the work by Nolte cited earlier)

$$P_{Viscous}(\text{psi}) = 0.0115\frac{E'(\text{psi})}{H_O(\text{ft})}\left[\frac{Q(\text{bpm})\mu(\text{cp})x_f(\text{ft})}{E'(\text{psi})}\right]^{1/4},$$

$$P_{Tip} = K_{Ic}\left(\text{psi}\sqrt{\text{in}}\right)\sqrt{\frac{\pi}{24H_O(\text{ft})}}$$

$$P_{Net}(\text{at well})(\text{psi}) = \left[P_{Tip}^{e} + P_{Viscous}^{e}\right]^{1/e} \tag{2.15}$$

$$w = \frac{2P_{Net}H_O}{E'}, \quad \bar{w} = \frac{\pi}{4}\frac{2P_{Net}H_O}{E'}$$

$$2x_f(\text{ft}) = \frac{Q(\text{bpm})t_P(\text{min})}{4C(\text{ft}/\sqrt{\text{min}})H_P(\text{ft})2x_f\sqrt{t_P} + 2H_P 2x_f V_{Spurt} + \frac{\pi}{4}\frac{2P_{Net}H_O^2}{E'}}$$

defining the major fracture design parameters.

Note that the use of the basic relations for treatment design is described in Chapter 18.

### Box 2.2 $P_{Viscous}$ AND $P_{Tip}$

For predicting $P_{Viscous}$, begin with the equation

$$\left(\frac{dP_{Net}}{dx}\right)_{\max} = \frac{64(Q/2)\mu}{\pi H w^3} \tag{2.16}$$

for viscous fluid flowing (laminar flow) down an elliptical conduit (Lamb, 1932). Combining this with the basic equation for fracture width (Sneddon, 1946),

$$w_{\max} = \frac{2P_{Net}H}{E'} \tag{2.17}$$

gives

$$\frac{dP_{Net}}{dx} = \frac{8(Q/2)\mu E'^3}{\pi H^4 P_{Net}^3} \rightarrow P_{Net}^3\, dP_{Net} = \frac{8(Q/2)\mu E'^3}{\pi H^4}\, dx \tag{2.18}$$

Integrating this from the tip of the fracture (where $P_{Net}$ is assumed = 0) back to the wellbore gives

$$P_{Net} = P_{Viscous} \Big|_{\text{wellbore}} = \frac{E'}{H}\left[\frac{8(Q/2)\mu x_f}{\pi E'}\right]^{1/4} \tag{2.19}$$

where in this case, this equals $P_{Viscous}$ since the assumption was $P_{Net} = 0$ at the fracture tip. In oil field units of $Q$ (bpm), $\mu$ (cp), $x_f$ (ft), $H$ (ft), and $E'$ (psi), this becomes

$$P_{Net} = P_{Viscous} = 0.0115\frac{E}{H}\left[\frac{Q\mu x_f}{E'}\right]_{1/4}. \tag{2.20}$$

Note that this is a PKN solution, so $H \gg L$ is assumed. Also, this assumption makes no correction for changes in $Q$ along the fracture, that is, no fluid loss, a limited, illustrative, solution.

While (as discussed in the following text) basic elastic fracture mechanics does not strictly apply to a hydraulically driven fracture, the basic concept is still of value. That says that for a radial fracture, the required propagation pressure, $P_{Tip}$, is given by

$$P_{Net} = P_{Tip} = K_{Ic}\sqrt{\frac{\pi}{4R}}, \quad \text{or} \quad = K_{Ic}\sqrt{\frac{\pi}{48R_{Tip}}} \tag{2.21}$$

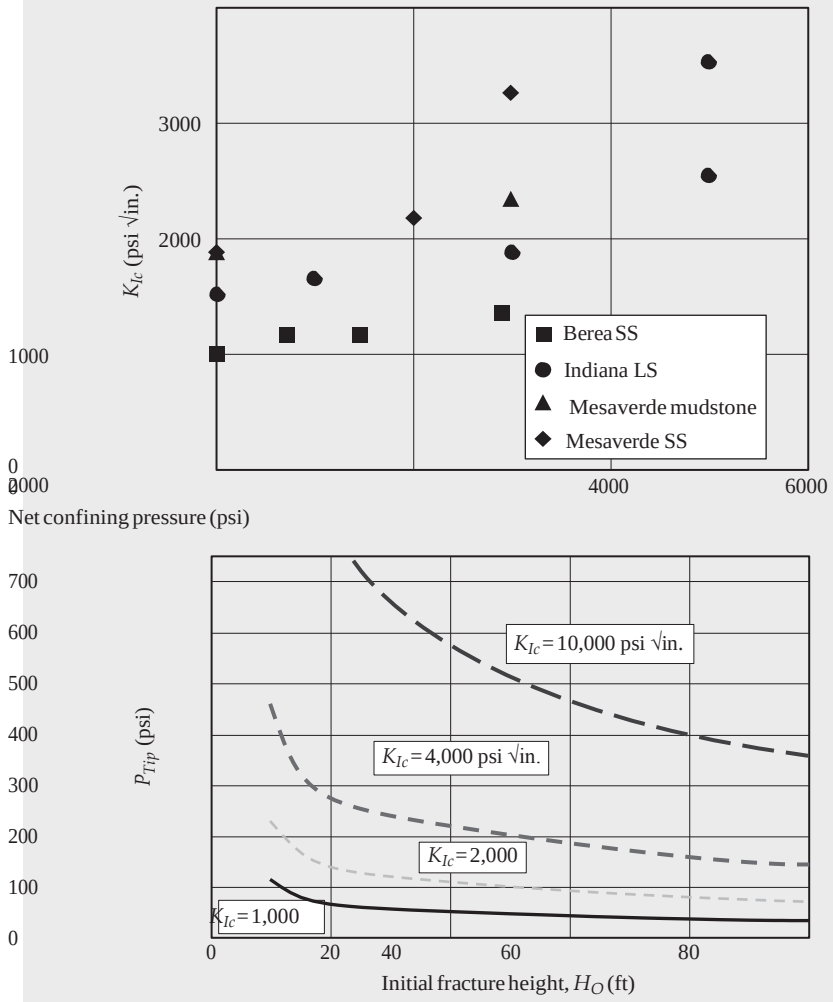


**Figure 15**
Typical $K_{Ic}$ values and the resulting $P_{Tip}$.

where the second equation is in oil-field units $K_{Ic}$ (psi √in.), $R_{Tip}$ (ft), and $P_{Tip}$ (psi). Still ignoring that this elastic fracture mechanics description is not strictly applicable, typical values for $K_{Ic}$ are seen in Figure 2.15 (replotted from several references as described in Chapter 3). This figure also shows predicted $P_{Tip}$ values for a range of $R_{Tip}$ (tip radius), and it is noted in passing that indeed, $P_{Tip}$ values on the order of 100–200 psi are routinely measured in the field from step-rate tests in "hard rock" (i.e., cemented, consolidated formations with modulus values of 1 + $\times 10^6$ psi).

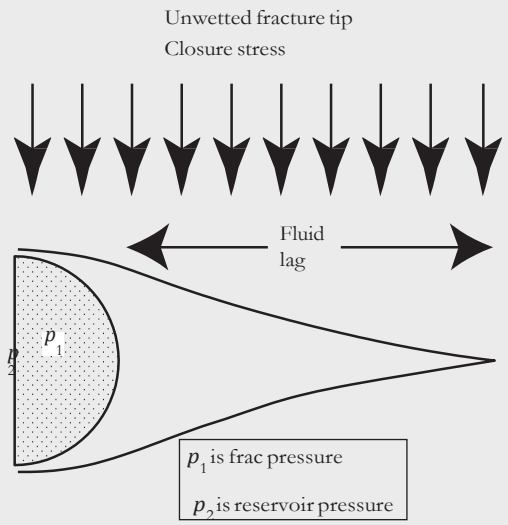


**Figure 16**
Unwetted fracture tip (or fluid log zone).

As espoused by Khristianovitch (1955) and measured in semifield scale experiments by Warpinski, there should be an unwetted region at the tip of a propagating hydraulic fracture as pictured in Figure 16. It is this unwetted tip that dominates $P_{Tip}$ (for "rock"), and an apparent fracture toughness $K_{Ic\text{-}App}$ can be related to this behavior with $K_{Ic\text{-}App}$ proportional to

$$K_{Ic-App} \propto (\sigma_{CL} - P_{Unwetted\_Tip}) \times \sqrt{d} \qquad (2.22)$$

where $d$ is the length of the unwetted zone and $P_{Unwetted\_Tip}$ is the pressure in this region. For a permeable formation, this might have a maxi- mum value of reservoir pressure, with the exact value depending on the $k/\mu$ of the formation and the velocity of the crack tip. For an impermeable rock, $P_{Unwetted\_Tip}$ may approach a vacuum. However, this apparent toughness is seldom much greater than the typical "rock mechanics" toughness values seen earlier (see Chapter 3).

The final net pressure at the wellbore, $P_{Net}$", is then related to $P_{Viscous}$ and $P_{Tip}$. However, it is *not* the simple sum of these two values (Nolte, 1991). Rather, if fluid viscosity is very high, then pressure drop along the fracture, $P_{Viscous}$, becomes so large that $P_{Tip}$ becomes irrelevant to the problem. Conversely, if $P_{Tip}$ is very high, the fracture width is large all along the length, and the $P_{Viscous}$ becomes negligently small. This can be written as

$$P_{Net} = \left\lceil P_{Tip}^{\,e} + P_{Viscous}^{\,e} \right\rceil^{1/e}, \quad e = n' + 2 = 3 \text{ (for Newtonian fluid)} \qquad (2.23)$$

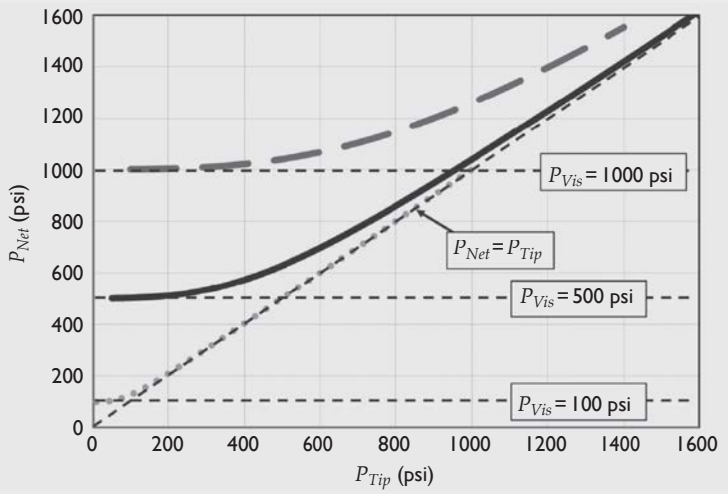


**Figure 17**
$P_{Tip}$ and $P_{Viscous}$ combining to give $P_{Net}$ (at wellbore) (Newtonian fluid, $n' = 1$).

where $n'$ is the non-Newtonian $n$ $n'$ for the fracturing fluid. For a Newtonian fluid, $n' = 1$. This behavior is illustrated in Figure 2.17. For a very low value of $P_{Viscous}$ (maybe due to a very low modulus such as found in many high-permeability, frac–pack applications) of maybe 100 psi, reasonable values of $P_{Tip}$ (maybe 100–300 psi) quickly dominate net pressure; this $P_{Net}$ dominates fracture width and ultimately frac design. For higher values of $P_{Viscous}$, it takes unusually high values of $P_{Tip}$ to have any significant impact on frac design.

# Chapter 3

## Microorganisms in the Oil and Gas Industry

Ian M. Head

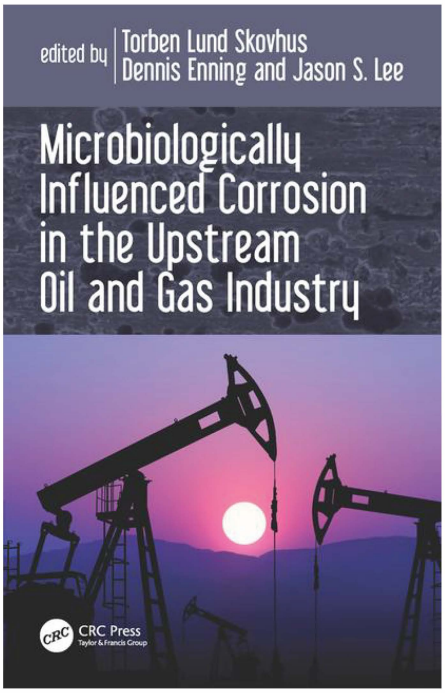


**Microbiologically Influenced Corrosion in the Upstream Oil and Gas Industry**

*By* Torben Lund Skovhus, Dennis Enning, and Jason S. Lee

**ABSTRACT**

The deep biosphere is the largest microbial biome on the planet. Being remote, difficult to sample, and refractory to direct observation, it can often seem esoteric and detached from practical relevance. Those working in the oil and gas industry know from difficult and costly experience that this view of the deep biosphere could not be further from the truth. Petroleum systems provide the most tangible evidence that the deep biosphere should not be relegated to a curious scientific oddity. The operational and economic consequences of microbial activity in petroleum systems are immense and a testament to the power of the deep biosphere and its very direct impact on human activities.

Petroleum reservoirs harbor a diverse array of microorganisms, which, on production *and* geological time scales, influence the properties and quality of emplaced oil and affect its production and ultimately its value. Heavy oil formation over tens of millions of years, sulfide formation leading to souring, microbially influenced corrosion, and the potential to enhance oil recovery all have a central microbiological component, and in some cases, there may be microbiological solutions to detrimental processes that occur during petroleum production. Here, the range of organisms associated with petroleum systems is explored. A particular emphasis is placed on the activities they catalyze and which underline their practical importance for good or ill in the oil and gas industry.

## INTRODUCTION: THE DEEP BIOSPHERE AND THE PETROLEUM RESERVOIR MICROBIOME

Subsurface sediments (defined by Whitman et al. 1998 as terrestrial habitats below 8 m and marine sediments below 10 cm) represent the largest biome on the planet with the latest estimates indicating that the deep biosphere comprises $4.7 \times 10^{29}$ cells (Kallmeyer et al. 2012). Whitman's analysis considered unconsolidated sediment to a maximum depth of 4 km, which equates to a sediment volume of $1.2 \times 10^{17}$ $m^3$. Four kilometers is considered to be the limit of the deep biosphere as this corresponds to the approximate average depth of the 122°C isotherm (Garland 1971; Kallmeyer et al. 2012), which is close to the currently known maximum temperature for life (Takai et al. 2008). However, microbial life in the deep subsurface and specifically in deep petroleum reservoirs may cease at lower temperatures (Wilhelms et al. 2001) probably due to the constraints of extreme energy limitation in deep subsurface sediments (Wilhelms et al. 2001; Jørgensen and D'Hondt 2006; Head et al. 2014).

Petroleum reservoirs occur from the Earth's surface to a depth of almost 6 km with the majority found at depths of less than 4 km (Ehrenberg and Nadeau 2005). The majority of petroleum reservoirs therefore are clearly within the bounds of the deep biosphere. The first evidence that life existed in petroleum reservoirs was reported in 1926 when Bastin reported the occurrence of sulfate-reducing bacteria in produced waters from a petroleum reservoir in the Illinois Basin (Bastin 1926), and though there have always been concerns regarding the provenance of microorganisms isolated from deep subsurface environments, and some organisms detected in these systems are almost certainly contaminants, it now seems clear that deep sub- surface sediments, including petroleum reservoirs, harbor diverse indigenous microbial communities (Magot et al. 2000; Magot 2005; Wentzel et al. 2013). Irrespective of their source, the microorganisms that constitute the petroleum biosphere have significant consequences for petroleum systems, both with respects to the predrill, in situ activities of indigenous organisms and the response of either indigenous or contaminating/deliberately introduced organisms during production.

The excellent review of Wentzel and coauthors (2013) and several chapters in Ollivier and Magot (2005) provide a comprehensive survey of the microorganisms isolated from or identified in petroleum reservoirs. Readers wishing more detailed information are directed to these sources. From these review articles, it is clear that anaerobic thermophiles from the Thermotogae are common in high-temperature petroleum reservoirs (e.g., *Petrotoga*, *Thermotoga*, *Geotoga*, *Kosmotoga*, *Oceanotoga*, and *Thermosipho*), and *Petrotoga* and *Geotoga*, for example, have only been isolated from petroleum reservoirs, suggesting these are indigenous petroleum reservoir specialists. Firmicutes, such as *Thermoanaerobacter*, *Geobacillus*, *Desulfotomaculum*, *Caldanaerobacter*, *Mahella*, and *Bacillus* (Wentzel et al. 2013) are also commonly reported among petroleum reservoir isolates. *Deferribacter* spp., *Thermus* spp., *Anaerobaculum* spp., and *Thermovirga* spp. too have been isolated from a range of petroleum reservoirs. Significantly, in the context of reservoir souring and corrosion, a range of delatproteobacterial sulfate reducers have also been isolated frequently from

petroleum reservoirs (Magot et al. 2000; Magot 2005), and many types of SRB have been found only in petroleum reservoirs and not other environments, strongly suggesting that they are part of an indigenous microflora (Birkeland 2005).

Many mesophilic bacteria have also been isolated from petroleum reservoirs and have been inferred to be indigenous based on their growth at in situ salinity (Magot 2005). Mesophilic, halophilic fermentative bacteria from the genus *Haloanaerobium*, for example, have been isolated from petroleum reservoirs as has *Fusibacter paucivorans* and *Spirochaeta smaragdinae* (Ollivier and Cayol 2005). A range of heterotrophic iron- and nitrate-reducing bacteria are also known from petroleum reservoirs (e.g., some members of the genera *Denitrivibrio*, *Garciella*, *Geobacillus*, *Marinobacter*, *Petrobacter*, *Shewanella*, and *Deferribacter* as mentioned above) and sulfide-oxidizing nitrate-reducers from the *Epsilonproteobacteria* (Gevertz et al. 2000).

In addition to bacteria, a range of archaea are also known to inhabit petroleum reservoirs. *Thermococcus* spp., *Pyrococcus* spp., and *Archaeoglobus* spp., all Euryarchaeota, have been isolated from high-temperature petroleum reservoirs as have thermophilic methanogens. Interestingly, it is exclusively hydrogenotrophic methanogens that have been isolated from high-temperature petroleum reservoirs, including members of the genera *Methanoculleus*, *Methermicoccus*, *Methanothermobacter*, and *Methanococcus* (Jeanthon et al. 2005; Wentzel et al. 2013). This has prompted the suggestion that syntrophic acetate oxidation to hydrogen and $CO_2$ may be an important process in high-temperature petroleum reservoirs (Jeanthon et al. 2005), and indeed *Thermacetogenium phaeum*, a known syntrophic acetate-oxidizing bacterium, has been identified in a high-temperature Chinese oil reservoir. Interestingly, a small number of culture-independent studies have detected members of the Methanosarcinales in high-temperature systems (Orphan et al. 2000), and Methanosarcinales sequences have been recovered from low-temperature reservoirs (Grabowski et al. 2005; Piceno et al. 2014), and in at least one low-temperature Alaskan reservoir, Methanosarcinales appeared to be the dominant group of methanogens (Pham et al. 2009).

## THE PETROLEUM RESERVOIR BIOSPHERE

The organisms found in petroleum reservoirs and reservoir fluid chemistry (e.g., presence of methane, sulfide, volatile fatty acids, and gas isotope data) indicate that the petroleum reservoir biosphere is primarily anoxic. In instances where formation waters are low in sulfate and seawater injection for secondary recovery has not been practiced, the petroleum reservoir biome is primarily driven by fermentation reactions that deliver hydrogen, carbon dioxide, and acetate to methanogens. In high-temperature reservoirs with archaeal communities dominated by hydrogenotrophic methanogens, it is also likely that syntrophic acetate oxidation plays a significant role in the anaerobic food chain of petroleum reservoirs. Interestingly, many of the fermenting archaea and bacteria found in petroleum reservoirs have the capacity to reduce oxidized iron and/or elemental sulfur and thiosulfate, for example (e.g., *Thermococcus*, *Thermotoga*, *Halanaerobium*; Jeanthon et al. 2005; Ollivier and Cayol 2005), suggesting that a degree of metabolic versatility is an important adaptation even in the rather static environment of an untapped

petroleum reservoir.

Where sulfate is abundant, sulfate reduction is a significant driver of the deep petroleum biosphere, and a wide range of unique sulfate-reducing bacteria, from three phyla (*Proteobacteria*, *Firmicutes*, *Thermodesulfobacteria*) are known from petroleum reservoirs as are euryarchaeotal *Archaeoglobus* spp. (Birkeland 2005). However, often *Archaeoglobus* spp. are not considered to be indigenous to petroleum reservoirs and are thought to be introduced with injected seawater (Birkeland 2005; Jeanthon et al. 2005). While the largest pool of carbon in petroleum reservoirs is clearly hydrocarbons (principally saturated and aromatic hydrocarbons), there are many other potential carbon and energy sources in petroleum reservoirs. These include organic acids, such as acetate, propionate, and butyrate, which can be present at tens of millimolar concentrations (Barth 1991). Moreover, hydrogen may act as an electron donor, driving sulfate reduction and methanogenesis in petroleum reservoirs with organic or inorganic carbon serving as carbon sources. In the case of $CO_2$ reduction, either for methanogenesis or biosynthesis, the carbon dioxide and hydrogen requirements can be met purely by the fermentation of organic substrates. However, it is possible that hydrogen in petroleum reservoirs may be derived from other sources, such as aromatization of organic compounds, serpentinization in deep hot rocks, or thermal maturation of organic matter in source rocks and transport of the hydrogen generated to the reservoir (Head et al. 2003).

The slow microbial utilization of hydrocarbons in petroleum reservoirs on geological time scales leads to one of the most dramatic expressions of the petroleum reservoir biosphere, if not the deep biosphere more generally: the occurrence of heavy oil. Heavy oil results from the activity of microorganisms present in the reservoir, which, over millions of years, have consumed the lighter, biodegradable components of the oil, typically components of the saturated hydrocarbon and light aromatic hydrocarbon fractions. This leads to oils that contain higher proportions of branched and cyclic saturated hydrocarbons, heavier aromatic hydrocarbons, and the more polar components of crude oils—the resin and asphaltene fractions. These heavy, biodegraded oils have physical and chemical properties that make them more difficult and costly to produce and refine. For example, heavy oils can have viscosities in the range of 1 million to 10 million centipoise and can contain as much as 5% or more sulfur by weight. By contrast, light oils typically have viscosities less than 10 centipoise at room temperature and sulfur content as low as 0.01% by weight (Carrales and Martin 1975).

Studies of heavy oil reservoirs have offered fundamental insights into the nature of the petroleum reservoir biosphere. First, gradients in oil composition often observed in biodegraded petroleum reservoirs containing heavy oil suggest that oil-degrading microorganisms are not homogeneously distributed throughout the reservoir, but are, in fact, focused at the base of the reservoir where oil-saturated rock meets underlying water-saturated rock—the oil–water transition zone (OWTZ; Head et al. 2003). This was subsequently confirmed by quantification of bacterial 16S rRNA genes through an OWTZ demonstrating that bacterial abundance in the transition zone was two to three orders of magnitude greater than in the overlying oil column (Bennett et al. 2013). Nevertheless, it is known that microorganisms can also be detected in oil (Bennett et al. 2013; Meckenstock et al. 2014; Wang et al. 2014) where they are present

at lower abundance than in the OWTZ (Bennett et al. 2013) and most likely are present in highly dispersed water droplets that are typically present in crude oils (Meckenstock et al. 2014).

Produced waters from petroleum reservoirs and other deep groundwater systems contain $10^3$ to $10^6$ microbial cells/ml (Pedersen 1993; Nilsen et al. 1996); however, there are almost no data on microbial abundance in sediments directly recovered from petroleum reservoirs. Bacterial 16S rRNA gene abundance data from a core spanning the OWTZ of a heavy oil reservoir at a depth of approximately 600 m indicated that bacterial abundances ranged from around $10^3$ (and lower) to $10^6$ per $cm^3$ sediment with greatest abundance in the OWTZ and the lowest abundance in the oil-saturated reservoir sediments (Bennett et al. 2013). Interestingly, the abundance at the OWTZ was consistent with the "global" relationship between cell numbers and depth seen in a large sampling of deep subsurface marine sediments (Parkes et al. 1994, 2014; Jørgensen and Marshall 2016). The abundance in the oil column was two to three orders of magnitude or more lower, suggesting that lack of access to a continuous water phase or the inhibitory effect of certain components of the oil might limit microbial abundance in the bulk volume of oil reservoirs.

The undisturbed, in situ petroleum reservoir biosphere is deep and slow. It has been estimated that it can take millions to tens of millions of years to biodegrade the oil in a petroleum reservoir (Larter et al. 2003), and this equates to very low levels of microbial activity. On the basis of oil compositional gradients and other independent approaches, first-order rate constants for oil biodegradation at an OWTZ have been estimated to be on the order of $10^{-6}$ to $10^{-7}$ $yr^{-1}$. This is on the same order as the estimated reactivity of deeply buried sedimentary carbon that may also fuel the deep biosphere in general (Middelburg 1989; Middelburg et al. 1993; Jørgensen and Marshall 2016). Thus, in terms of broad characteristics, the petroleum reservoir deep biosphere is similar to other deep sedimentary environments, which, excluding situations where plate tectonics drive fluid circulation and mass transport, is an environment where activity is controlled by slow transport of solutes by diffusion (Jørgensen and Marshall 2016). This results in low cellular activity and low doubling times (typically on the order of hundreds to thousands of years; Jørgensen and Marshall 2016).

## WAKING THE (ALMOST) DEAD

Like the majority of the deep biosphere, microbial activity in the petroleum reservoir biosphere is likely limited by low energy availability engendered by limited quantities and transport of labile organic carbon, nutrients, and electron acceptors. Regions in the deep biosphere where advection of fluids increases mass transport of limiting resource are characterized by increased cell abundance and activity (Parkes et al. 2005). This clearly illustrates the fact that undisturbed deep subsurface sediments are mass transport limited, and resident microbiota have the potential to be reawakened given favorable environmental conditions. Moreover, it is clear from the work of Parkes et al. (2005) that an increase in solute mass transport can be sufficient

to revive the dormant cells of the deep biosphere. For a more complete appraisal and definition of dormancy in relation to the deep biosphere, the reader is directed to Jørgenesen and Marshall (2016).

A corollary of this observation is that any anthropogenic activity that alters fluid flow in the deep subsurface will have the likely consequence of stimulating the activity of the previously dormant indigenous microbiota. In addition, the stimulation of the native microbiota purely as a result of increased mass transport will be augmented by the delivery of exogenous organisms, electron donors, electron acceptors, and nutrients. Potential electron donors and carbon sources are plentiful in petroleum reservoirs, and under certain circumstances, electron acceptors can also be nonlimiting (e.g., sulfate from injected seawater). The sources of inorganic macronutrients required to wake the dormant petroleum reservoir microbiota are less well under- stood. Ammonium concentrations of up to 15 mM have been reported from some deep (ca. 300 mbsf) sub-seafloor sediments (Morono et al. 2011), and even higher ammonium concentrations (up to 71 mM) have been detected in a limited number of deep groundwater samples from petroleum reservoirs (Manning and Hutcheon 2004). Crude oil itself contains nitrogen (ca. 0.1% to 0.9% by weight; Ball et al. 1951). Much of this is organic nitrogen contained in the macromolecular fractions of the oil (Richter et al. 1952) and may thus be poorly available to micororganisms. The more soluble forms of organic nitrogen, mainly in the form of carbazoles, pyrolles, pyridines, and quinolones, are a potential source of nitrogen for microorganisms present, and alkylcarbazoles in particular have been shown to be degraded during heavy oil formation (Oldenburg et al. 2006).

Phosphorus in petroleum reservoirs is most likely present in mineral form, such as apatite inclusions in feldspars (Head et al. 2003), and it is known that in near-surface aquifers microorganisms preferentially colonize such mineral phases (Rogers et al. 1998). Whether this is also the case in petroleum reservoirs is not known, but again, utilization of a solid phase phosphorus source indicates that mass transfer of inorganic nutrients may have an important role to play in waking the petroleum reservoir biosphere.

Other factors that may contribute to waking the (almost) dead resident microbiota include temperature and salinity. The formation water from oil reservoirs can range from almost freshwater to near salt saturation (Ollivier and Cayol 2005), and the most halophilic hydrogenotrophic methanogen cultivated to date, *Methanocalculus halotolerans*, was isolated from a petroleum reservoir (Ollivier et al. 1998). It is apparent that there is an interaction between temperature and salinity, and halophilic thermophiles have not been found in petroleum reservoirs (Adkins et al. 1992; Bernard et al. 1992). This prompted Jeanthon et al. (2005) to suggest that high temperature and salinity together may limit microbial activity in petroleum reservoirs. This has subsequently been formalized in the palaeopickling hypothesis that attempts to explain the occurrence on nonbiodegraded oils in low-temperature saline reservoirs (Head et al. 2014).

While in situ, salinity and temperature may limit microbial activity; both may be altered considerably during oil production through practices such as seawater injection. Generally, this will lower temperatures, and depending on the formation water salinity, salinity may be increased or decreased by seawater injection. Alteration of temperature and salinity can have profound effects on microbial

activity, and this is likely to be most apparent close to the well bore subject to seawater injection. This has led to the concept of a thermal viability shell (TVS) that is incorporated into some reservoir souring models (Eden et al. 1993). The TVS refers to the region sur- rounding an injector well where the temperature is reduced and provides a gradient

of conditions extending from the well bore where both thermophilic and mesophilic organisms may thrive. This can have important consequences for souring and corrosion and their control in high-temperature reservoirs where a reduction in temperature can lead to a microbiologically active zone in the reservoir that was hitherto limited by high temperatures. Reductions in salinity close to the well bore of high- salinity reservoirs could likewise promote a "halo viability shell," promoting the activity of dormant indigenous organisms or permitting organisms introduced with injected fluids to thrive. This effect has been observed in practice where injection of low-salinity water in a Michigan oilfield precipitated reservoir souring, which was attributed to stimulation of sulfate-reducing microorganisms previously held in check by high-salinity conditions (Tinker et al. 1983).

Temperature changes are also inherent in the production infrastructure of an oil-field. Decrease in temperature of produced fluids as they are transported from a high-temperature reservoir to lower temperature above ground infrastructure, such as pipes and oil separators, again can result in stimulation of microbial activity, which may contribute to corrosion or hydrogen sulfide generation but may also contribute to other microbiologically influenced phenomena, such as biofouling (Sanders and Sturman 2005).

It is inevitable that the exploitation of deep geological resources will lead to changes in microbial ecology and activity, which may result in the modulation of beneficial and/ or detrimental microbial processes. Our intrusion into the subsurface will therefore always wake the deep, dormant biosphere. Thus, an understanding of the factors that control the deep biosphere is not simply a matter of academic curiosity. Indeed, it is, as those working in the business of resource extraction from the Earth know, a matter of significant practical import. The remainder of this treatise summarizes some of the consequences of waking the deep biosphere with respect to souring and corrosion (the central focus of this volume), microbially enhanced oil recovery, and challenges for emerging areas in geoenergy recovery. This sets the stage for more comprehensive treatment of specific issues provided in the following chapters.

## SOURING AND CORROSION AND THEIR CONTROL

A significant, though not the sole, cause of reservoir souring is the stimulation of microbial sulfate reduction (Gieg et al. 2011), which may be exacerbated by injection of sulfate-rich seawater for secondary oil recovery. It is not entirely understood whether the main culprits in reservoir souring are indigenous sulfate-reducing microorganisms (SRM) stimulated by free access to an electron acceptor that was previously limiting or if SRM introduced with the seawater also contribute. Nevertheless, it is clear that many sulfate-reducing taxa have been exclusively isolated from petroleum reservoirs and are likely to be indigenous (Birkeland 2005).

Irrespective of whether the SRM responsible are indigenous or introduced, the hydrogen sulfide produced represents a serious health and safety issue on production platforms as well as reducing the value of the produced oil and contributing to corrosion of the reservoir infrastructure.

Sulfate reduction is thought to be driven by organic compounds in the crude oil, such as organic acids (e.g., acetate, propionate, butyrate), which can be found at levels as high as 20 mM in oilfield waters (Birkeland 2005). It is also possible that crude oil hydrocarbons could act as an electron donor in some circumstances (Hubert et al. 2010; Agrawal et al. 2012; Khelifi et al. 2014). In addition to increasing accessibility to sulfate, the increased fluid movement induced both during primary production and due to water injection for secondary recovery will also increase the mass transport of electron donors as well as providing the sulfate necessary for hydrogen sulfide generation. The fact that secondary oil recovery that does not use injection of high-sulfate seawater (e.g., during produced water reinjection; PWRI) can also result in souring suggests that increasing mass transport alone can be sufficient to stimulate sulfide production (Vance and Thrasher 2005; Bjoernestad et al. 2006; Lysnes et al. 2009) and/or that organisms capable of generating sulfide using substrates other than sulfate (e.g., elemental sulfur-reducing *Thermococcus* and *Thermotoga* spp., or a range of oilfield organisms capable of thiosulfate reduction, e.g., *Thermotoga* spp., *Halanaerobium congolense*, and *Dethiosulfovibrio peptidovorans*) may have a role to play in souring under some circumstances (Ollivier and Cayol 2005).

Corrosion in all its forms has been estimated to cost the oil and gas industry around $1.4 billion annually in the United States alone (Koch et al. 2002). Microbially influenced corrosion (MIC) is a significant contributor to corrosion in the oil and gas industry (Little et al. 2007). Microbially produced sulfide contributes to MIC, but a range of microbial processes coupled with chemical and electrochemical reactions are involved in the process, which is far from fully understood. Sulfate-reducing bacteria have also been implicated in MIC through what has been termed "cathodic depolarization." This involves the microbial consumption of hydrogen produced electrochemically by reduction of protons with electrons derived from iron oxidation (Hamilton 1985; Larsen et al. 2010). The validity of cathodic depolarization as a key mechanism for MIC has been called into question (Hamilton 1985; Crolet 2005), and in many cases, it seems that prolonged generation of $H_2S$ by SRB and its reaction with metallic iron may be a more significant process in MIC (Enning and Garrelfs 2014). Direct oxidation of metallic iron as an electron donor (known as electrical microbially influenced corrosion or EMIC) for some sulfate-reducing microorganisms has also been shown to be a potentially significant in MIC (Enning and Garrelfs 2014). This process, which has been termed electrical microbially influenced corrosion (EMIC), can result in corrosion rates as high as 0.9 mm/yr, more than sufficient to lead to oilfield equipment failures. Nevertheless, it is likely that multiple processes contribute to corrosion under field conditions and that different mechanisms may dominate in different situations (Angell 1999).

Biocide treatment is often applied to control and reduce souring and MIC. However, these processes are often associated with biofilms, and biocides are generally less effective in biofilms. Treatment with nitrate has therefore been proposed as an alternative control mechanism for souring and corrosion. The precise mechanism of

nitrate control of sulfide production may be different under different circumstances. Nitrate treatment may stimulate heterotrophic bacteria that can outcompete sulfate reducers for electron donors. Nitrite generated by nitrate-reducing microorganisms can also be toxic to sulfate reducers and suppress sulfide production, or sulfide-oxidizing nitrate reducers that use sulfide as an electron donor can remove sulfide produced by the sulfate reducers and may also generate toxic nitrite (Hubert 2010). The end product of nitrate reduction may also be different, depending on the organisms present. Most dissimilatory nitrate reducers produce nitrite as an end product (Zumft 1992); however, in many different organisms, the nitrite generated is simply an intermediate, which is further reduced to ammonia, or through nitric oxide with nitrous oxide or dinitrogen gas as end products (Zumft 1992).

Nitrate treatment to control sulfide in petroleum reservoirs is not without its problems, and nitrite and possibly other chemical species generated as a product of nitrate treatment may actually exacerbate corrosion (Beeder et al. 2007; Vik et al. 2007).

Oilfield waters also contain considerable amounts of organic acids (Barth 1991). A number of mechanisms may lead to the generation and presence of compounds such as volatile fatty acids, including acetate, butyrate, and propionate. Thermal maturation of organic matter, either in the source rock from which the oil was derived or thermal alteration of organic matter in the reservoir itself, may explain this (Means and Hubbard 1987). However, fermentation of alkanes or other oil components may also lead to the generation of organic acids, and indeed it is known that during in-reservoir oil biodegradation over geological time scales, many organic acids are generated (Huang and Larter 2005). These include naphthenic acids and other acids structurally more complex than the volatile fatty acids produced by fermentation and generally considered by microbiologists (Huang and Larter 2005). This heterogenous mix of organic acids contributes to the total acid number (TAN) of crude oils, and high-TAN oils are known to lead to problems with corrosion, especially during downstream refining (Kapusta et al. 2004). Despite their significance for corrosion and souring prediction, factors controlling the concentrations of organic acids in petroleum reservoir fluids remain poorly understood, and this is an area worthy of future exploration.

## MICROBIALLY ENHANCED OIL RECOVERY

Waking the petroleum reservoir biosphere can clearly have detrimental consequences by promoting souring and corrosion; however, enhancing mass transport in petroleum reservoirs also has the potential to promote beneficial microbial processes in petroleum reservoirs. Stimulating resident microbial communities (Belyaev and Ivanov 1990; Ivanov et al. 1993) or the addition of exogenous microorganisms (Wang et al. 1993) with a view to enhancing oil production has the potential to use enhanced mass transport to great advantage. While microbially enhanced oil recovery (MEOR) is conceptually attractive, it has a somewhat checkered history and is often viewed with skepticism in the industry. This skepticism stems, in part, from a limited fundamental understanding of the microbiological processes that might lead to enhanced oil recovery, concerns about formation damage, and the difficulty of attributing changes in oil production to a

specific intervention on a field scale.

The concept of MEOR can be traced back to 1926 (Lazar et al. 2007), but MEOR was tackled seriously for the first time through the pioneering work of Claude Zobell in 1947 (Zobell 1947), and many of the principle drivers of MEOR were already recognized at that time. The very purpose of MEOR and enhanced oil recovery (EOR) in general is to increase mass transfer, and it is therefore not surprising that implementation of MEOR stimulates the activity of indigenous organisms, which then leads to further improvements in mass transfer. This can occur through modification of porosity and permeability (e.g., by alteration of mineral phases in a reservoir, selective plugging of high permeability "thief zones" with biomass or microbially produced polymers), alteration of wettability and interfacial forces (by production of biosurfactants), or modification of oil viscosity and/or reservoir pressure through gas or solvent production (Lazar et al. 2007). Modification of the oil composition through selective biodegradation of particular components of crude oil may also improve mass transfer and fluid flow (He et al. 2000). It has also been suggested that stimulating the conversion of residual oil to methane in situ could be a means of enhancing the recovery of otherwise stranded oil (Parkes 1999; Gieg et al. 2008; Jones et al. 2008). This could enhance oil recovery by generating more gas in situ, which would initially dissolve in the oil, reducing its viscosity. When the gas solubility is exceeded, the free gas generated would repressurize the reservoir, improving oil recovery, and finally, if sufficient gas is generated, the gas itself could be recovered as an energy source (Head et al. 2014).

Given the range of processes that may be involved in MEOR, it is perhaps not surprising that it is difficult to reliably evaluate the efficacy of any particular MEOR intervention. Moreover, as noted previously, enhancing mass transfer in a formerly diffusion-driven system has the potential to promote not only beneficial process, but also detrimental processes. A side effect of MEOR treatments can therefore be reservoir souring and increased MIC (Lazar et al. 2007).

## NEW FRONTIERS FOR OIL AND GAS MICROBIAL ECOLOGY

Foremost among new frontiers for geoenergy recovery is the use of hydraulic fracturing (fracking) to recover shale gas. The fact that very low permeability shales retain vast amounts of gas, primarily methane, is testament to the extremely slow mass trans- port in these systems, and indeed the fundamental basis of fracking is to increase mass transfer of gases trapped in micropores within the shale. The very low levels of mass transport and the extremely small pore sizes (nm scale) in shales (Al Hinaia et al. 2014) make shales inhospitable for microbial life. Nevertheless, microorganisms can inhabit larger pores and the fracture system in intact shales, and so shales are likely not completely devoid of life though microbial abundance is likely to be very low. Since fracking dramatically increases mass transport in shales, it seems likely that there will be equally dramatic alterations in the microbial communities in response. Microbial studies of shales are currently sparse (Mouser et al. 2012; Cluff et al. 2014; Jimenez and Krüger 2014) though the organisms detected fit with the characteristics of the system, being dominated by halophiles presumably from the saline aquifers associated

with the shales (Cluff et al. 2014).

Given that increasing mass transport will stimulate the shale-associated deep biosphere, there is considerable potential for microbially mediated problems, such as MIC or souring, to arise in shale gas production facilities. Conversely, managing shale-associated microbial communities could be used beneficially to alter formation porosity and permeability, for example, by transformation of organic matter in the shale and/or alteration of the mineralogy of the formation.

Coal bed methane formation also has a microbiological dimension, and there are many uncertainties about the source of biogenic methane in biologically enhanced coal bed methane formation (Strapoc et al. 2011). The structure of coal also means that microbial conversion to methane may also be mass transfer limited. There is, however, evidence that microorganisms have the capacity to overcome this in novel ways. It has been shown that the phenazine dye, neutral red, at concentrations greater than its aqueous solubility forms conducting organic crystals (Beckmann et al. 2016). These crystals enhance methane production from coal and other materials, and a possible mechanism for this is the direct transfer of negative potential electrons to methanogens by direct electron transport from the coal matrix to the methanogens that can then use the electrons to reduce $CO_2$ to methane (Beckmann et al. 2016). The realization that direct intercellular electron transport may be a widespread feature of anaerobic ecosystems (Wang et al. 2016) opens the door to many exciting avenues of research and potential applications in low mass transport environments.

# Chapter 4

## Digital Petrophysics: Imaging, Modeling, and Experimental Challenges Related to Porous

Peter Tilke

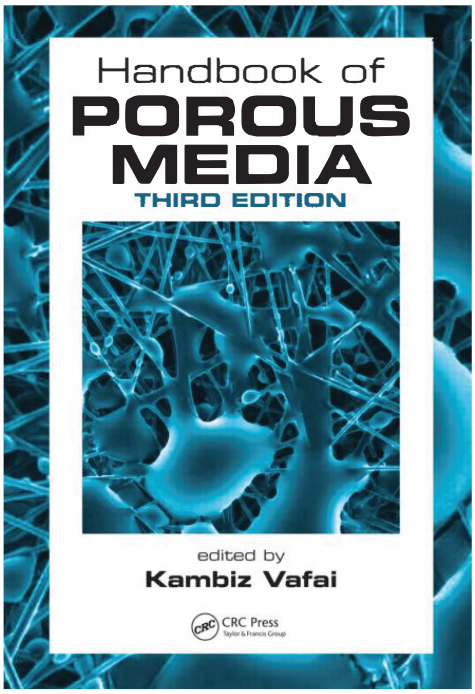


**Handbook of Porous Media, Third Edition**

*By* Tambiz Vafai

# Introduction

The complex interaction of liquids, gases, and solids at the pore scale is of interest in many areas of geoscience including oil and gas production, enhanced oil recovery, hydraulic fracturing, analysis of shale oil and shale gas, and carbon sequestration. This chapter presents the background and an overview of the rapidly evolving field of digital petrophysics: the imaging and modeling of porous media in the oil field along with experimental issues related to their understanding.

Modeling multiphase fluid flow at the pore scale gives us much insight into the physics at nanometer and micrometer scales. However, when interpreting and modeling porous media in the oil field, one must consider the wide spectrum of scales that must be addressed and the challenges in reconciling the physics and geology at these different scales.

An overview of the digital imaging workflow with an emphasis on x-ray computed tomography (CT) is presented. This is followed by a discussion of the various elements of the digital petrophysics workflow that includes imaging, image processing, and the modeling of transport properties. A review of experimental approaches to imaging dynamic multiphase interactions at the microscopic level during drainage and imbibition follows.

Finally, some of the challenges involved in relating studies conducted at the pore scale to the phenomena observed at the macroscopic reservoir scale are addressed.

## Porosity and Permeability in the oil field

The term oil field can refer to either a geographic area where oil is produced or to the subsurface accumulation of oil trapped in reservoir rock. The latter definition is the one used in this chapter. Oil fields are composed of sedimentary rock composed of mineral grains and interconnected pores. This aspect of porous rock can easily be seen in a geologic precursor such as beach sand; a hole in beach sand rapidly fills with water. When porous sediment such as beach sand is buried and trans- formed into rock (diagenesis), the connate water in the pores can remain, migrate away, migrate in, or be chemically incorporated into the cement-forming minerals. Many types of sediment contain abundant organic material that, during the diagenetic process caused by increasing temperature and pressure, transform to kerogen and, ultimately, to oil and gas.

The sedimentary rocks in an oil field are generally either clastic or carbonates. Clastic sediments are deposited by wind (e.g., sand dunes), rivers (e.g., point bars and deltas), marine reworking (e.g., beaches), and deep-sea currents (turbidites). The minerals comprising these clastic rocks can represent the weathered remains of ancient mountain ranges and include quartz, feldspar, and clay minerals. Carbonates, on the other hand, are of biological origin and can represent deposition ranging from buildups by living organisms, for example, coral reefs to the gradual accumulation of biogenic calcite. When these sediments are buried and compacted, diagenetic processes cement the grains together forming rock.

During diagenesis, dissolution of original minerals may increase the pore space or precipitation of minerals may decrease the pore space. As a result, the rock is now a

complex network of pores connected with pore throats in which the mineral composition of the pores and pore throats can be quite variable.

Whereas porosity represents the capacity of reservoir rocks to store oil, permeability represents the ability of fluids to flow through these rocks. The most direct measurement of permeability is absolute permeability, measured in darcies or millidarcies, which is an intrinsic property of the rock. Relative permeability, on the other hand, results from the complex interaction of multiple immiscible fluid phases in the pore network. It is a dimensionless term that describes the flow of a fluid in the presence of other fluids. Relative permeability is influenced by fluid compositions, relative saturations, wettability, and capillary pressure, which must all be considered when trying to understand the fluid flow in reservoir rocks.

In conventional oil fields, the oil formed in the organic-rich source rock migrates to relatively high-porosity reservoir rock. In the reservoir rock, the oil may be trapped in structural or strati- graphic traps. As oil migrates into the reservoir rock, it displaces some of the original water. Because of the complex wettability and relative permeability relationships, some fraction of the connate water generally remains.

In shale oil fields, the oil is being produced directly from the source rock. In these rocks, the matrix permeability is extremely low, typically in the nanodarcy range. To produce oil from these rocks, fluid must be injected at high pressure from a borehole into the formation to induce fractures or open existing natural fractures. Thus, understanding the interplay of fluid flow between the low-permeability matrix and fracture network is crucial.

The properties of porous rock in the oil field must be considered at scales spanning many orders of magnitude. At the smallest scale, pore throats connecting the pores, which store fluid, will influence the permeability. In shale formations and tight reservoirs, these pore throats can be 10–100 nm in diameter, while in conventional reservoirs, they may be micrometer sized. The interplay of water and oil wettability may be influenced by the mineralogy of rock at the nanometer scale. At the centimeter and meter scales, fine-scale heterogeneities in the rock layering come into play and will affect fluid flow in the vertical direction and are often modeled as a series network. At still larger scales, on the order of tens of meters, lateral heterogeneities are important. A high-porosity river channel deposit may give way laterally to a very low-porosity floodplain deposit. At still larger scales of hundreds of meters to kilometers, heterogeneity due to faults, fracture networks, and folds dictate variation in porous properties. It is clear that all these scales must be considered when an oil field is being developed.

Measuring the static and dynamic properties in situ is the most direct measurement of rock and fluid properties. To do this, a well must be drilled, and logging measurements—measurement of the rock's response to electric, electromagnetic, sonic, and other signals by specialized tools lowered into the hole—are made to infer the mineralogy of the rock, the porosity, and fluid com- position. New technologies now allow fluids to be sampled downhole, which gives insight into the current fluid composition. However, to measure the properties under a variety of fluid compositions, a sample of the rock must be obtained, either full-diameter cylinders (cores) of the formation being drilled or as smaller sidewall cores taken from the formation surrounding the borehole and the measurements made in the laboratory. The difficulty with this approach is that while the measurement may be relevant to the sample, the observed heterogeneity in rock properties and fluid composition as already discussed makes it difficult to extrapolate the results to the entire reservoir. For this reason, it is necessary to complement these small-scale measurements with larger-scale and lower-

resolution measurements using technologies such as reflection seismology. Seismic data are a measurement of acoustic properties in which the measurement size or voxel is at the scale of tens of meters. Modeling of seismic attributes can yield very accurate insights into the rock and fluid properties, albeit at a coarse scale relative to the in situ measurements.

When a core sample is obtained from a well, a standard suite of measurements is generally made in the laboratory. This conventional core analysis includes a description of the lithology and measurements of porosity, grain density, fluid saturations, and absolute permeability parallel to bedding. The lithological description is done on the whole, full-diameter core while the other measurements are done on smaller plugs taken from the whole core. The measurements are performed either at standard temperature and pressure (STP), or at reservoir conditions, or both.

Special core analysis (SCAL) is performed when more complex reservoir engineering properties are required. This includes relative permeability, capillary pressure, and wettability under a variety of combinations of two-phase or even three-phase conditions.

Because of the cost, time, and uncertainty in these core analysis measurements, there has recently been great interest in computational approaches. These techniques involve imaging a microscopic sample of the rock using techniques such as confocal microscopy, x-ray CT, scanning electron microscopy (SEM), or focused ion beam (FIB) tomography. These three-dimensional (3D) images are then analyzed to generate models of the mineral, grain, and pore network. Using these geometric models with physical properties, many of the traditional laboratory measurements can now be modeled.

As noted earlier, the microscopic physical properties obtained from the core plug will not necessarily agree with the macroscopic properties and behavior at the reservoir scale. Therefore, it is standard practice to complement core plug measurements with the interpretation of reservoir properties from observed well performance (i.e., its production history). Over the life of a well, the fluid production rate and/or bottom-hole pressure will decline as the reservoir is depleted. These changes in the well performance are interpreted using decline and rate transient analysis techniques to infer the macroscopic reservoir properties.

If many wells have been producing in a reservoir over an extended period, then the model-based interpretation of the well performance is interpreted using a reservoir simulator. This exercise is termed history matching and involves refinement of the reservoir model so that an optimal match is found between the observed historical behavior of the wells and the model of the structure of the reservoir and the distribution of different rock types.

Related to the question of scale and history matching is the reconciliation of the microscopic and macroscopic measurements, physics, and geology. That is, how laboratory measurements made on millimeter-sized core samples relate to the performance over 30 years of hundreds of wells in an oil field. Interpretations and inferences made at one scale must be consistent with the other scale.

## Digital Rocks and their Interpretation

Understanding the physics underlying the interaction between fluids, pores, and rock matrix is crucial to explaining the experimental observations and measurements made at the laboratory and field scales. Only by developing good explanations can we make reliable forecasts of the behavior (Deutsch, 2012).

The macroscopic transport properties of porous rocks are the aggregate or emergent properties of phenomena occurring at the pore scale. Therefore, models of the 3D microstructure resulting from the mineral grains and pore network must be constructed to derive the macroscopic properties. Katz and Thompson (1986) presented an early effort to develop a relationship between pore- network geometry and macroscopic transport properties such as electrical conductivity. Their work suggested a characteristic length for percolation in porous media. With improving computational tools during the late 1980s, many workers began investigating the idea of generating digital or synthetic microstructural rock models to better understand the emergent behavior of fine-scale rock–fluid interactions at the larger rock or even reservoir scale.

**Reconstruction**

In recognition of the need for good microstructural models, there has been much interest in reconstructing 3D microstructural models from lower-dimension (2D) data. Adler et al. (1992) worked with 2D thin section images of Fontainebleau sandstone. The 2D image was binarized and statistically modeled to obtain the porosity and the spatial autocorrelation of the grain and pore space. Assuming spatial isotropy and ergodicity, the sample was then statistically reconstructed in 3D.

Yeong and Torquato (1998) developed a more general approach to reconstructing porous media and also illustrated the procedure with a Fontainebleau sandstone example. They showed that it is necessary to invoke a hybrid model for the morphology, which incorporates the two-point autocorrelation and a lineal path function.

Hazlett (1997), working on Berea sandstone, compared different approaches to reconstruct a 3D model of the pore network. In addition to statistical and visual comparisons of the reconstructions, lattice Boltzmann (Chen and Doolen, 1998) simulations of the permeability performed a further validation. It was found that the purely geometry-based reconstructions were insufficient to model the measured permeability. However, if the image-based reconstructions were supplemented with pore connectivity information obtained from capillary pressure drainage experiments, satisfactory results could be achieved.

This work is further developed by Manwart et al. (2000), who also extend the work of Yeong and Torquato (1998) by considering two-point statistics, lineal path, and pore size distribution. Further refinements to the simulated annealing approach introduced by Yeong and Torquato (1998) are found. In applying this approach to the reconstruction of Berea and Fontainebleau sandstones, it is recognized in agreement with the findings of Hazlett (1997) that the image-derived proper- ties are insufficient to reproduce the transport properties. The authors suggest incorporating local porosity theory (Hilfer, 1992) to refine the reconstruction by modeling variations in morphological properties such as porosity, specific surface, and connectivity.

Bakke and Øren (1997) developed a process-based reconstruction approach in which sandstone is reconstructed by simulating the processes of deposition, compaction, and diagenesis. Øren and Bakke (2003) further developed this approach by interpreting 2D thin sections of Berea sandstone to identify porosity, grain-size distributions, and mineral phases. The 3D model is then constructed by depositing spherical and ellipsoidal grains honoring the observed grain-size and phase distributions. The rock is then compacted and diagenetically altered. Subsequent modeling of the transport properties using this reconstruction approached yielded results consistent with experiment.

Using multipoint geo-statistics, Strebelle and Journel (2001) allow a training image to be defined, which gives a much richer description of the spatial statistics than that can be obtained with two-point and lineal techniques. Okabe and Blunt (2004) applied this approach to reconstruct Berea sandstone and obtained good results when simulating permeability.

## CT imaging

Withjack (1988) introduced CT imaging of porous rock with an emphasis on evaluating potential core damage and characterizing the distribution of fluids during flooding experiments. This early work involved imaging at the millimeter scale. Although there is a trade-off between resolution and sample size, scanner technology has advanced such that, for example, Vega et al. (2013a) report 20 nm resolution images of small 60 µm samples. A typical resolution for conventional porous rock is 3.52 µm voxels with sample dimensions 1024 × 1024 × 1484 (Sheng et al., 2011). Imaging volume has also increased with some vendors reporting 20 µm resolution for a 1.5″ core plug.
Figure 1 is an example of the high-quality imagery now available illustrated by a carbonate with image voxel size of 2 µm, while Figure 2 is a shale sample imaged at a voxel size of 500 nm.

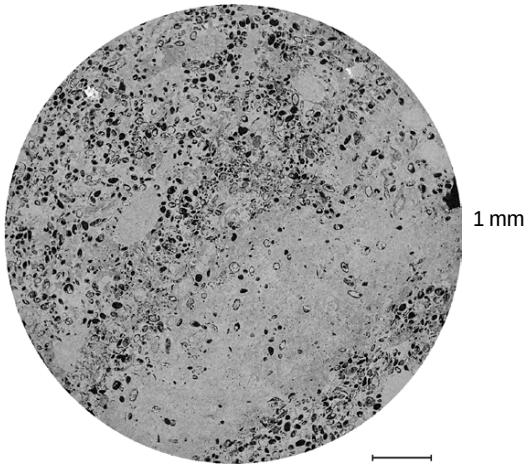


**Figure 1** Grayscale 2D micro-CT cross section of carbonate (voxel size is 2 µm) acquired from 8 mm cylindrical core mini-plug. (Image copyright Schlumberger Technology Corporation, Sugar Land, TX. Used with permission.)

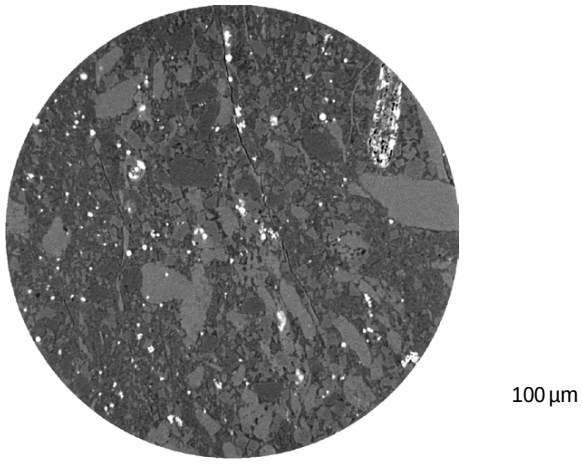


**Figure 2** Grayscale 2D micro-CT cross section of shale (voxel size is 500 nm—resolution) acquired from 8 mm cylindrical core mini-plug. (Image copyright Schlumberger Technology Corporation, Sugar Land, TX. Used with permission.)

CT imaging of the pore structure is possible because the CT number of mineral grains is sufficiently high, where CT number in Hounsfield units (HU) is defined as

$$HU = \frac{\mu_X - \mu_{water}}{\mu_{water}}$$

$\mu_X$ is the average linear attenuation coefficient of the voxel
$\mu_{water}$ is the linear attenuation coefficient of water

Akin et al. (2000) list some typical CT numbers.

It is now possible to *zoom in* on a sample so that a high-resolution image can be obtained from a large sample without physically cutting the sample. Figure 1 illustrates a 5 µm resolution image of sandstone obtained from a 1.5-in. cylindrical core mini-plug using this capability (Figure 3). Not only has the resolution of CT instruments improved, but the experimental techniques and workflows have advanced so that mineral phases can be distinguished and even fluid types. For example, Zacher et al. (2010) studied numerous limestone samples at 500 nm with impressive resolution of fossiliferous pore structures. Vega et al. (2013a) studied gas shale samples from the Eagle Ford, Barnett, and Fayetteville fields. Using a relatively low-resolution CT of 200 µm, they were able to study relatively large samples of 2.5 cm diameter. By injecting high-contrast xenon and krypton gas into the sample, the authors imaged the porosity and fracture distributions.

Although CT is proving to be excellent at resolving different mineral phases, it does not provide insight into the chemistry of these phases. Boone et al. (2010) present a workflow for combining CT imagery with x-ray fluorescence elemental maps.

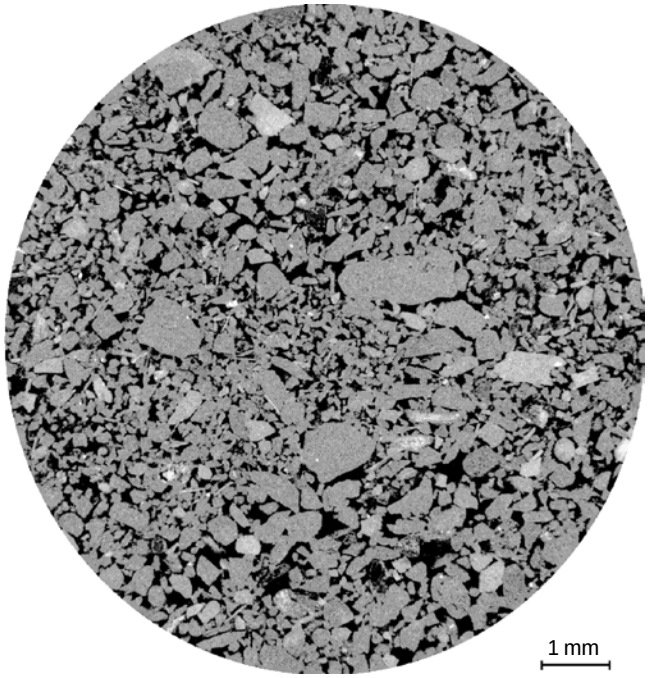


**Figure 3** Grayscale 2D micro-CT cross section of sandstone (voxel size is 5 µm) acquired from 1.5 in. cylindrical core mini-plug using zoom-in option for scanning entire rock volume without physically cutting the sample. (Image copyright Schlumberger Technology Corporation, Sugar Land, TX. Used with permission.)

## FiB-SEM imaging

FIB tomography allows 3D images to be constructed at the resolution of several nm to yield insight into the microporous structures of carbonates and shales. In this approach, the SEM images the sample surface, while an FIB etches away a fresh surface after each scan. Stacking sequential 2D SEM images thus composes the 3D image.

## Dynamic Imaging

Many questions in understanding transport properties involve time. Darcy's law for single-phase fluid flow relates fluid flux to absolute permeability:

$$u = -\frac{k}{\mu}\frac{\partial p}{\partial x}$$

where

$u$ is the velocity of the fluid
$k$ is the absolute permeability
μ is the viscosity of the fluid
$\partial p/\partial x$ is the pressure gradient of the fluid

Multiphase fluid flow involves relative permeability of the interacting phases. Displacement of a non-wetting phase by an immiscible wetting phase is termed imbibition. Complex flow geometry

and wettability cause hysteresis in both capillary pressure and relative permeability. The concept of relative permeability allows Darcy's law to be extended to multiple phases:

where

$u_w$ is the velocity of the wetting phase
$k$ is the absolute permeability
$k_{rw}$ is the relative permeability of the wetting phase
$\mu_w$ is the viscosity of the wetting phase
$\partial p_w/\partial x$ is the pressure gradient of the wetting phase

A variety of laboratory methods exist to measure relative permeability (e.g., Dandekar, 2013) However, novel application of CT imaging has provided a new approach to measuring relative permeability. For example, Akin et al. (2000) and Schembre and Kovscek (2003) present imbibition experiments in which diatomite cores are dried and placed in a water jacket, and a CT image of the dry sample is acquired. Water is then injected from the side of the core sample, and a series of time-lapse CT images is acquired. Water and air have different CT numbers as shown in Akin et al. (2000). Images at different time steps are subtracted from the reference (air only) image. The differences in CT number are transformed to saturation maps using (Akin et al., 2000)

where

$S_w$ is the saturation of the wetting phase
$CT_{dry}$ is the CT number of the dry phase
$CT_{wet}$ is the CT number of the wetting phase $CT_{obj}$ is the CT number of the object

At different time steps during the experiment, saturation profiles are obtained across the core samples (Figure 4 in Schembre and Kovscek, 2003). These experiments were also conducted on oil–water systems in diatomite and Berea sandstone. Schembre and Kovscek (2003) also develop the equations to interpret relative permeability from these experimental observations and obtain consistent results for both the diatomite and Berea sandstone.

Rangel-German and Kovscek (2002) applied a similar time-lapse CT approach to analyzing imbibition when an idealized fracture is present to compare the behavior of different fracture widths. They identified two different flow regimes when comparing flow in the fracture with respect to flow in matrix.

Lee and Karpyn (2010) studied Berea sandstone with a single tensile fracture. They explored different injection rates to understand fracture–matrix transfer mechanisms. This yielded a comprehensive set of data showing fluid recovery and saturation maps (Figures 5 and 6 in Lee and Karpyn, 2010). Alshehri and Kovscek (2012) studied waterflooding of fractured carbonate cores with and without surfactants using this dynamic CT imaging technique. The major flow pathways were successfully imaged in these experiments (Alshehri and Kovscek, 2012, Figure 11).

Dynamic CT imaging has given insight on directly imaging the major fluid flow pathways dur- ing imbibition. Pioneering work with dynamic high-resolution confocal microscopy is beginning to yield greater insights into the pore-scale spatial fluctuations of fluid flow through these porous media. Krummel et al. (2013) demonstrate that during imbibition, the wetting phase (water) pinches off threads of the non-wetting phase (oil) in the narrow crevices of the porous medium, forming disconnected, non-wetting phase ganglia. Some of these ganglia remain trapped within the medium. By fully imaging the fluid distributions in 3D, Krummel et al. (2013) are able to show that the typical ganglion size and the total amount of residual non-wetting (oil) decrease as the capillary number increases. This behavior reflects the competition between the viscous pressure in the wetting phase and the capillary pressure required to force the non-wetting phase through the pore network. Thus, the influence of pore-scale fluid dynamics on multiphase flow at a macroscopic scale is better understood.

## Modelling Digital Rocks

The advent of imaging techniques such as x-ray CT and confocal microscopy has enabled the rou- tine acquisition of 3D images of porous rock. To apply modeling techniques to these images, they must first be *segmented*. Image segmentation involves classifying the voxels to either grain or void (pore) space. Ideally, the grains may be further classified into their distinct mineral phases.

## Segmenting the Images

Image segmentation is widely studied in many fields ranging from character recognition to medical imaging to remote sensing. The challenge in any of the domains is to reduce the misclassification of pixels and voxels that occurs in naive thresholding approaches.

Thresholding can often be applied to classify grains and pores when the entire pixel/voxel is occupied by the phase. However, difficulty arises when the pixel/voxel is partially occupied.

Recognizing the unique characteristics of porous rocks, Oh and Lindquist (1999) extended the thresholding technique to incorporate spatial geostatistics. The authors evaluate the spatial covariance in the image and then use indicator kriging to identify grain edges even when pixels/voxels are partially filled.

To efficiently prepare a 3D image for modeling, it is insufficient to simply distinguish grain from pore. Lindquist et al. (2000) and Sok et al. (2002) recognized that other key geometric properties must be extracted from the image, including pore size distribution, throat size distribution, coordination number distribution, and pore channel length. When comparing Fontainebleau sandstone to stochastically generated rocks, Sok et al. (2002) found modeled transport properties to be different from the imaged rocks, even when the noted geometric properties were consistent. They found it necessary to introduce additional properties including pore–pore correlations and local pore–throat correlations.

Thompson et al. (2005) present a grain-based reconstruction algorithm, which, as with the process-based and multipoint geostatistics approaches, extracts a wide range of grain properties from a training image. These properties include grain size, aspect ratios, orientation, and surface area. Each individual grain is labeled (Thompson et al., 2005 Figure 4). The basis of the image is now the set of grains rather than voxels. This allows pores to be identified and their interconnections to be modeled more efficiently (Thompson et al., 2005, Figure 7).

Figure 4 is an example illustrating the workflow for CT image processing. Grayscale images from the micro-CT reconstruction pass through the binarization phase of segmentation, followed by rock structure analysis, which identifies individual grains and labels them with colors.

Images acquired with the FIB-SEM approach go through similar processing steps. Figure 5 illustrates an example of this workflow applied to shale. Here each phase (pore, organic, minerals with different electron densities) is classified. The result is each pixel in the image being classified to a particular phase.

As tomographic imaging is applied to more complex problems, the segmentation requirements have also increased. Of interest to many workers on porous media in the oil field is the ability to image multiple fluid phases in the pores: water, oil, and gas. Image contrast between these fluid phases is often difficult to resolve, and the signal peaks can have significant overlap. Bhattad et al. (2010) leveraged techniques from medical imaging, such as anisotropic diffusion, to complement the geostatistical indicator kriging approaches discussed earlier.

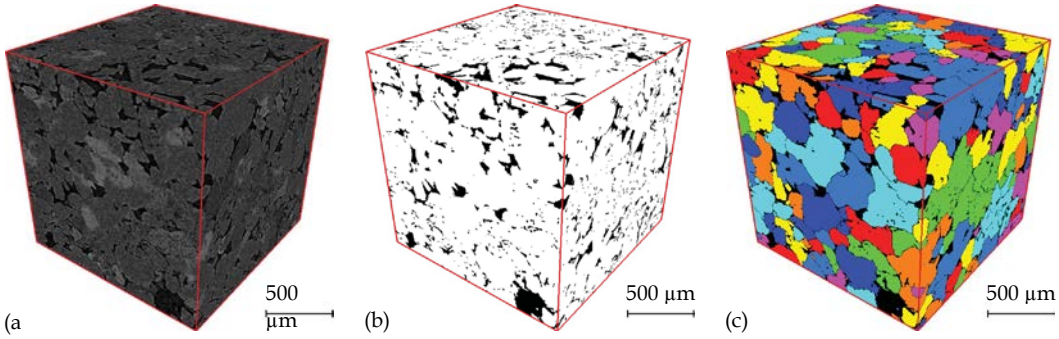


(a) (b) (c)

**Figure 4** X-ray micro-CT image processing and analysis workflow. (a) Visualization of 3D cubical stack of grayscale images (cropped from scanned volume, usually cylindrical). (b) Binarized 3D volume created with preserving grain/pore boundaries. (c) Visualization of well-separated grains in sandstone. (Images copyright Schlumberger Technology Corporation, Sugar Land, TX. Used with permission.)

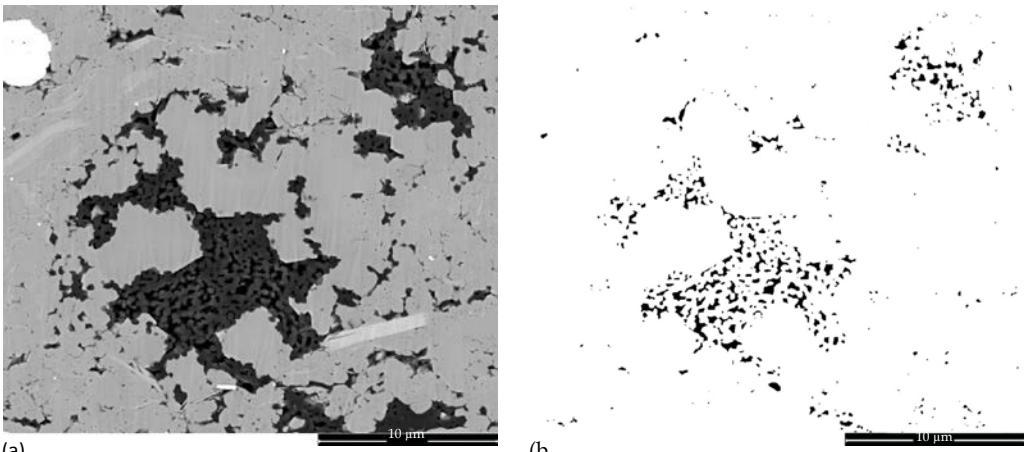


(a) (b)

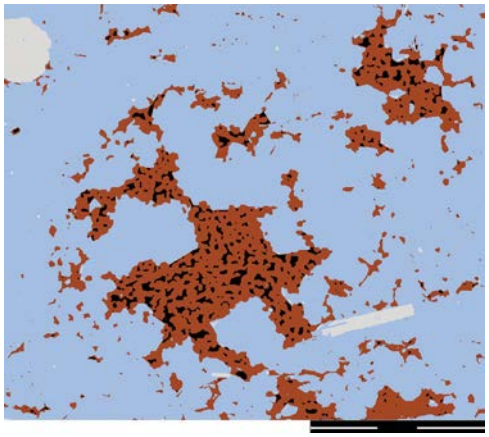

(c)

**Figure** SEM image processing and analysis workflow. (a) Two-dimensional grayscale image acquired via electron backscattering to achieve high contrast between minerals with different density. (b) Binary images are then generated for each phase of interest. (c) Binary images of each phase are then combined: pores (black), organic (orange), main minerals (blue), and dense minerals (white). (Images copyright Schlumberger Technology Corporation, Sugar Land, TX. Used with permission.)

Software packages now exist (e.g., Cnudde et al., 2010) to routinely segment tomographic images into different phases for the analysis of geometrical and material properties such as porosity, partial porosity, pore size distribution, grain size, grain orientation, and surface determination.

## Building the Model

Once the 3D image of the rock has been segmented into different mineral and fluid phases, a decision of how to model the volume for subsequent simulation must be made. The choice of model and simulation tool depends on a number of factors, including the physics being modeled, the scale of the problem, and the computational capabilities. Some of the model classes and simulation approaches are summarized later.

### lattice Boltzmann

The lattice Boltzmann simulation method is a simulation technique that solves a discretized Boltzmann equation (Gunstensen et al., 1991; Chen and Doolen, 1998). It can be shown that the macroscopic dynamics of this technique obeys the Navier–Stokes equation. The technique has been successfully applied to a variety of porous media problems (e.g., Ferreol and Rothman, 1995). The fluid is modeled as particles that move on a regular lattice.

Many investigators have found the lattice Boltzmann approach to give satisfactory solutions to the Navier–Stokes equation for transport properties such as absolute permeability (e.g., Manwart et al., 2002; Arns et al., 2004, 2005a, 2008; Okabe and Blunt, 2004; White et al., 2006) The general lattice Boltzmann method has also been extended to support immiscible multiphase fluids (Reis and Phillips, 2007). However, there are still significant limitations in the ability of lattice Boltzmann to model differences in the fluid properties such as viscosity of the different phases.

One major advantage of the lattice Boltzmann method is that a 3D lattice can be simulated directly, rather than implementing a simplified pore-network model. However, the disadvantage is the computationally large model that must be created for lattice Boltzmann. Despite increasing computing capacity, the largest models that can be accommodated with lattice Boltzmann are significantly smaller than what can be modeled with the compressed pore-network models.

### Finite Difference

The finite difference approach lends itself to simulating many properties of porous rock. Manwart et al. (2002) compared the finite difference and lattice Boltzmann methods to model absolute permeability. Haney et al. (2006) demonstrated finite difference for modeling the acoustic properties of porous media.

A key advantage of finite difference approaches is the wide range of available standard approaches. Another advantage of finite difference is that the voxels of CT images may be used directly as the finite difference cells without the need for the upscaling that must be done for pore-network modeling. On the other hand, the computational

resources limit the size of the modeled rock volume.

**Finite Element**

While the finite difference method is suitable for modeling many problems in porous media, it is often necessary and valuable to apply the finite element method to these problems. For example, Könnö (2011) uses the finite element method to model Brinkman flow in porous media, which balances Darcy and Stokes flow in a single model. Another important advantage of finite elements over finite difference is that complex models can be constructed. Figure 6 illustrates a finite element mesh model of porous rock at the pore and pore threat scale. Note the wide variation in the size and shape of the individual elements of the model. The fine elements in the pores allow accurate modeling of the multiphase and multicomponent fluids, while the fine elements on either side of the boundary between solid and liquid phases allow surface phenomena to be modeled.

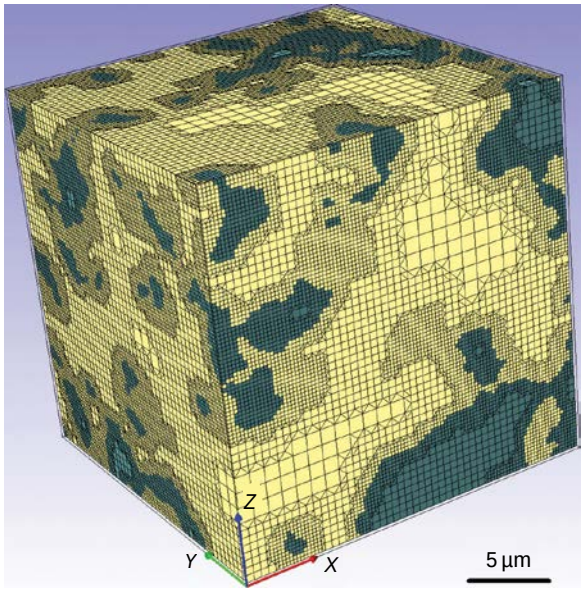


**Figure 6** Visualization of mesh rock model. This type of model can be used by commercial finite element multiphysics simulation software. (Image copyright Schlumberger Technology Corporation, Sugar Land, TX. Used with permission.)

When the porous medium is represented with such a mesh, the physical and chemical properties may be modeled using commercial multiphysics simulation software.

**Pore Network**

Representing the pore space as a graphical network is a powerful model for simulating transport properties. In this pore-network approach, vertices represent pores and the throats connecting pores are represented as edges (Piri and Blunt, 2005, Figure 2). This approach acquired momentum when Blunt (1997b) developed a pore-network model to study the effects of wettability by integrating the pore-level approach introduced by Kovscek et al. (1993).

In this approach, the throats represented by the edges of the graphical network can assume a variety of cross-sectional shapes (Piri and Blunt, 2005, Figure 5). Blunt (1997a) and Blunt (1998) were able to investigate pore-network models with a variety of initial oil saturations and differing contact angles. Modeling of relative permeability and

capillary pressure on the model gave insight into the behavior at the pore and throat levels.

Bakke and Øren (1997) and Øren et al. (1998) also demonstrated the value of building large pore- network models to predict a variety of transport properties in good agreement with experimental results on several sandstones. These workers were also able to model multiphase properties such as relative permeability.

Applications of pore-network modeling have become increasingly complex. Hui and Blunt (2000) investigated three-phase flow. An initially water-filled water-wet system is invaded by oil to represent initial oil migration. Water injection followed by gas injection results in many possible different combinations of wettability (Hui and Blunt, 2000, Figure 2). Hughes and Blunt (2000) studied imbibition with varying flow rate and contact angles. Using the pore-network model, they identified five generic types of displacement pattern. Knackstedt et al. (2001) and Arns et al. (2003) demonstrated that pore-network models are consistent with experimental results only if correlated heterogeneity is considered when modeling the pore geometry.

Despite ever-increasing computational power, there continues to be a need to make larger models of the microstructure. Pore-network models are ideally suited for this as they are a highly compressed representation of the microstructure. The models can now be made large enough to bridge the gap to the larger continuum representations. Sheng and Thompson (2013) take such an approach by embedding large pore networks into grid blocks of a reservoir model. In this approach, the network model can predict transport properties such as relative permeabilities, while the continuum reservoir simulator provides boundary conditions from time step to time step.

An obvious difficulty with the pore-network approach is that the true geometry of individual pores and pore throats is highly simplified. Further, it is difficult to determine a priori what complexities in the pore and throat geometry and properties must be modeled to properly replicate multiphase flow.

#### 22.4.2.5 Smooth Particle Hydrodynamics

Recently, Leonardi et al. (2011) demonstrated a porous media simulator using a 3D smooth particle hydrodynamics approach.

Smooth particle hydrodynamics is a mesh-free Lagrangian particle simulation method first developed for astrophysical problems by Gingold and Monaghan (1977) and Lucy (1977). It is now applied widely to fluid mechanics problems and continuum problems involving large deformation or brittle fracture (e.g., Liu and Liu, 2003; Onate and Owen, 2011) As with other particle methods, a key advantage of particle methods such as smooth particle hydrodynamics is the ability to advect mass with each particle. Thus, phase interfaces do not have to be explicitly tracked during the simulation. There is a computational expense for managing the free particles. However, in many circumstances, the versatility for solving multiphysics problems can be justified.

**Density Functional Hydrodynamics**

Density functional hydrodynamics (DFH) is an application of density functional theory (DFT) in the hydrodynamics of multiphase compositional mixtures (Dinariev, 1995, 1998). DFH is substantiated in both classical and quantum statistical mechanics (Dinariev, 2000). The central idea of DFT is the representation of energy of a heterogeneous system as a functional of densities of chemical components constituting this system. The first consistent results in DFT are related to the Thomas– Fermi model of electron gas developed in 1927. DFT is successfully applied in quantum chemistry, nuclear physics,

physics of semiconductors, superconductivity, and diamagnetics. DFH can be considered as a generalization of DFT. Detailed exposition of DFH and its applications is given by Demianov et al. (2011).

DFH is a simulation technique that combines classical thermodynamics and hydrodynamics via constitutive relations. These relations use a particular expression for the density functional that is based on Helmholtz energy or entropy of multiphase multicomponent system. The specific expression for the density functional uses square gradients of molar densities, which enable description of surface tension. The existing realization of the DFH developed by Schlumberger Moscow Research models mass (i.e., chemical components), momentum, and energy balance together with a diffuse interface description. The diffuse interface approach is a consistent and efficient way to model the evolution of the fluid–fluid interfaces in multiphase flow. The thermodynamic state of the mixture is described by means of bulk and surface Helmholtz energies, where the latter enables correct description of liquid–solid interaction, that is, wettability and adsorption.

The method covers various classes of multiphase hydrodynamic problems while taking into account many special phenomena and allowing for complex modeling scenarios including complex compositional fluids with phase transitions: gas–liquid, liquid–liquid, liquid–solid; wettability and adsorption; complex rheologies of phases; presence of surfactants, solvents, and polymers (Figure 7). Koroteev et al. (2013 a,b) present examples of DFH applications to real problems in the oil and gas industry.

There is a high-performance computing realization of the DFH that allows simulating complex compositional flows using large models consisting of several tens of billions of cells within practical computational times.

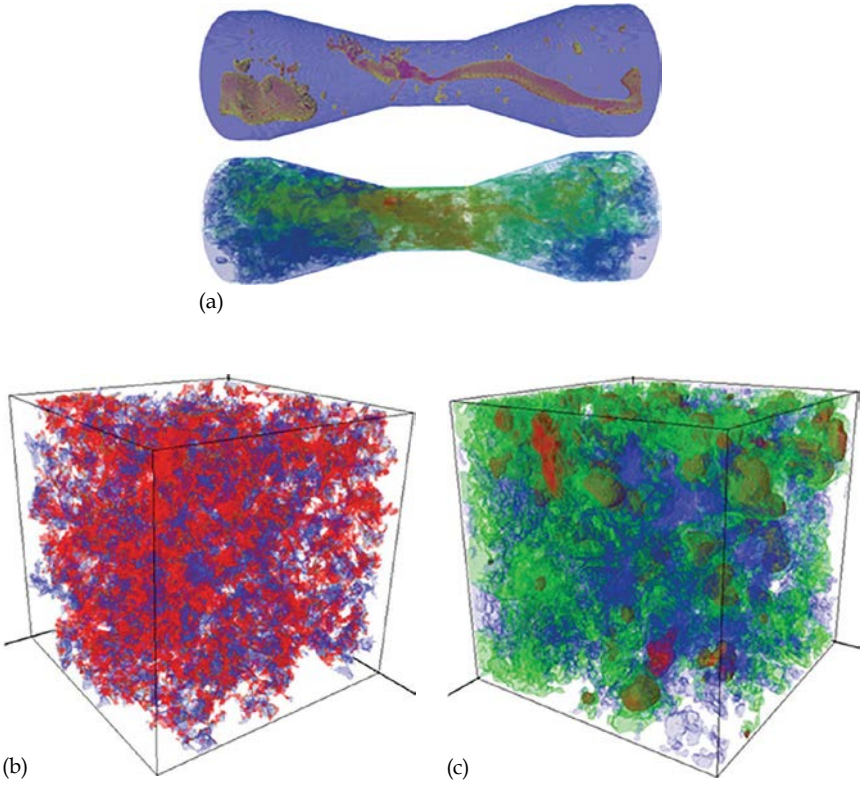


**Figure 7** DFH numerical modeling examples. (a) Two-phase turbulent flow (phases and velocity). (b) Oil primary drainage. (c) Oil recovery by water alternating gas (WAG). (Images copyright Schlumberger Technology Corporation, Sugar Land, TX. Used with permission.)

## Structural Analysis

The workflow of segmenting the 3D grayscale image into pore and grain space, identifying individual grains and mineral phases, then building pore-network or finite element meshes gives a very rich representation of the rock. It has been recognized that analyzing these representations alone can yield many insights into the microstructural properties of the rock (e.g., Thompson et al., 2005; Sheppard et al., 2006) This type of analysis yields direct information on grain sizes, aspect ratios, orientations, surface areas, etc.

## Modelling Transport Properties

Early efforts to model petrophysical properties such as absolute permeability and electrical conductivity with CT imaging held much promise but generally underestimated predictions with respect to experimental results (e.g., Schwartz et al., 1994; Spanne et al., 1994; Auzerais et al., 1996). Arns et al. (2001) recognized that some of the inaccuracies in simulating transport properties could be minimized by removing three sources of error: finite size effects, discretization errors, and statistical fluctuations. They were able to obtain accurate predictions of electrical conductivity properties on Fontainebleau sandstone.

These studies led to an expansion in the variety of petrophysical and transport properties researchers attempted to simulate from digital imagery of the microstructure. Arns et al. (2004) demonstrated that absolute permeability could be modeled on Fontainebleau sandstone over a wide range of porosities. Fredrich et al. (2006) used lattice Boltzmann simulation to compute absolute permeability on three natural and one synthetic sandstone and again obtained results consistent with experiment. Note that, at about the same time, Schembre and Kovscek (2003) were using CT dynamic imaging to infer relative permeability.

Recognizing the importance and challenges of carbonate rocks, many workers focused modeling and simulation efforts in this area. By integrating additional data sources such as high-resolution 2D thin sections, Okabe and Blunt (2004) simulated absolute permeability with reasonable results. Recognizing the multiple scales of porosity that characterize carbonates from vuggy macroporosity to intragranular microporosity, several workers (Arns et al., 2005; Lucia, 2007) imaged carbonate samples at multiple resolutions. A variety of pore-scale and petrophysical properties (permeability, drainage capillary pressure, formation factor, and nuclear magnetic resonance (NMR) response) were then computed on the highest resolution samples. Permeability measured on the small subsamples was then upscaled to the larger core sample and was found to be consistent with experimental measurements. Knackstedt et al. (2007b) presented a comprehensive study of six core plugs spanning four different classes of carbonate (oomoldic, vuggy, and bioclastic limestone, and sucrosic dolomite). Comparing modeled transport properties with experiment, they reported good results.

One of the foundational assumptions of NMR imaging of porous rocks is pore connectivity and isolation. Directly imaging the 3D pore network with CT allows this and other assumptions to be tested. Arns et al. (2005b) present an NMR-response simulation tool to model $T_1$, $T_2$ relaxation and dephasing based on pore connectivity. They studied 20 sandstone and 2 carbonate samples. Arns and Sheppard (2006), Arns et al. (2006, 2008) further developed the interpretation and modeling of NMR response.

Imaging synthetic rocks of sintered glass beads, Haney et al. (2006) modeled acoustic properties. Using finite difference simulation, they were able to show the rock behaving as

an effective medium at low frequencies and strong scattering at higher frequencies.

Archie's equations form the basis of interpreting resistivity logs:

and

where

$F$ is the formation factor, which is the ratio of the brine-saturated rock resistivity $R_0$ to the resistivity of the brine $R_w$

The resistivity index $I_R$ is the ratio of the partially brine-saturated rock $R_t$ to $R_0$ $m$ and $n$ are the cementation and saturation exponents

$a$ is an empirical constant

Variability in $m$ and $n$ as measured in the laboratory is attributed to heterogeneity between the samples. CT imaging affords the opportunity to directly image this heterogeneity and therefore yield insight into the behavior of $m$ and $n$. Knackstedt et al. (2007a) present a comprehensive study of 12 samples and are able to reconcile Archie's exponents with the observed pore structures.

## Upscaling Digital Rocks

Due to the advances in imaging and modeling at the pore scale that we have seen over the past 30 years, our understanding of the phenomena affecting multiphase fluid flow at the pore scale in petroleum reservoirs has increased substantially. However, from a practical standpoint, the motivation driving this has been to better understand how to optimize production at the scale of the entire petroleum reservoir. Thus, in parallel with advances in our knowledge of pore-scale physics, we have seen advances not only in macroscopic modeling and simulation, but also in efforts to better reconcile the physics modeled at the pore scale with that at the reservoir scale.

It should be emphasized that the range of scales we must consider and reconcile when modeling and interpreting porous media behavior in the oil field rivals that in many other fields of physics. Vega et al. (2013a) report 20 nm ($2 \times 10^{-8}$ m) resolution images of gas shale using transmission electron microscopy; this resolution is routinely obtained to analyze the mineralogical structures within porous rocks. At the other extreme, the Ghawar oil field in Saudi Arabia is 230 km in length. This range in scale represents 13 orders of magnitude.

Given the complexities of porous rock, the concept of effective properties or effective media has gained wide acceptance. The effective property of a rock at a given scale of observation or modeling is that of a simple homogeneous sample at that scale (e.g., Wang and Pan, 2008). However, the mapping of the fine scale to the coarser scale (upscaling) is not unique. This upscaling is highly dependent on the scale in question, the types of rock, the fluid phase composition and distribution, and the physics of interest.

Christie (1996) introduced many in the petroleum engineering world to the needs and challenges of upscaling geological models to reservoir simulation models. At this phase of the modeling workflow, the oil field might be composed of a geological model described by cells 10 m (width) × 10 m (length) × 0.1 m (thickness). An oil reservoir 10 km

× 10 km × 100 m would then be built from approximately $10^9$ cells. The geological model describes the spatial variation of rock types and properties. The relatively fine vertical scale describes modeled variations in the stratigraphic layering. However, for modeling fluid flow over the life of the field, for example, 30 years, this resolution is too fine from a computational perspective. The number of cells might be reduced by three orders of magnitude for effective simulation (Figure 1). Thus, a simulation model represents an effective medium model of the finer-resolution geological model. Christie (1996) outlines some of the approaches for upscaling in this scale range. For contemporary discussions on the issues related to reservoir simulation at this scale, see, for example, Fanchi (2005), Ahmed (2010), or Guo (2011) (Figure 22.8).

As discussed earlier, a typical resolution for CT imaging is 1–5 μm, which still involves upscaling approximately six to seven orders of magnitude. Hurley et al. (2012) present a workflow for upscaling from the CT scale to the reservoir scale (see Hurley et al., 2012, Figure 22.1).

Correctly modeling the rock heterogeneity is key in this upscaling process. Hurley et al. (2012) introduce the concept of representative element volume (REV) as the smallest volume of rock that can represent the rock heterogeneity within specified limits of variance of the underlying property, such as porosity or permeability, at a given scale. Thus, if at a fine scale such as a 1 μm CT image, a variance for the effective medium volume is defined for the upscaled porosity and permeability.

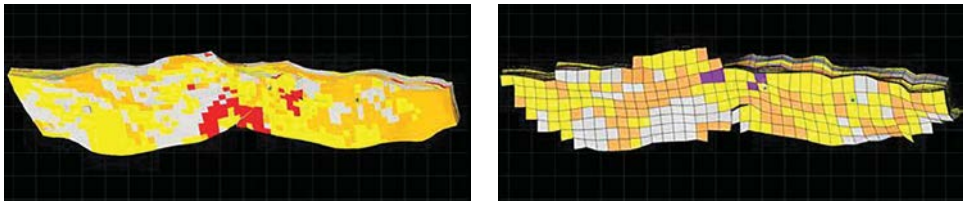


**Figure 8** Model of the oil reservoir discussed in the text. The colors represent different rock types.
(a) The fine-scale geological model and (b) the coarser upscaled simulation model. The differences between the models are partly because visualization is of the top layer and the upscaled model involves averaging over several fine layers.

The determination of REV sizes is practically determined by relating a volume to a subvolume. For example, if a 1 m volume is to be modeled, the REV is the subvolume size that yields the desired variance in a property. Many subvolumes are sampled and their property determined, and the aggregate variance of the subvolume samples computed. Subvolume size is then increased and variance recomputed. The REV is then the largest subvolume size that reflects the desired variance.

Once the REV for a given scale is obtained, it is necessary to upscale from the REV subvolume to the larger volume. This is nontrivial because of spatial autocorrelation and different physics and geological processes operating at different scales (e.g., Hilfer, 2002). A wide range of geostatistical tools and approaches are available for the autocorrelation issues depending on the scale interval of interest. For example, at the reservoir scale, multipoint geostatistics is commonly applied (e.g., Strebelle and Journel 2001). As discussed previously, when upscaling from the CT scale (1–5 μm) to the core plug scale (~10 mm), pore-network models are commonly constructed (Blunt, 1998), although additional measurements must be integrated to reduce nonuniqueness. Ghous et al. (2008) present a workflow for integrating complementary techniques with CT including thin section analysis, mercury injection experiments, and FIB-SEM. White et

al. (2006); Balhoff et al. (2007); and Sheng and Thompson (2013) present examples of coupling pore-network models with coarser continuum models.

## Future Directions

As CT imaging has become an increasingly common tool in the petroleum industry over the past 20 years, many innovative imaging, interpretation, and modeling techniques have been developed. There is now increasing recognition that robust workflows can and need to be developed that com- bine CT with other imaging tools (e.g., Kumar et al., 2010; Hurley et al., 2012). Iterative registration of images acquired with these different techniques is desirable so that consistent models at this scale are obtained.

Despite these advances in the digital petrophysics workflow, they cannot and will not replace laboratory core analysis. As such, we can expect to see improved integration of the imaging and modeling techniques described here into the overall core analysis workflow.

## Acknowledgements

I thank Schlumberger for permission to publish this work. I am grateful to Mark Andersen, Austin Boyd, Nikolay Evseev, Denis Klemin, and Alexander Nadeev for helpful discussions, reviewing of the manuscript, and providing imagery from their work.

# Chapter 5

## Core-Scale Oil Shale Pyrolysis Media in Oil Fields

Pankaj Tiwari, Josh Staten, and Milind Deo

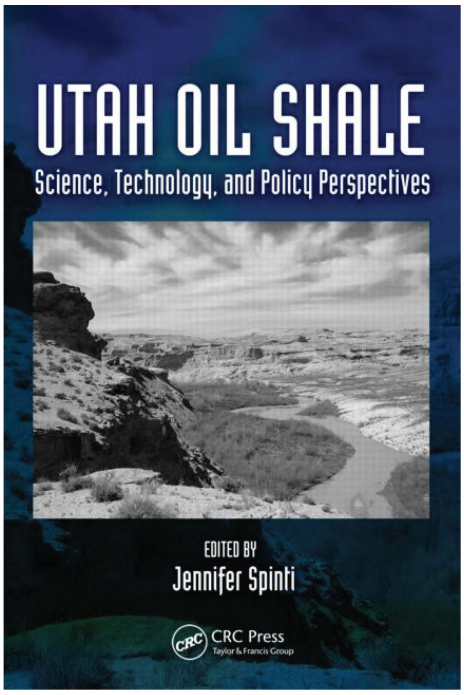


**Utah Oil Shale: Science, Technology, and Policy Perspectives**

*By* Jennifer Spinti

This chapter focuses on heat and mass transport effects in larger core samples from the Skyline 16 core and from other cores elsewhere in the Mahogany zone of the Green River Formation in Utah. It describes experiments for determining the magnitude of the effects of four factors (core size, heating regime, pressure, and temperature) on products from oil shale pyrolysis. It is shown that each of the four factors contributes to oil yield and to product distribution. These factors may be used in enhancing the techniques that exist for the production of shale oil from oil shale pyrolysis.

## Background

Different in situ and ex situ technologies have been proposed for commercial oil shale development. Royal Dutch Shell built a pilot-scale facility that employed the in situ conversion process (ICP) in which the oil shale is gradu-ally heated with electric heaters to a temperature of about 350°C. ExxonMobil's ElectroFrac™ process fractures the oil shale using a hydraulic fluid then fills the fractures with a conductive material, creating a planar heater. For ex situ processing, the Petrobras Petrosix gas combustion retort is a conventional oil shale process, pyrolyzing 7800 tons of crushed oil shale per day. Red Leaf's EcoShale® in-capsule process technology was operated successfully in a 2009 field pilot in which a capsule filled with oil shale was heated by a gas-fired, closed-loop piping system (Red Leaf Resources 2015). Each method varies in implementation, but the underlying physical restraints of kinetics, thermodynamics, heat transfer, and mass transport must be overcome at a low enough cost to make the technologies economically feasible for commer-cial oil production from oil shale.

Pyrolysis of oil shale occurs at approximately 300°C, the temperature at which the endothermic energy barrier is overcome; the decomposition rate then accelerates as the temperature increases. There are four physical phenomena that need to be addressed to optimize shale oil production via oil shale pyrolysis. One, heat transfer through the oil shale is the key to unlocking the oil from the oil shale kerogen in an economical manner. Two, reaction kinetics shows the optimum heat regime for maturing the kerogen into oil. Three, mass transfer moves products of the matured kerogen through the rock to a recoverable area. Four, thermodynamics affects each of the other phenomena; as the products are formed, their intrinsic properties change. Each of the four phenomena is affected by the nature of the rock and of the kerogen, by the type of heat source used, by the pressure of the system, and by the time the oil shale is held at a given set of conditions.

A good model of oil shale pyrolysis will bridge the gap between in situ and ex situ retorting, enabling experts in the field to compare the costs and benefits of different technologies. For example, the kinetic model of kerogen decomposition will be identical in both processes. Heat and mass transfer models will be dictated by the process and by the particle characteristics. The accuracy of predictions from in situ models will be governed by the heterogeneity of the formation, whereas predictions from the more tightly

controlled ex situ processes will have narrower uncertainty bands. To predict oil yields for in situ pyrolysis, any model must be validated against available experimental data. As described in the next section, Tiwari performed the initial steps in the validation process by obtaining thermo-gravimetric analysis (TGA) data for determining kinetic rates, high-pressure TGA (HPTGA) data for determining pressure effects on kinetic rates, TGA with mass spectrometry (TGA-MS) data for determining stoichiometric com-position, and data from the multiscale pyrolysis of different sizes of core samples for determining scaling factors due to size.

## Oil Shale Pyrolysis Experiments

This section describes the experimental procedures that were performed and presents selected results from the characterization, pyrolysis, and pyrolysis product analysis of three sets of oil shale samples. The first two sets of samples were provided by the Utah Geological Survey and were from the Mahogany zone of the Green River Formation in Utah. Sample #1 (S1) was a powdered oil shale sample, while Sample #2 (S2) was a set of four samples, including three cores (0.75 in., 1 in., and 2.5 in. in diameter) and one powdered sample. The third set of samples was from the 4 in. diameter Skyline 16 core discussed in Chapters 4, 5 and 6. This set included three fresh, organic-rich (Mahogany zone) samples: GR1 (461.1–462.1 ft in depth), GR2 (485.9–486.9 ft), and GR3 (548.1–549.1 ft). More detailed results can be found in Tiwari (2012).

### Oil Shale Characterization

#### *S1 and S2*

The prepyrolysis (e.g. raw) S1 and S2 oil shale samples were tested for inherent moisture and characterized using elemental analysis and x-ray diffraction (XRD). To test for inherent moisture, small quantities of powdered S1 and S2 samples were dried at 100°C for 4 h. No significant weight loss was observed, so the samples were used as received. Elemental analysis was done to characterize the common elements found in the organic portion of the oil shale. A LECO CHNS-932 analyzer was used for carbon (C), hydrogen (H), nitrogen (N), and sulfur (S) and a VTF-900 analyzer for oxygen (O). Using the O/C and H/C ratios, both S1 and S2 were located on a van Krevelen chart as type I kerogens. The results of the elemental analysis are shown in Table 7.1. The raw oil shale samples were ground to 325 mesh in a micronizing mill and then characterized using XRD. The mineral composition is important for determining the likelihood that the TGA, and multiscale pyrolysis results are affected by mineral interactions. The results of the XRD characterization are given in Table 7.2. While there are many constituents, dolomite (33.5 wt% and

**TABLE 7.1**

Elemental Analysis (CHNSO) Results for the Raw Oil Shale Samples

| | Sample #1 | | Sample #2 (Powder) | |
|---|---|---|---|---|
| **Element** | **Weight %** | **Std Dev** | **Weight %** | **Std Dev** |
| Carbon | 17.45 | 0.26 | 22.09 | 1.00 |
| Hydrogen | 1.60 | 0.08 | 2.14 | 0.12 |
| Nitrogen | 0.53 | 0.06 | 0.65 | 0.06 |
| Sulfur | 0.18 | 0.04 | 0.11 | 0.02 |
| Oxygen | 15.69 | 0.79 | 16.54 | 0.97 |
| H/C (molar) | 1.10 | — | 1.17 | — |
| O/C (molar) | 0.67 | — | 0.56 | — |

*Note:* Molar H/C and O/C ratios are calculated for kerogen typing.

**TABLE 7.2**

Results from XRD of Oil Shale Rock

| | Weight % | | |
|---|---|---|---|
| **Mineral** | **Sample #1** | **Sample #2** | **Chemical Formula** |
| Quartz | 7.7 | 7.7 | $SiO_2$ |
| Plagioclase | 19.5 | 7.60 | $CaAl_2Si_2O_8$ |
| Calcite | 6.9 | 3.95 | $CaCO_3$ |
| Illite | 5.8 | 2.84 | $(K,H_3O)(Al,Mg,Fe)_2(Si,Al)_4O_{10}[(OH)_2,(H_2O)]$ |
| Dolomite | 33.5 | 62.93 | Ca Mg $(CO_3)_2$ |
| Orthoclase | 12.4 | 10.88 | $KAlSi_3O_8$ |
| Aragonite | 11.7 | – | $CaCO_3$ |
| Analcime | 2.4 | 4.13 | $NaAlSi_2O_6{\cdot}H_2O$ |

62.93 wt% in S1 and S2, respectively) is the predominant mineral in both samples. Illite and analcime, also found in both samples, may add to the complexity of modeling the pyrolytic reactions because water is released from these minerals at a relatively low temperature. Another modeling complexity is the release of carbon dioxide ($CO_2$), oxygen ($O_2$), and other mineral emissions as the inorganic portion of the oil shale decomposes. These potential interactions and decompositions are not considered in the model developed here.

#### *7.2.1.2 GR1, GR2, and GR3*

Elemental (CHNS) and TGA analyses were conducted on uniformly mixed, powdered (100 mesh) shale samples of GR1, GR2, and GR3. TGA experiments were also performed on the isolated kerogens from these samples (GR1.9, GR2.9, and GR3.9). The kerogens were isolated from the homogenous pow-dered samples of GR1, GR2, and GR3 shales using a series of strong acids (demineralization process) as described in Chapter 5. The elemental analysis was repeated three times for each sample, and the average values with

**TABLE 7.3**

Elemental Analysis (CHNS) of Skyline 16 (GR) Samples

| Sample ID | C (wt%) | H (wt%) | N (wt%) | S (wt%) |
|---|---|---|---|---|
| GR1 | 33.93 ± 5.76 | 3.21 ± 0.21 | 1.17 ± 0.27 | 0.56 ± 0.68 |
| GR2 | 19.80 ± 5.23 | 1.40 ± 0.64 | 0.47 ± 0.19 | 0.13 ± 0.17 |
| GR3 | 20.44 ± 1.00 | 1.84 ± 0.05 | 0.71 ± 0.11 | 0.18 ± 0.15 |

**TABLE 7.4**

TGA Analysis (Weight Loss) of Skyline 16 (GR) Samples and Their Isolated Kerogens (GR X.9) at Heating Rates of 10°C/min

| | Samples ID | Sample (mg) | Organic (%) | Mineral (%) | Coke (%) |
|---|---|---|---|---|---|
| Oil shale | GR1 | 18.16 | 21.13 | 17.86 | 1.63 |
| | GR2 | 17.00 | 7.20 | 29.85 | 0.0 |
| | GR3 | 23.11 | 11.16 | 20.43 | 0.34 |
| Isolated kerogen | GR1.9 | 4.32 | 70.58 | — | 15.57 |
| | GR2.9 | 2.3 | 80.81 | — | 11.98 |
| | GR3.9 | 6.77 | 67.58 | — | 10.92 |

standard deviation are reported in Table 7.3. The TGA results from the original shale samples and from the kerogen isolates are summarized in Table 7.4. Details of the TGA experiments are found in Section 7.2.2.2.

The samples analyzed reflect considerable variation in the organic versus mineral composition as well as in the elemental composition. GR1 had the highest organic content of the three samples at 21.13 wt%, while GR2 had only 7.2% organic content. GR2 had the highest content of minerals that decompose at high temperature (29 wt%). A similar trend was observed in the elemental analyses. The weight percents of C, H, N, and S were higher in the organic-rich GR1 sample than in the organic-lean GR2 sample.

### 7.2.2 Experimental Procedures

Four different sets of experimental procedures, summarized in Table 7.5, were employed to study the phenomena associated with production of shale oil via oil shale pyrolysis. These procedures were carried out on the pow-dered and core samples discussed above (or in the previous section). S1 was used in all four sets of experimental procedures, S2 was used in three sets (excluding TGA-MS), and the Skyline 16 samples were used in two sets.

#### *7.2.2.1 TGA Pyrolysis Experiments on S1 and S2 Samples*

TGA was performed on S1 and S2 (powder) to obtain intrinsic reaction rates of the oil shale. This procedure was similar to that performed on the Skyline

**TABLE 7.5**

Experimental Procedures Performed on Powdered and/or Oil Shale Core Samples

| Oil Shale Sample | Size | Experimental Procedure |
|---|---|---|
| Sample #1 | Powder | TGA<br>HPTGA<br>TGA-MS<br>Multiscale pyrolysis (1 in. Swagelok reactor) |
| Sample #2 | Powder | TGA<br>HPTGA |
| | 0.75 in. diameter | Multiscale pyrolysis (1.25 in. Swagelok reactor) |
| | 1 in. diameter | Multiscale pyrolysis (1.25 in. flange reactor) |
| | 2.5 in. diameter | Multiscale pyrolysis (3.0 in. flange reactor) |
| GR1 | Powder | TGA |
| | 1 in. diameter | Multiscale pyrolysis (1 in. Swagelok reactor) |
| GR2 | Powder | TGA |
| | 1 in. diameter | Multiscale pyrolysis (1 in. Swagelok reactor) |
| GR3 | Powder | TGA |
| | 1 in. diameter | Multiscale pyrolysis (1 in. Swagelok reactor) |

*Notes:* All samples are from the Mahogany zone of the Green River Formation in Utah. Multiscale pyrolysis was performed at various heating rates, final temperatures, pressures, and operating modes (batch, semibatch, and continuous).

16 oil shale samples in Chapter 5. TGA measures the change in weight of a sample undergoing pyrolysis to indirectly observe the progress of reactions. TA Instrument's Q500 was the TGA equipment used in these experiments. It controlled the temperature of the reaction chamber up to a maximum of 1000°C using electrical heating, accommodated a total gas flow rate of 100 mL/min and provided heating rates from 0.1°C/min to 100°C/min.

The TGA was purged with nitrogen ($N_2$) for 15 min prior to initiating the experiment. Approximately 20 mg of sample was placed in a platinum basket attached to a microbalance with a small wire. Mass or heat transport effects were assumed to be negligible because of the size of the particles. The reactor was then heated to the desired temperature at a set heating rate. For the TGA and TGA-MS experiments, the balance gas ($N_2$) was maintained at flow rates of 40 and 10 mL/min and the purge gas at 60 and 90 mL/min, respectively. For the isothermal tests, the samples were rapidly heated (heating rate of 100°C/min) to a predetermined final temperature between 200°C and 550°C. For the non-isothermal tests, the heating rate was varied between 0.5°C/min and 50°C/min.

The HPTGA experiments were performed on S1 and powdered S2 samples to determine pressure effects on intrinsic reaction rates and on product distribution. The Cahn TherMax 500 HPTGA from Thermo Fischer was used.

TGA-MS experiments were performed on S1 to determine at which temperature the targeted components evolved. To conduct the experiments, the TGA described earlier was coupled with a Thermostat model GSD 301 TC from Pfeiffer Vacuum MS.

### *7.2.2.2 TGA Pyrolysis Experiments on GR Samples*

TGA pyrolysis/combustion experiments were performed on powdered samples of GR1, GR2, and GR3 at a heating rate of 10°C/min to measure the organic and mineral content of the samples and to estimate the coke formed during pyrolysis. The final temperature for the pyrolysis experiments was 1000°C and for the combustion experiments was 600°C. The final hold times were 10 min for all experiments. The pyrolysis was divided into two stages: the first peak (organic), which appeared from ambient to 600°C (depending on heating rate), and the second peak (mineral decomposition), which occurred from 600°C to 1000°C. After pyrolysis, the sample was cooled to 400°C in an $N_2$ environment without opening the furnace. Then, air was supplied to combust the sample, and the sample was heated to 600°C. Finally, the sample was held isothermally at 600°C for 10 min to ensure complete combustion of the any coke that had formed. This scheme can be seen in Figure 7.1.

Similar TGA pyrolysis/combustion experiments were also performed on the isolated kerogens from these samples (GR1.9, GR2.9, and GR3.9). The pyrolysis experiments were performed at three heating rates, 5°C/min, 10°C/min, and 20°C/min. The second peak (mineral decomposition) does not appear in these kerogen samples.

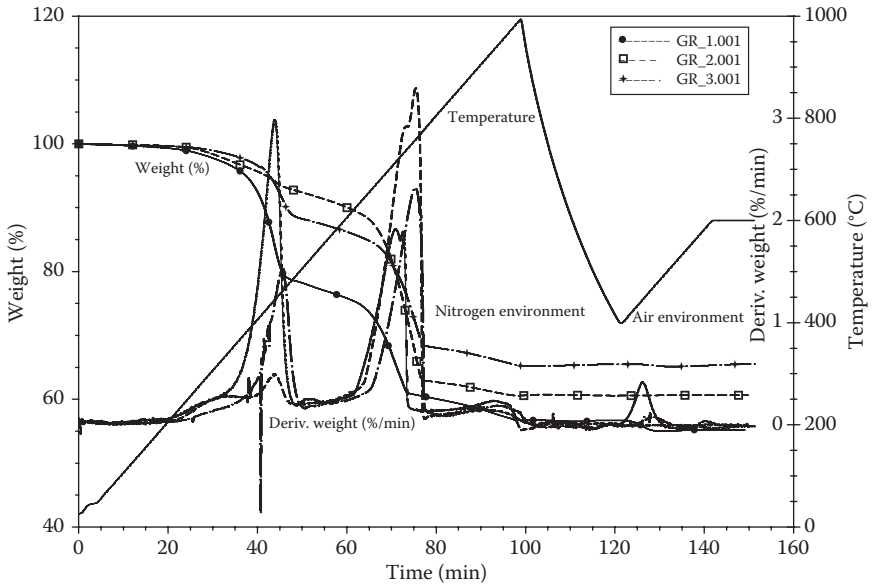


**FIGURE 7.1**
Scheme of different stages of TGA analysis to estimate the organic, mineral and coke content of the material (raw or spent shales). Example of GR powdered samples.

#### *7.2.2.3 S1 and S2 Multiscale Pyrolysis Experiments*

The multiscale pyrolysis experiments were run in batch, semibatch, and continuous flow conditions at temperatures of 350°C, 425°C, and 500°C and at pressures of psig (ambient pressure) and 500 psig. A specified heating rate was applied until the desired temperature was reached. The samples were then tested at 6, 12, 18, 24, and 48 h. In batch mode, the system was closed and no products escaped the reaction chamber. This mode simulates an in situ condition where the pyrolysis products do not reach a pressure that fractures the rock. In semibatch mode, products were allowed to escape out of the top of the reactor, but no sweep gas was used. This mode simulates an in situ condition where the products escape the system by their generated pressure and by the given conditions. In continuous mode, the reactor was swept with gas; any product that was exuded was swept out of the reaction chamber and the secondary reactions were quenched. This condition simulates ideal conditions in a reservoir with high flow capacity. However, immediate removal and quenching of pyrolysis products from the heated zone is impractical at an industrial scale with current in situ technology.

Pyrolysis experiments were performed on S1 under batch, semibatch, and continuous reactor conditions to determine how the primary reaction products may continue to break down with differing residence times at reaction conditions. Then, pyrolysis experiments were performed on S2 (0.75–2.5 in. diameter cores) under continuous reactor conditions to evaluate transport resistances (mass and heat) and to study the effects of pressure (0 and 500 psig), core size (0.75–2.5 in. in diameter), heating rate (nonisothermal, 1°C/min–10°C/min; isothermal, 100°C/min), and final temperature (300°C–500°C) on product yield and distribution.

Four different cylindrical reactors were constructed for the analysis: 1 in. × 6 in. (diameter by length), 1.25 in. × 8 in., 1.25 in. × 12 in., and 3 in. × 10 in. These reactor sizes were chosen to house the powdered and core sam-ples with minimal dead volume. All reactors were constructed of 316 stainless steel rated to 4000 psi at 600°C. Heating tape heated the three smaller reactors and a ceramic heater band heated the 3 in. × 10 in. reactor. The reac-tors and fittings were insulated using glass wool and high-temperature silicon tape. High-pressure Swagelok fittings were used for the 1 in. × 6 in. and 1.25 in. × 12 in. reactors. These reactors were used to test the powdered core samples (S1 and S2) and the 0.75 in. core (S2), respectively. Graphite flanges were used to seal both ends of the 1.25 in. × 8 in. and 3 in. × 10 in. reactors. The flange reactors were used to test the S2 1 in. and 2.5 in. cores, respectively.

Type K thermocouples were used to find the temperature profile through the core for each case. The thermocouples were inserted 0.6 in. into the core through 0.128 in. diameter holes drilled through the reactor and the core sample as illustrated in Figure 7.2. The 1.25 in. flange reactor had holes designed to monitor the temperature at the center of the core (TC-1), the sur-face of the core (TC-4), and the surface of the reactor (TC-5). The two Swagelok

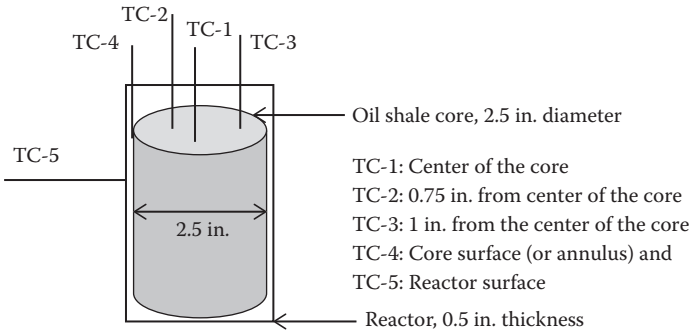


**FIGURE 7.2**
Schematic of thermocouple placement for the 2.5 in. diameter core sample. All thermocouples used in the tests were of type K.

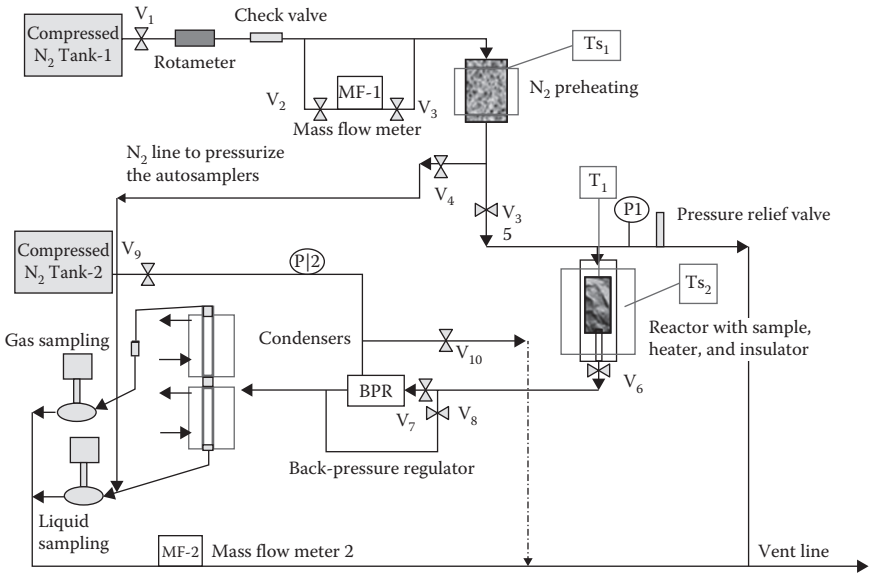


**FIGURE 7.3**
Experimental setup used to study the effect of operational parameters on yield and quality of the pyrolysis product distribution.

reactors were designed to monitor TC-1 and TC-5. The 3 in. flange reactor was designed to monitor all five of the thermocouples in Figure 7.2.

A schematic for the continuous flow experiments is shown in Figure 7.3. The system allowed for the immediate collection of the products formed from the pyrolysis reactions. The products were then condensed, sampled, and analyzed. The walls of the chamber were heated, and the reactor temperature

was controlled using SPECVIEW and either TC-1 or TC-5, depending on whether the experiment was isothermal or non-isothermal. The $N_2$ was preheated before entering the reaction chamber. Temperature and gas flow rates were recorded using LabVIEW. Pressure was controlled using a Swagelok back-pressure regulator. A heater kept the line from the reactor to the back-pressure regulator at a constant temperature of 200°C. The condensers were cooled using a Brookfield TC501 bath with controller. Samples were taken using a 12 port auto-sampler with a VCOM interface.

#### *7.2.2.4 Skyline 16 Multiscale Pyrolysis Experiments*

Each core (GR1, GR2, GR3) was dissected into three sections (Figure 7.4). These sections were then tested in continuous flow isothermal experiments at 350°C, 425°C, and 500°C with hot $N_2$ flow (~100 mL/min) for 24 h. The temperature of the reactor surface (TC-5) was used to control the pyrolysis temperature. Temperature profiles were recorded at three points: reactor surface (TC-5), core surface (TC-4), and at the center of the core (TC-1). The steady-state temperature difference between the reactor surface and the center of the core was about 50°C while that between the core surface and center of the core was 20°C.

#### *7.2.2.5 Pyrolysis Product Analysis*

Oil and gas samples were collected for compositional analyses after pyrolysis. The fluid collected in the condensers after pyrolysis was analyzed using gas chromatography (GC) and GC/MS (only selected samples) to determine com-position. The GC chromatograms were converted to carbon number distribu-tion by using simulated distillation procedures. Produced oil was analyzed using FTIR to find the wax appearance temperature of the oil, densitometry to find the density of the oil, and rheometry to find the viscosity of the oil.

Pyrolyzed samples (e.g., spent shales) from the multiscale pyrolysis reac-tor (either powders or cores) were subjected to TGA analysis to estimate the amount of unreacted organic material and of coke/char left in the rock. To perform these tests, the solid material collected after the reactor pyrolysis was

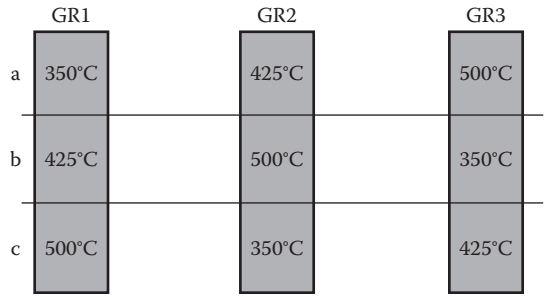


**FIGURE 7.4**
GR core sections subjected to isothermal pyrolysis under different temperatures.

crushed/ground to a powder (if the sample was a core) or used "as-is" (if the sample was a powder). Then, the TGA analysis discussed in Section 7.2.2.2 was performed. For these samples, the first pyrolysis peak (organic) was the unreacted organic material remaining in the sample after the pyrolysis reactor experiment. The weight loss during the combustion stage corresponded to the coke that formed during pyrolysis.

## 7.3 Pyrolysis Experimental Results and Discussion

Results of the non-isothermal TGA experiments and of the isothermal and non-isothermal, multiscale pyrolysis experiments are presented in this section; isothermal TGA results were not used in the kinetic model and are not presented in this chapter. For full results and details, including results from the HPTGA and TGA-MS experiments, see Tiwari (2012).

### 7.3.1 Determination of Oil Shale Pyrolysis Rates Using TGA Data

Results from the non-isothermal TGA of S1 are seen in Figure 7.5. The different symbols connected by lines represent the mass loss at heating rates

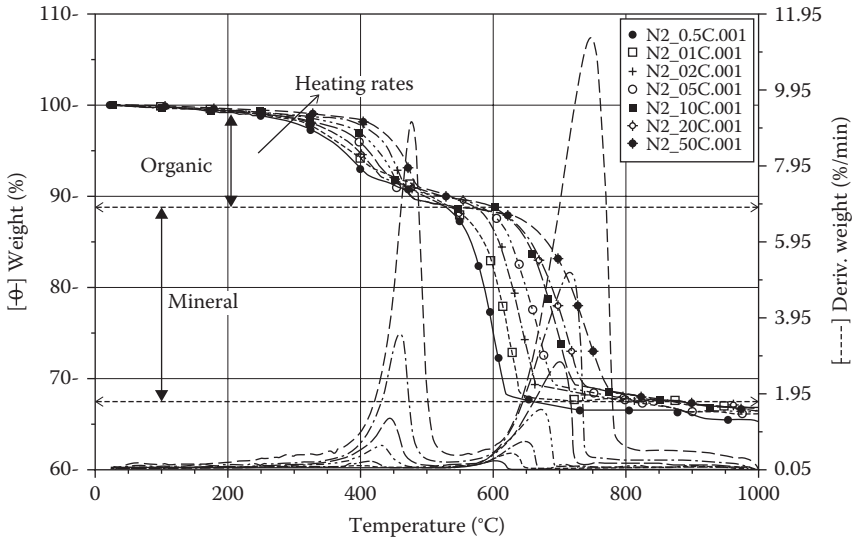


**FIGURE 7.5**
Nonisothermal thermogravimetric analysis pyrolysis thermograms of S1 at heating rates from 0.5°C/min to 50°C/min in an $N_2$ environment. The solid lines are weight curves and the dashed lines are the corresponding derivatives. The first derivative peak represents organic weight loss and the second peak represents mineral weight loss.

ranging from 0.5°C/min to 50°C/min, while the lines represent their corresponding time derivatives. Based on these TGA results and on results from other researchers (Franks and Goodier 1922), it is inferred that pyrolysis begins when the oil shale reaches approximately 300°C.

From the non-isothermal TGA data of S1, kinetic parameters were calculated using the advanced isoconversional method, described briefly here and more extensively in (Vyazovkin and White 2000). In this method, the TGA weight loss data are used to calculate the activation energy as a function
of α, the normalized weight loss, or sample conversion (Equation 7.1), using Equation 7.2:

$$\alpha = \frac{W_0 - W_t}{W_0 - W_\infty} \tag{7.1}$$

$$\frac{d\alpha}{dt} = f(T) \cdot f(\alpha) = A \cdot e^{\frac{-E}{RT(t)}} \cdot f(\alpha) \tag{7.2}$$

where

$W_0$ is the initial sample weight
$W_t$ is the weight at any given time ($t$)
$W_\infty$ is the final weight
$A$ is the pre-exponential factor
$E$ is the activation energy
$R$ is the universal gas constant
$T(t)$ is the temperature at time $t$.

Figure 7.6 shows the activation energies for the kerogen in the oil shale range from 93 to 245 kJ/mol and the values of $A \cdot f(\alpha)$ vary from 1.42E6 to 4.46E16 $min^{-1}$.

Figure 7.7 shows the fit of the model to the S1 experimental data for normalized conversion of kerogen to products (initial and final conversion set to zero and one, respectively) versus temperature for heating rates ranging from 0.5°C/min to 50°C/min. The lower heating rates show the decomposition reaction starting just above 250°C, but there is a thermal induction period for higher heating rates. Inferring from Figure 7.7, slower heating rates require lower temperatures but longer process time to reach full conversion (~830 min at 0.5°C/min versus ~10 min at 50°C/min).

### 7.3.2 TGA Results for GR Samples and Their Kerogen Isolates

The TGA results from the original GR1, GR2, and GR3 powdered samples and from their powdered kerogen isolates were presented in Table 7.4. The onset points of GR1.9 kerogen decomposition coincide with those of organic

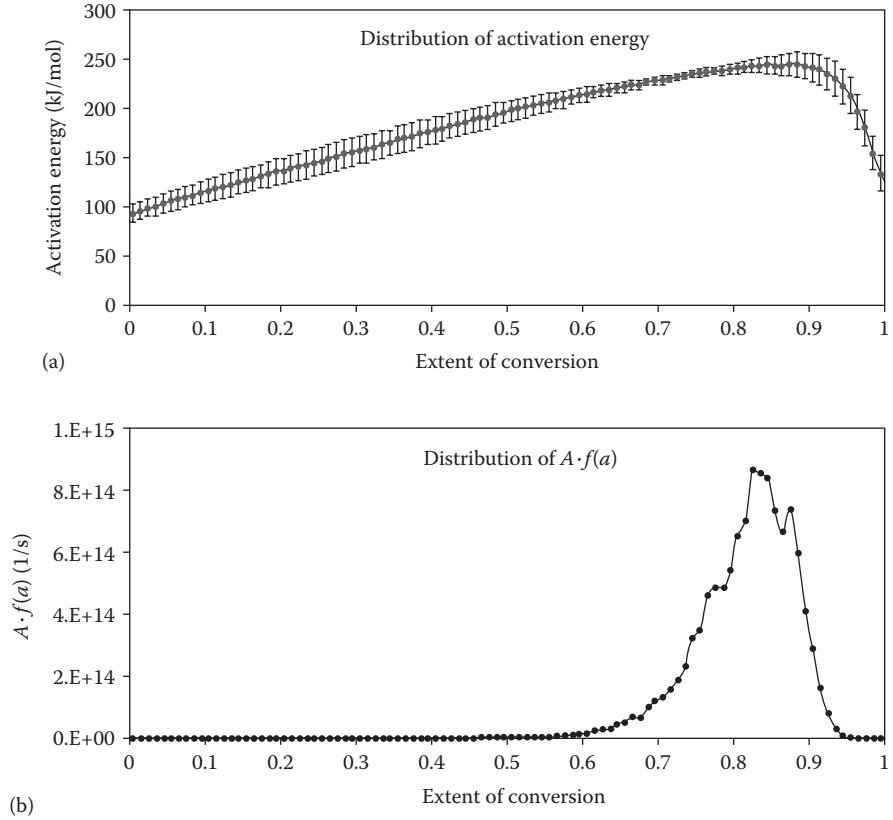


**FIGURE 7.6**
Kinetic parameters obtained using the TGA data shown in Figure 7.5. Distribution of activation energies and pre-exponential factors as a function of conversion are shown.

matter in the original GR1 shale under identical conditions as shown in Figure 7.8. The raw shale and isolated kerogen have similar decomposition patterns, which suggests that the kerogen decomposition is not affected by the inorganic material present. Also, the results from the kerogen isolates (GR1.9, GR2.9, and GR3.9) show that the onset points (start and end) in the pyrolysis zone of all three kerogens are identical (Tiwari 2012).

For the kerogen isolates, the coke formed during pyrolysis varies in the range of 10–15 wt% of initial kerogen weight and is highest for GR1.9; see Table 7.4. This trend is also observed during the TGA pyrolysis of the raw oil shale samples, where the amount of coke formed during pyrolysis correlates to the amount of the organic matter in the original sample. Coke formation is a maximum in the organic-rich GR1 sample, while there is no coke formation during the GR2 pyrolysis.

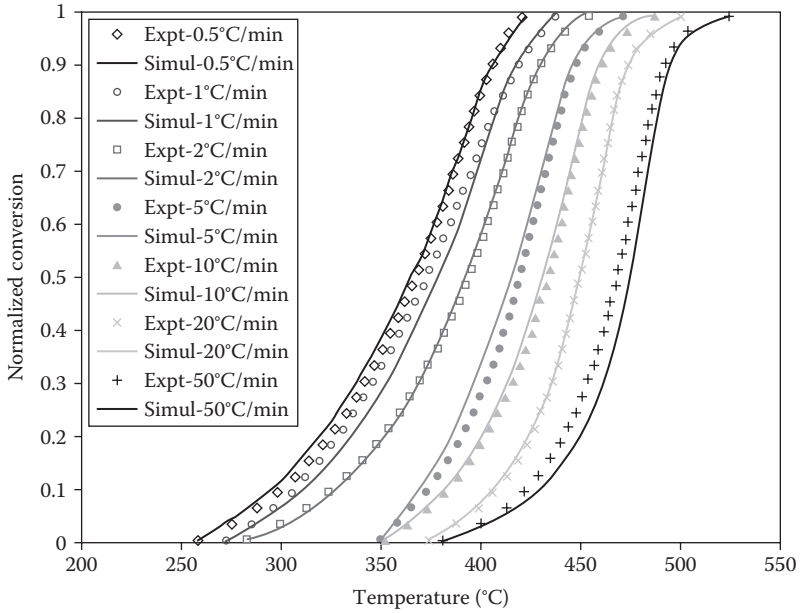


**FIGURE 7.7**
Experimental and simulated conversion profiles at different heating rates using the advanced isoconversional method.

### 7.3.3 Multiscale Pyrolysis Results

Pyrolysis was performed at four scales (powder and 0.75 in., 1 in., and 2.5 in. diameter cores) using the apparatus shown in Figure 7.3. The results and findings are presented in this section.

#### *7.3.3.1 Pyrolysis of Powder Sample (S1)*

S1 was pyrolyzed in the 1 in. Swagelok reactor in batch, semibatch, and continuous flow modes at various temperatures (350°C, 425°C, and 500°C) and pressures (ambient pressure and 500 psig).

Selected results for the batch experiments can be seen in Figure 7.9; batch experiments were considered to be isothermal with heating rates of 100°C/min. As noted in Section 7.2.2.5, the weight percent of unreacted organic material and that of coke after pyrolysis were determined using TGA (in inert and then oxidizing environments). Hold time and pressure appear to affect coke formation as the only significant coke that formed (0.28 and 1.20 wt%) in the batch experiments came after 6 and 18 h of heating at 500°C and an initial pressure of 500 psig. There was negligible coke formed at 500°C and ambient initial pressure. Also at ambient pressure, no appreciable products formed until the temperature reached 425°C. There is a distinct trend of more product at higher pressure.

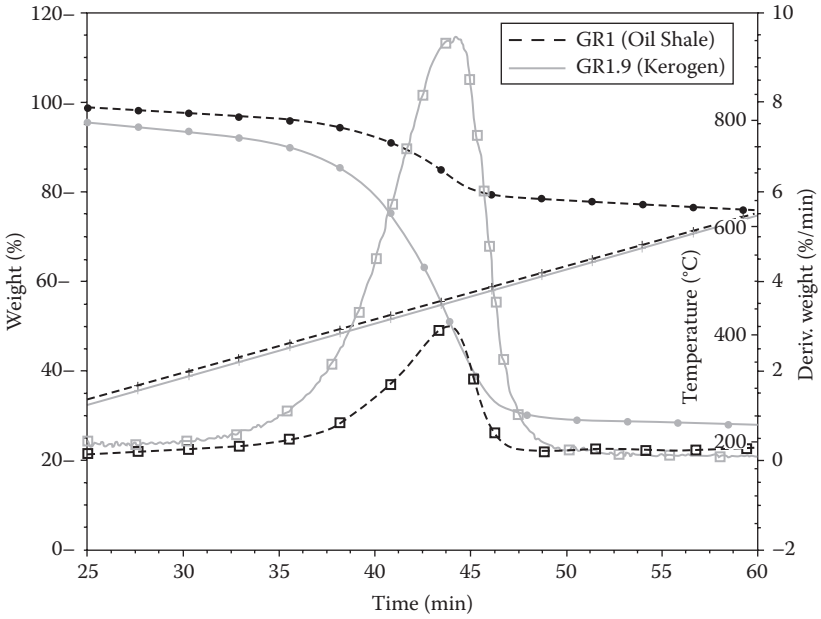


**FIGURE 7.8**
Comparison of the onset points for organic matter decomposition during the pyrolysis (10°C/min in $N_2$ environment) of isolated kerogen (GR1.9) and of the raw oil shale (GR1). The straight lines correspond to the temperature.

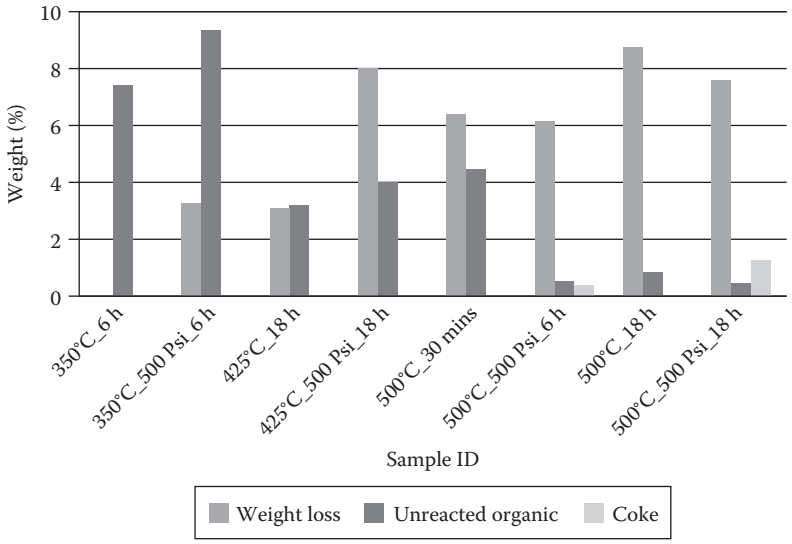


**FIGURE 7.9**
Weight loss, unreacted organic content, and coke results from the batch pyrolysis of S1 followed by the TGA analysis of spent shale.

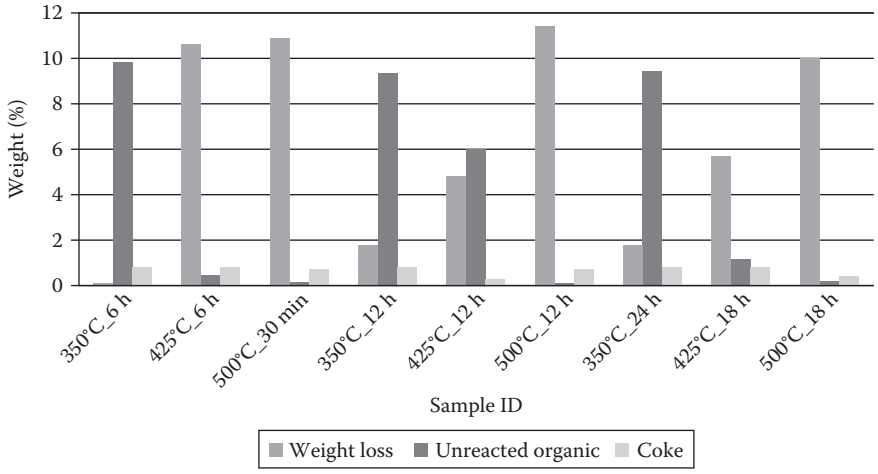


**FIGURE 7.10**
Weight loss, unreacted organic content, and coke results the semibatch pyrolysis of S1 followed by the TGA analysis of spent shale.

Selected results for the semibatch mode can be seen in Figure 7.10. All semibatch experiments were considered to be isothermal with heating rates of 100°C/min. Hold time had a negligible effect on the higher-temperature experiments and a small effect on the experiments at 350°C (2% weight loss after 24 h compared to negligible weight loss after 6 h). In contrast to the batch experiments, coke formation was observed at all temperatures, although it never exceeded 1% by weight.

Under continuous flow conditions, no coke was found for heating rates below 5°C/min, but there was 0.89 wt% coke found in the sample heated to 500°C at a rate of 10°C/min. The oil yield reflected the heating rate, i.e., higher heating rates yielded more oil.

These powdered oil shale experiments provide insight into the challenges faced with in situ retorting of oil shale to produce shale oil. The results from the batch and semibatch pyrolysis of S1 show that the product composition is dependent on temperature, pressure, and residence time; higher values for these parameters create more coke. The continuous flow experiments show that maximum oil production can be achieved by opti-mizing the heating rate and the oil extraction rate; oil production is maxi-mized at high heating rates and high oil extraction rates (instantaneous product extraction and quenching). However, for in situ processes, this situation is not possible.

#### *7.3.3.2 Pyrolysis of 0.75 in. Diameter S2 Core*

Table 7.6 lists the elemental analysis (CHNSO) of three 0.75 in. diameter S2 oil shale core samples after pyrolysis (spent shale) and of the pyrolysis products

**TABLE 7.6**

Elemental Analysis of Three 0.75 in. Diameter S2 Oil Shale Cores and Their Pyrolysis Products (shale oil)

| Samples | Pyrolysis Temperature | C (wt%) | H (wt%) | N (wt%) | S (wt%) | O (wt%) | Total | H/C (molar) | O/C (molar) |
|---|---|---|---|---|---|---|---|---|---|
| Oil shale (powdered) | — | 22.09 | 2.14 | 0.65 | 0.11 | 16.54 | 41.53 | 1.17 | 0.56 |
| Spent shale | 300°C | 14.12 | 0.44 | 0.26 | 0.01 | 25.42 | 40.24 | 0.38 | 1.35 |
| | 350°C | 14.10 | 0.82 | 0.47 | 0.02 | 20.87 | 36.28 | 0.70 | 1.11 |
| | 400°C | 13.06 | 0.21 | 0.27 | 0.01 | 27.99 | 41.54 | 0.19 | 1.61 |
| Shale oil | 300°C | 79.72 | 10.72 | 2.34 | 0.65 | 2.36 | 95.79 | 1.61 | 0.02 |
| | 350°C | 79.91 | 10.91 | 2.34 | 0.62 | 1.93 | 95.71 | 1.64 | 0.02 |
| | 400°C | 80.89 | 11.10 | 2.05 | 0.65 | 2.13 | 96.82 | 1.65 | 0.02 |

*Note:* Oil shale refers to the prepyrolysis samples, while spent shale refers to the post-pyrolysis sample.

at three temperatures (300°C, 350°C, and 400°C). For comparison, the analysis of the powdered S2 oil shale sample prior to pyrolysis is also included. This analysis gives material constraints for the products formed during pyrolysis; in particular, the H/C ratio gives the best idea of what type of oil or quantity of coke will result from pyrolysis.

Results from the pyrolysis of the 0.75 in. diameter cores are shown in Table 7.7. For the ambient pressure experiments, the test at 400°C had the highest oil yield and weight loss. For the high-pressure experiments (500 psig), the test at 500°C had the highest oil yield and weight loss. It can be inferred from Table 7.7 that high pressure results in a higher gas yield, while the oil yield does not change significantly.

While the kinetic model for oil shale pyrolysis described in Section 7.3.1 predicts that higher pressure results in higher coke formation, in the 0.75 in. core pyrolysis, the high-pressure experiment at 400°C results in lower coke yields (0.22 wt%) than the 400°C experiment at ambient pressure (5.78 wt%) (Table 7.7). These results illustrate that pressure is not the only factor influencing coke formation and that core heterogeneity is a large source of uncertainty (the S2 cores were not taken from the exact same location/depth).

#### *7.3.3.3 Pyrolysis of 1 in. Diameter S2 Core*

Results from the pyrolysis of 1 in. diameter S2 core samples at 500°C and ambient pressure for three heating rates (1°C/min, 5°C/min, 10°C/min) can be seen in Table 7.8. The results indicate that the lower heating rates yield more oil at a cost of process time. This increase in oil yield at low heating rates may be due to the oil shale spending more time in a temperature range that limits secondary reactions such as coking and cracking while the oil is expelled from the core. Another advantage of the lower heating rate is that a higher grade of oil (e.g., lighter compounds) is produced as seen in the combined naphtha and middle distillate condenser fractions in Figures 7.11 and 7.12 for heating rates of 5°C/min and 10°C/min, respectively.

#### *7.3.3.4 Pyrolysis of 2.5 in. Diameter S2 Core*

The 2.5 in. diameter core sample had the greatest heat and mass transport effects of the sizes tested. The temperature distributions for a series of isothermal experiments are shown in Figure 7.13; please refer to Figure 7.2 for the locations of the thermocouples. The anomalies in the temperature readings, listed below, are most likely from the heterogeneity of the core, the deviance from ideal conditions (e.g., symmetry, insulation), and/or the secondary reactions:

**TABLE 7.7**

Results for the Isothermal Pyrolysis of the 0.75 in. Diameter S2 Oil Shale Core

| | Pyrolysis Conditions | | | Reactor Pyrolysis | | | TGA of Spent Shale | |
|---|---|---|---|---|---|---|---|---|
| Experiment # | Temperature (°C) | Pressure (psig) | Sample Mass (g) | Wt loss (%) | Oil Yield (wt%) | Gas Yield (wt%) | Unreacted Organics (wt%) | Coke (wt%) |
| Expt-1 | 500 | 0 | 47.71 | 15.30 | 10.71 | 4.59 | 0.08 | 0.33 |
| Expt-2 | 400 | 0 | 41.39 | 16.77 | 12.46 | 4.31 | 2.66 | 5.78 |
| Expt-3 | 300 | 0 | 50.88 | 1.08 | 0.64 | 0.44 | 15.52 | 1.16 |
| Expt-4 | 500 | 500 | 38.5 | 18.70 | 10.63 | 8.07 | 0.16 | 1.03 |
| Expt-5 | 400 | 500 | 39.09 | 9.67 | 2.06 | 7.61 | 7.68 | 0.22 |
| Expt-6 | 300 | 500 | 44.47 | 2.46 | 0.67 | 1.79 | 15.16 | 1.44 |

**TABLE 7.8**

Results for the Nonisothermal Pyrolysis of the 1 in. Diameter S2 Oil Shale Core at Ambient Pressure

| Experiment # | Heating Rate (°C/min) | Sample Mass (g) | Wt. Loss (%) | Oil Yield (wt%) | Oil Yield/ Wt. Loss |
|---|---|---|---|---|---|
| Expt-1 | 1 | 145.08 | 15.34 | 8.76 | 0.57 |
| Expt-2 | 5 | 144.46 | 13.50 | 8.20 | 0.60 |
| Expt-3 | 10 | 145.32 | 10.41 | 7.66 | 0.73 |

*Note:* Samples were held at final temperature of 500°C for 2 h.

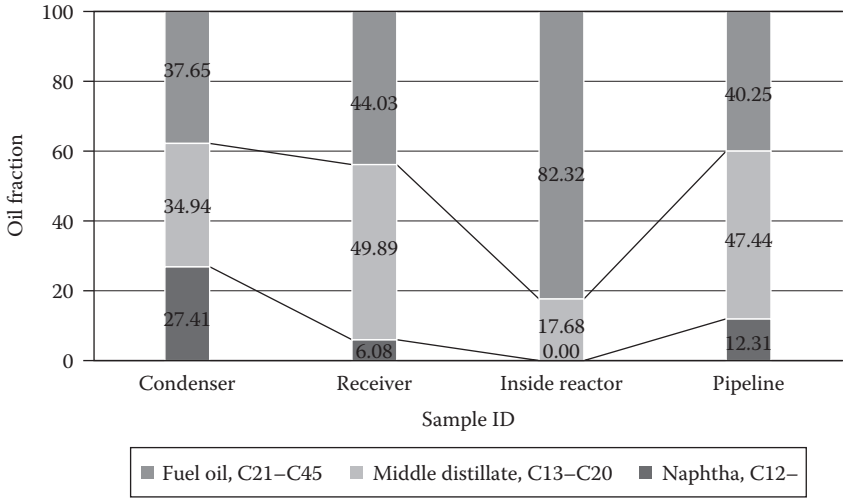


**FIGURE 7.11**
Grade of oil samples collected during the pyrolysis of S2 1 in. diameter core at a heating rate of 5°C/min to a final temperature of 500°C. The column labels indicate the location in the experimental apparatus where the oil was sampled (see Figure 7.3).

- 350°C and 500°C experiments at ambient pressure—The temperature reading 1 in. from the center (TC-3) is higher than the surface temperature (TC-5); TC-5 is the controlling thermocouple.
- 350°C experiment at ambient pressure—TC-2 has a lower temperature reading than the center of the core.
- 500°C experiment at 500 psig—TC-3 has a higher temperature reading than all of the other thermocouples.

The experiment with an isothermal surface temperature of 350°C and ambient pressure has a steady-state temperature gradient of approximately

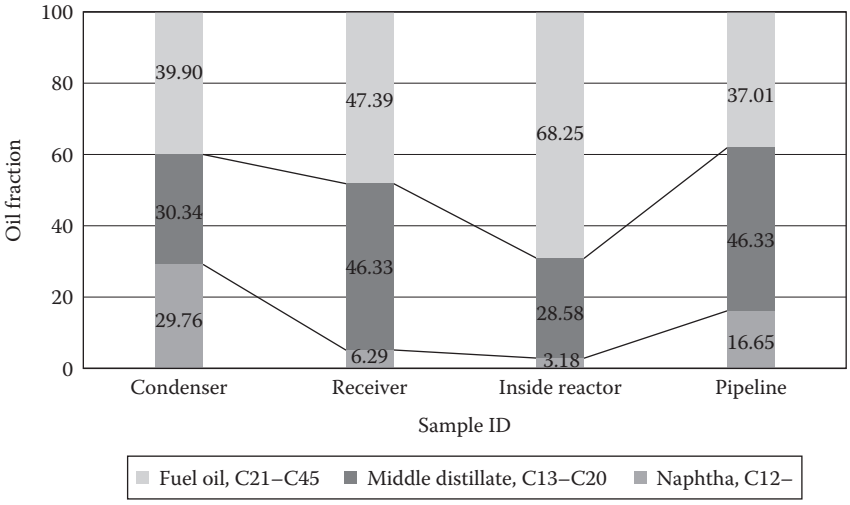


**FIGURE 7.12**
Grade of oil samples collected during the pyrolysis of S2 1 in. diameter core at a heating rate of 10°C/min to final temperature of 500°C. The column labels indicate the location in the experimental apparatus where the oil was sampled (see Figure 7.3).

80°C/in. This gradient is primarily due to heat losses despite heavy insulation. The lowest temperature (TC-2) is 310°C, which is outside the pyrolysis range of 350°C–400°C. The experiment at 500°C and ambient pressure has a similar gradient, but the lowest temperature (TC-2) is above 400°C, which is in the pyrolysis range.

At 500 psig, there is less temperature gradient in the core. In the experiment, the temperature control was on the surface of the reactor and not on the surface of the core. Under these conditions, higher pressure would lead to better heat transfer through the medium in the annulus and therefore a smaller overall temperature gradient in the system. Heat trans-port effects are a limiting phenomenon for pyrolyzing kerogen in bulk quantities.

Results from the isothermal experiments at various temperatures ranging from 350°C to 500°C can be seen in Table 7.9. The low weight loss for the experiment at 350°C and ambient pressure can be attributed to the tempera-ture set point itself and to the large temperature gradient in the sample. In contrast, the heat transfer effects are not as prominent in the 500 psig experi-ments, perhaps due to better heat transfer in the annular space that keeps the surface of the core at a higher temperature. For example, in the experiment at 400°C and 500 psig, each thermocouple measured a temperature above 300°C, the onset of pyrolysis. With higher core temperatures in the pressur-ized experiments, the weight loss was higher than for the same experiments

at ambient pressure. However, the oil yield was lower because more gas was produced at 500 psig than at ambient pressure, as indicated by the oil-yield-to-weight-loss ratio in Table 7.9.

The highest coke formation, 6.06% of the sample's original mass, occurred in the experiment at 500 psig and 500°C. This large amount of coke formation can be attributed to a longer residence time caused by a smaller pressure difference between the core and the reactor's annulus. As the heat moves into the core, the internal core pressure increases due to pyrolysis reactions and thermal expansion. The generated pressure in the pores pushes the products out of the sample. This driving force is reduced if the pressure difference is small, resulting in longer residence times for the pyrolysis products within the core. Longer residence times at high temperatures increase secondary reactions (e.g., cracking and coking).

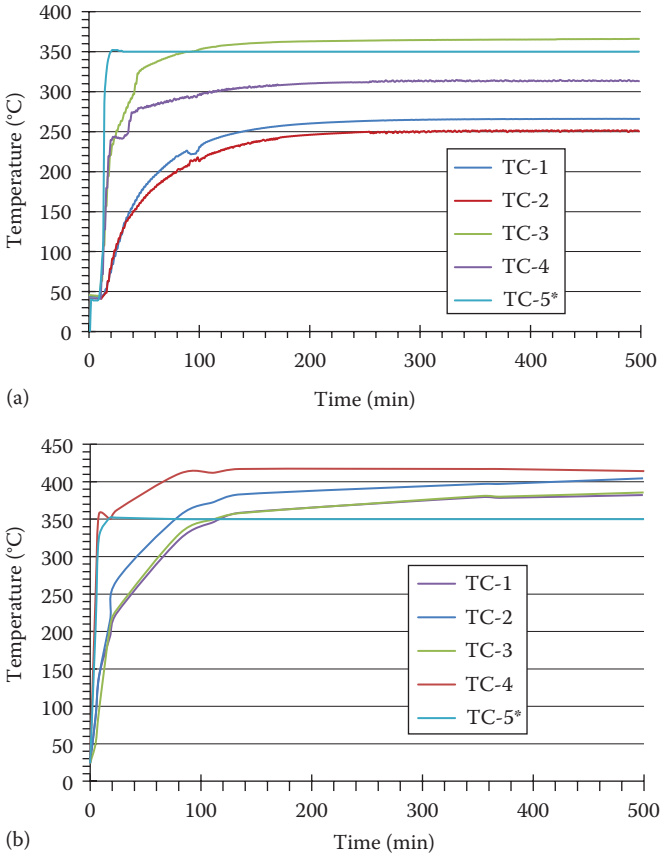


**FIGURE 7.13**
Temperature profiles during pyrolysis of 2.5 in. diameter core sample. (a) 350°C and ambient pressure (b) 350°C and 500 psig (*Control temperature probe.) (*Continued*)

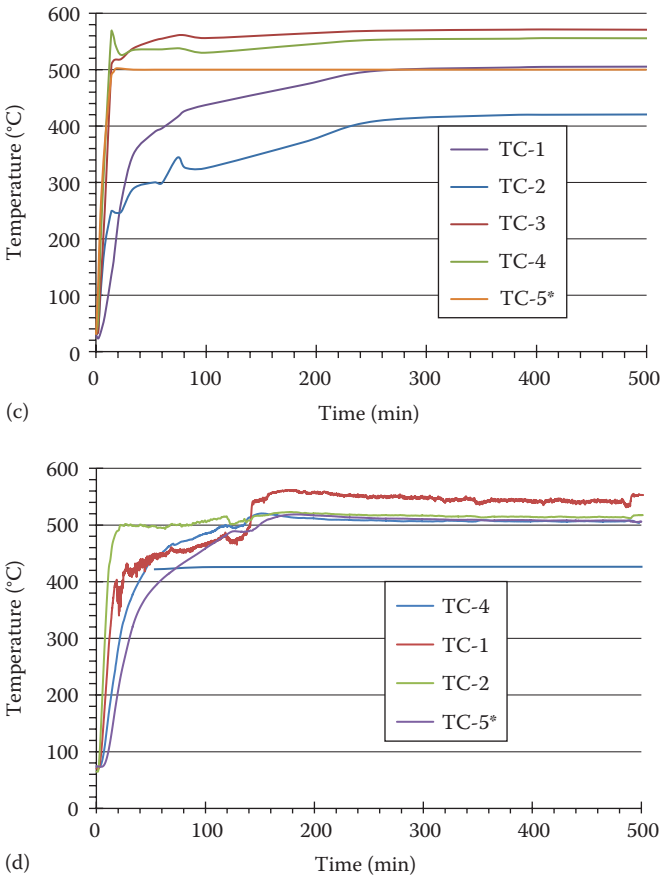


**FIGURE 7.13 (*Continued*)**
Temperature profiles during pyrolysis of 2.5 in. diameter core sample. (c) 500°C and ambient pressure (d) 500°C and 500 psig (*Control temperature probe.)

### *7.3.3.5 Pyrolysis of 1 in. Diameter GR Cores*

Following the isothermal pyrolysis of the 1 in. diameter GR1, GR2, and GR3 samples, the weight loss and oil yield were measured and the gas produced was calculated by material balance. The results are shown in Figure 7.14. An increase in temperature resulted in an increased weight loss and oil yield. GR1, the organic-rich sample, showed greater weight loss and oil yield than either the GR2 or GR3 samples.

A small amount of spent shale (post-pyrolysis core sample) was further pyrolyzed and then combusted, as described in Section 7.2.2.5, to estimate the unreacted organic remaining in the shale and the amount of coke formed during the pyrolysis, respectively. The results from the TGA analysis of the spent shale are shown in Figure 7.15.

**TABLE 7.9**

Experimental Results from the Pyrolysis of 2.5 in. Diameter S2 Oil Shale Cores at Different Isothermal Reactor Temperatures and Pressures

| Experiment # | Temperature (°C) | Pressure (psig) | Sample Mass (g) | Hold Time (h) | Wt. Loss (%) | Oil Yield (wt%) | Oil Yield/ Wt Loss |
|---|---|---|---|---|---|---|---|
| Expt-1 | 350 | 0 | 493.58 | 48 | 3.67 | 2.77 | 0.75 |
| Expt-2 | 350 | 500 | 695.15 | 48 | 14.44 | 8.32 | 0.57 |
| Expt-3 | 500 | 0 | 961.99 | 48 | 21.58 | 11.71 | 0.54 |
| Expt-4 | 500 | 500 | 760.00 | 24 | 24.52 | 7.97 | 0.32 |

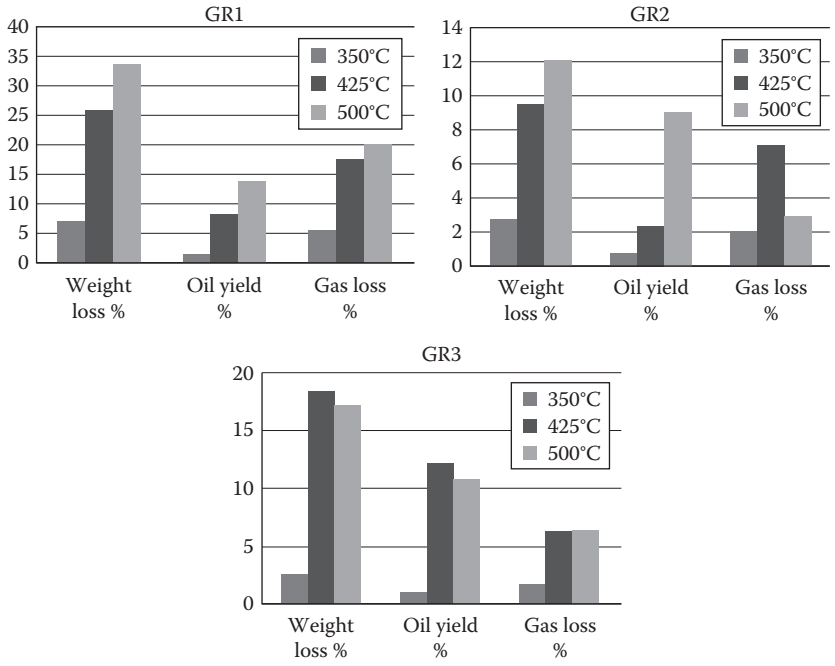


**FIGURE 7.14**
Weight loss, oil yield, and gas production (e.g., gas loss) during isothermal pyrolysis of GR core sections. The *y*-axis represents the data in weight percent.

The images of the spent shales after isothermal pyrolysis of the different sections of the three cores are shown in Figure 7.16. During high-temperature (500°C) pyrolysis, the cores with higher organic content (GR1) showed more deformation than at lower-temperature pyrolysis (350°C); they also showed more deformation than organic-lean cores (GR2). Pyrolysis experiments at 350°C resulted in less weight loss and correspondingly low oil yield, an indication that organic decomposition was slow.

The pyrolysis of GR cores showed a trend similar to the powdered TGA and CHNS analyses of the same sections. GR1 samples showed a greater weight loss (33%) at higher temperatures (500°C), but the oil yield (13.7 wt%) did not correspond to the weight loss. One reason for this discrepancy is that during the high-temperature, isothermal pyrolysis (24 h hold time), mineral decomposition may have contributed to the weight loss. The TGA analysis of spent shale showed the presence of significant organic material in pyrolyzed GR1 core samples. This organic matter could either be unreacted organics or heavy oil produced during core pyrolysis. Pyrolysis of GR1 cores also produced more coke relative to organic-lean

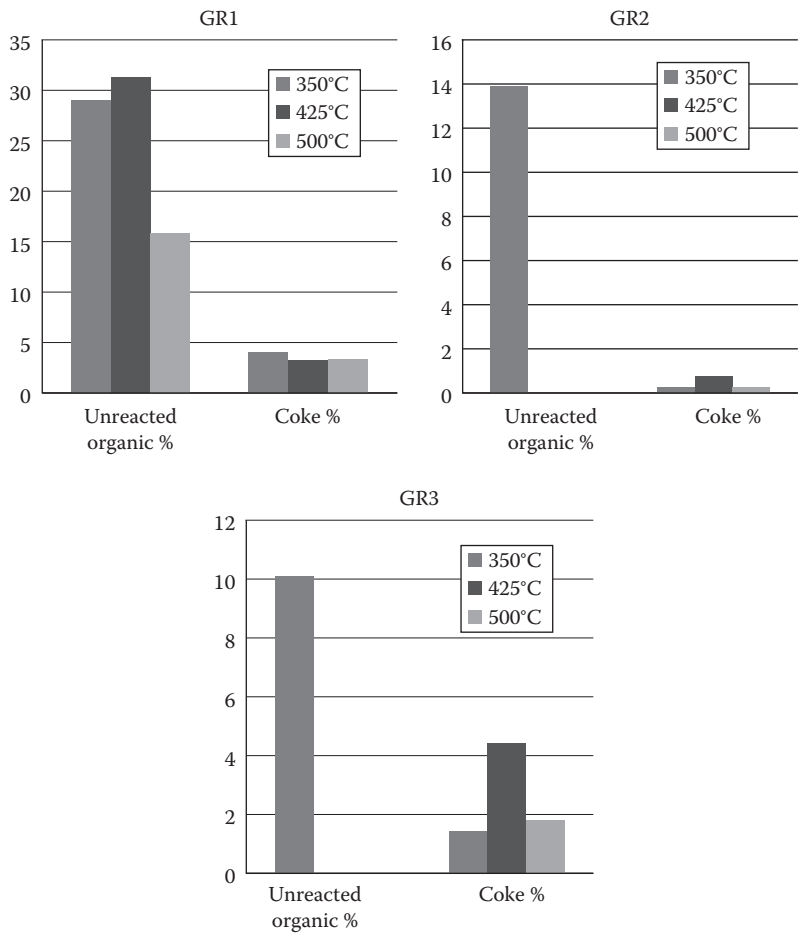


**FIGURE 7.15**
Unreacted organics and coke in the spent shales from isothermal pyrolysis of GR core sections. The *y*-axis represents the data in weight percent.

samples (GR2 and GR3). The results suggest that it is not only the temperature that influences coke formation but also the organic content of the shale.

Oil and gas samples from the reactor pyrolysis experiment were collected and analyzed using GC. The chromatograms of oils from GR core samples pyrolyzed at 500°C are shown in Figure 7.17. The distribution of hydrocarbons (Figure 7.18) shows that the oils produced from different shales under identical conditions differ in composition. A similar trend is seen in the gaseous products.

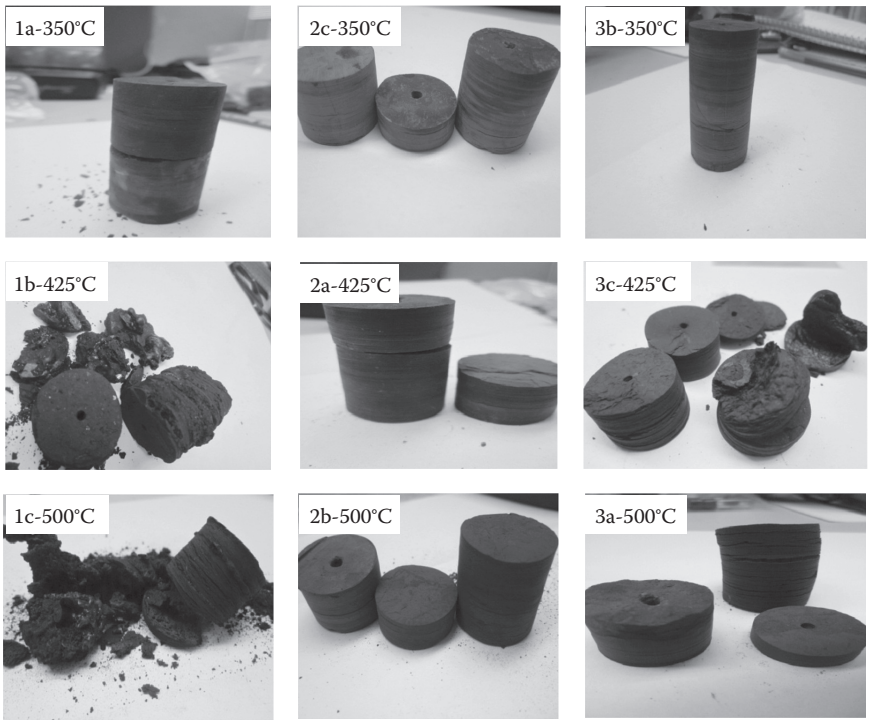


**FIGURE 7.16**
Images of the spent shales from the pyrolysis of GR core samples.

### 7.3.4 Comparison of Multiscale Core Pyrolysis Results

A comparison of the overall mass balances for the 2.5 and 0.75 in. diameter S2 core experiments at 500 psig is shown in Table 7.10. Because the shale oil produced in the larger core has a longer core residence time, it undergoes secondary reactions of coking and cracking, which decreases oil yield while increasing gas and coke yields. Also in the larger core, the weight loss is higher, which could be beneficial in increasing the flow pathways for the products.

For all the cores, most of the higher temperature experiments yielded higher weight loss (as seen in Tables 7.7 and 7.9 and in Figure 7.14). The grade and the yield of the oil were dependent on sample size, pressure, final temperature, and heating rate. A lower heating rate yielded a higher percentage of oil than higher heating rates. Higher pressure and higher temperature increased the rate of secondary coking and cracking reactions by increasing the residence time of the shale oil in hot zones; the 2.5 in. diameter core at high pressure and temperature yielded the most coke and gas. One exception to this trend was the 0.75 in. diameter core; more coke formed at 400°C than at 500°C.

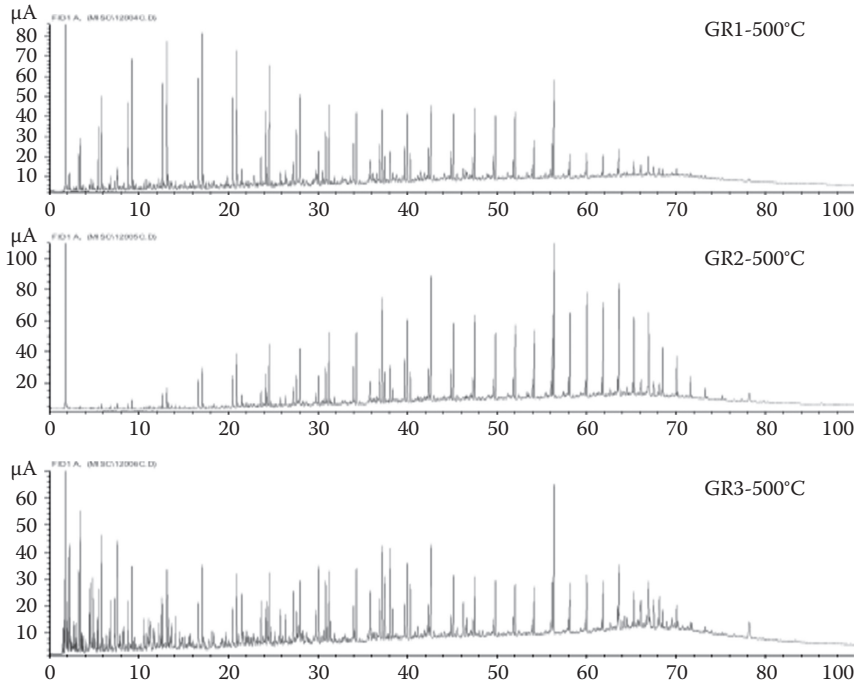


**FIGURE 7.17**
Gas chromatograms of the oil produced at 500°C from GR1, GR2, and GR3 oil shales.

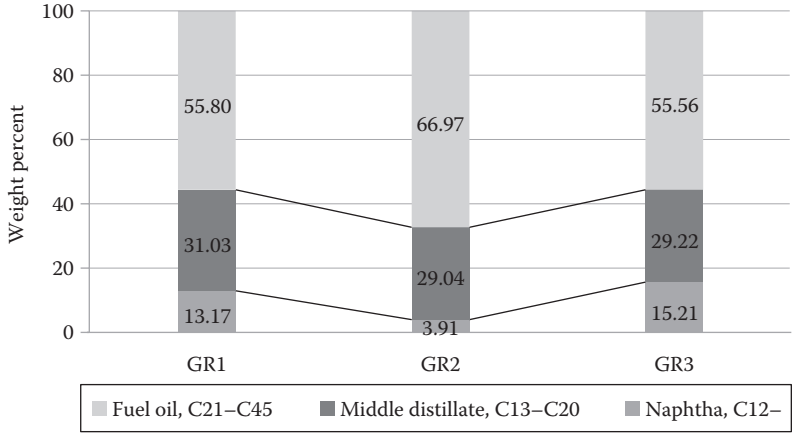


**FIGURE 7.18**
Oil fractions based on single carbon number distribution of the shale oils produced from pyrolysis of GR core samples at 500°C. Single carbon number distribution is a way of representing the GC spectra with the help of an internal standard.

**TABLE 7.10**

Comparison of Overall Mass Balance Results for the Isothermal Pyrolysis of 2.5 in. and 0.75 in. Diameter S2 Cores at 500°C and 500 psig

| Material Balance | 2.5 in. Diameter Core | 0.75 in. Diameter Core (%) |
|---|---|---|
| Wt. loss % | 24.52 | 18.69 |
| Oil yield, wt% | 7.96 | 10.63 |
| Coke, wt% | 6.06 | 1.03 |
| Gas, wt% | 16.56 | 8.06 |
| Unreacted organics (wt %) | 0.05 | 0.43 |

## 7.4 Summary and Conclusions

The TGA and multiscale pyrolysis experiments were used to obtain intrinsic reaction rates of Green River oil shale and to study the effects of core size, heating regime, pressure, and final temperature on product distribution and oil yield. It was found that larger core sizes produced more coke and gas per unit mass of core sample, indicating that secondary reactions were occurring inside the core samples. The oil production in nonisothermal heating regimes was dampened by heat transport effects in core sizes with diameters larger than 1 in. It was found that higher pressure lowered the temperature gradient in larger core samples, producing a higher weight loss but a lower oil yield.

Pyrolysis experiments on larger core samples or pilot-scale in situ experiments are needed to provide data for model validation. Such experiments will provide researchers with information on how the oil shale rock will crack and fracture due to thermal expansion, kerogen degradation, oil/gas expansion, and pressure changes, potentially creating macrochannels for product removal. More research is also required to determine if higher temperatures and pressures generated from pyrolysis reactions could create enough back-pressure to move products through the rock to a collecting well.

The fundamental characterization of Green River oil shale described in Chapter 5 together with models that describe how oil forms during pyrolysis (Chapter 6 and this chapter) and moves through the rock (Chapters 8 and 9) are steps toward creating new technologies that make oil shale an economically and environmentally viable source of long-term energy.